Institute of Geophysics
Polish Academy of Sciences

Satellite imagery to support flood risk modelling in large European rivers

PhD Thesis by:

Yiwei Guo

Supervisor: Dr. hab. Michael Nones

Warsaw, 2026

Abstract

In the context of increasingly frequent flood hazards driven by climate change, reliable hydrodynamic modelling is essential for effective flood management. Among all model input parameters, roughness, which is commonly represented by Manning's n, plays a critical role in regulating flow resistance. However, most hydrodynamic models assume fixed roughness values and neglect vegetation dynamics, even though vegetation varies seasonally or suddenly due to events such as floods and significantly influences hydraulic resistance. This assumption may increase model uncertainty, particularly in river reaches with vegetated sandbars.

To address this limitation, this study proposes a framework for estimating vegetation dynamic roughness by integrating uncrewed aerial vehicle (UAV) observations and satellite remote sensing. UAV surveys conducted during the vegetation growth period (May 2025) in two large European rivers, the Vistula (Poland) and the Po (Italy), provided high-resolution vegetation characteristics and multispectral data. The Vegetation height (h) was related to multispectral vegetation indices (NDVI, GNDVI, LCI, NDRE, and OSAVI) using machine learning (Random Forest and Extra Trees with three-fold cross-validation). The vegetation indices calculated from Sentinel-2 imagery were applied to the trained model for satellite-based h estimation. Satellite-based dynamic vegetation roughness was calculated from the estimated vegetation height using Manning's formulation and implemented in the numerical model Delft3D Flexible Mesh to evaluate the impact of satellite-based vegetation roughness on flow discharges.

The results showed that the machine learning models performed better for vegetation heights between 0-3 m than for 3-20 m, indicating higher reliability for grass and shrubs than for trees. Validation against UAV observations showed strong agreement, with R^2 values of 0.95 (Vistula) and 0.94 (Po), and low systematic bias. Hydrodynamic calibration identified optimal fixed Manning's n values of 0.06 for both the Vistula and Po reaches. Both fixed and dynamic roughness approaches reproduced discharge accurately (r_P^2 and $NSE > 0.90$), although systematic underestimation was observed. Dynamic roughness reduced bias under varying vegetation conditions, particularly in the Vistula reach.

Overall, the proposed approach enables satellite-based estimation of vegetation roughness and demonstrates its applicability in real-river hydrodynamic modelling. The framework provides a time- and cost-efficient solution for integrating vegetation dynamics into flood simulations and supports more physically consistent flood management practices.

Keywords: Vegetation Height, Vegetation Roughness, Uncrewed Aerial Vehicle, Satellite Imagery, Machine learning, Delft 3D FM model, Vistula River, Po River.

Abstract in Polish

W kontekście coraz częstszych zagrożeń powodziowych wywołanych zmianami klimatu, wiarygodne modelowanie hydrodynamiczne jest niezbędne dla skutecznego zarządzania powodziami. Wśród wszystkich parametrów wejściowych modeli szorstkość, najczęściej reprezentowana przez współczynnik Manninga *n*, odgrywa kluczową rolę w regulacji oporów przepływu. Jednak większość modeli hydrodynamicznych zakłada stałe wartości szorstkości i pomija dynamikę roślinności, mimo że roślinność zmienia się sezonowo lub nagle w wyniku zdarzeń takich jak powodzie i istotnie wpływa na opory hydrauliczne. Założenie to może zwiększać niepewność modeli, szczególnie na odcinkach rzek z porośniętymi roślinnością łachami rzecznymi.

W celu przezwyciężenia tego ograniczenia niniejsze badanie proponuje ramy metodyczne do estymacji dynamicznej szorstkości roślinności poprzez integrację obserwacji z bezzałogowych statków powietrznych (UAV) oraz teledetekcji satelitarnej. Kampanie UAV przeprowadzone w okresie wzrostu roślinności (maj 2025 r.) na dwóch dużych rzekach europejskich, Wiśle (Polska) i Padzie (Włochy), dostarczyły danych o wysokiej rozdzielczości dotyczących cech roślinności oraz danych wielospektralnych. Wysokość roślinności (*h*) została powiązana z wielospektralnymi wskaźnikami roślinności (NDVI, GNDVI, LCI, NDRE oraz OSAVI) z wykorzystaniem metod uczenia maszynowego (Random Forest oraz Extra Trees z trzykrotną walidacją krzyżową). Wskaźniki roślinności obliczone na podstawie zobrazowań Sentinel-2 zostały następnie wykorzystane w wytrenowanym modelu do estymacji satelitarnej wysokości *h*. Dynamiczna szorstkość roślinności oparta na danych satelitarnych została obliczona na podstawie oszacowanej wysokości roślinności przy użyciu wzoru Manninga i zaimplementowana w modelu numerycznym Delft3D Flexible Mesh w celu oceny wpływu satelitarnie oszacowanej szorstkości roślinności na przepływy.

Wyniki wykazały, że modele uczenia maszynowego osiągały lepsze rezultaty dla roślinności o wysokości 0–3 m niż dla roślinności o wysokości 3–20 m, co wskazuje na większą wiarygodność w przypadku traw i krzewów niż drzew. Walidacja względem obserwacji UAV wykazała wysoką zgodność, z wartościami R^2 równymi 0,95 (Wisła) oraz 0,94 (Pad) oraz niskim obciążeniem systematycznym. Kalibracja modelu hydrodynamicznego wykazała, że optymalna stała wartość współczynnika Manninga n wynosi 0,06 zarówno dla odcinka Wisły, jak i Padu. Zarówno podejście ze stałą szorstkością, jak i podejście z dynamiczną szorstkością dobrze odwzorowały przepływ (r_P^2 oraz NSE $>$ 0,90), choć zaobserwowano systematyczne niedoszacowanie. Dynamiczna szorstkość zmniejszyła błąd w warunkach zmiennej roślinności, szczególnie na odcinku Wisły.

Podsumowując, zaproponowane podejście umożliwia satelitarną estymację szorstkości roślinności oraz potwierdza jego przydatność w modelowaniu hydrodynamicznym rzeczywistych rzek. Opracowane ramy stanowią rozwiązanie efektywne pod względem czasu i kosztów w zakresie integracji dynamiki roślinności z symulacjami powodziowymi oraz wspierają bardziej fizycznie spójne zarządzanie ryzykiem powodziowym.

Słowa kluczowe: wysokość roślinności, szorstkość roślinności, bezzałogowe statki powietrzne, zobrazowania satelitarne, uczenie maszynowe, model Delft3D FM, Wisła, Pad.

Content

Figures

Tables

List of Acronyms

1D	One-dimensional
2D	Two-dimensional
3D	Three-dimensional
ADI	Alternating Direction Implicit
API	Application Programming Interfaces
CFL	Courant–Friedrichs–Lewy
Delft3D FM	Delft3D Flexible
DEM	Digital Elevation Models
DJI M3M	DJI Mavic 3 Multispectral
DSM	Digital Surface Models
ET	Extra Trees
G	Green band
GEE	Google Earth Engine
GNDVI	Green Normalized Difference Vegetation Index
GPW	Gridded Population of the World
LCI	Leaf Chlorophyll Index
ML	Machine Learning
MVIs	Multispectral Vegetation Indices
n	Manning's n
NDRE	Normalized Difference Red Edge Index

NDVI	Normalized Difference Vegetation Index
NIR	Near-infrared Band
NSE	Nash–Sutcliffe Efficiency
OOB	Out-of-bag
OOF	Out-of-fold
OSAVI	Optimized Soil Adjusted Vegetation Index
PBIAS	Percent Bias
PR	Po River
R	Red band
r_P^2	Coefficient of Determination, calculated as the square of the Pearson correlation coefficient
R^2	Coefficient of Determination
RE	Red-edge band
RF	Random Forest
RMSE	Root Mean Squared Error
UAV	Uncrewed aerial vehicle
VC	Vegetation conditions
VR	Vistula River
C	Chézy C

List of Symbols

Q	Discharge	[m³/s]
A	Area of cross section	[m²]
H	Water level	[m]
H_h	Water depth	[m]
S_0	Bed slope	[-]
S_f	Friction slope accounting for resistance effects	[-]
v	Cross-sectionally averaged flow velocity	[m/s]
R	Hydraulic radius	[m]
τ_b	Bed shear stress	[kg·m⁻¹·s⁻²]
ρ	Water density	[kg/m³]
g	Velocity vector	[m/s²]
h_1	Flow depth	[m]
u	Depth-averaged velocity vector	[m/s]
Q_f	Net water flux per unit area due to precipitation and evaporation	[m/s]
P_x, P_y	Hydrostatic pressure gradient terms in the x and y directions	[m/s²]
f_u, f_v	Coriolis force terms in the x and y momentum equations	[m/s²]
F_x, F_y	Imbalance of horizontal Reynolds stresses (turbulent	[m/s²]

	momentum diffusion terms)	
M_x, M_y	External momentum source or sink terms	[m/s²]
F_{sx}, F_{sy}	Secondary flow correction terms in the depth-averaged momentum equations	[m/s²]
y_i	Observed value of the i-th sample	[m]
$\hat{y}_i$	Model-predicted value of the i-th sample	[m]
$\bar{y}$	Mean of observed values	[m]
N	Number of samples	[-]
Qi	Observed value of the i-th sample	[m3/s]
S_i	Simulated (estimated) value of the i-th sample	[m3/s]
$\bar{Q}$	Mean of observed values	[m3/s]
$\bar{S}$	Mean of simulated values	[m3/s]
C_D	Drag coefficient	[-]
m	Vegetation stem density	[-]
D	Characteristic stem diameter	[m]

Data source

Data	Project/Organisation	Website
Bed level of Vistula Reach	Informatyczny System Osłony Kraju	https://isok.gov.pl/o-projekcie.html
Bed level of Po Reach	Italian Autorità di bacino distrettuale del fiume Po	https://www.adbpo.it/
Hydrological data (discharge and water level) of Vistula	Hydroportal IMGW-PIB	https://hydro.imgw.pl/#/
Hydrological data of Po	Agenzia per l’Energia e lo Sviluppo Sostenibile	https://www.agenziapo.it/content/monitoraggio-idrografico-0
Satellite data	Sentinel-2	https://sentinels.copernicus.eu/copernicus/sentinel-2

Chapter 1 Introduction

Accurate quantification of river channel roughness is essential for flood modelling, as roughness strongly controls water levels, flow velocities, and flood-wave propagation. Conventional approaches typically assign time-constant (hereafter defined as "fixed") roughness, mainly defined with Manning's *n* or Chézy *C* values derived from land use data. This approach fails to capture the temporal variability of riparian vegetation, a major driver of river bed roughness, induced by seasonal dynamics and flood disturbances. To address this limitation, the current thesis study integrates uncrewed aerial vehicle (UAV, commonly defined as "drone") and satellite observations with data-driven modelling to derive dynamic vegetation roughness at large spatial and temporal scales and its impact on flood modelling results.

In the following sections, the research background, motivation, questions, and framework will be explained.

1.1 Background

Floods are the most common type of natural hazard worldwide, and pose substantial risks to life, property, and food production (Dottori *et al.* 2018). A flood is defined as an event that occurs when water inundates land that is normally dry, or when a river's flow exceeds its channel capacity and overflows its banks (Speer and Gamble 1965, Rogers *et al.* 2017). As natural phenomena that occur in various geographic regions and at different time scales, the character of floods results from complex atmospheric and hydrological processes such as intense rainfall, snowmelt, or sudden storms (Halecki and Młyński 2025).

Recently, driven by climate change, more frequent extreme weather events, such as heavy rains, storms, and rapid snowmelt, have led to a rise in severe floods, particularly across Europe (Rahmani and Fattahi 2023, Halecki and Młyński 2025), as summarized in Figure 1-1, where data from the Historical Analysis of Natural Hazards in Europe (HANZE) dataset (Paprotny *et al.* 2024) are reported.

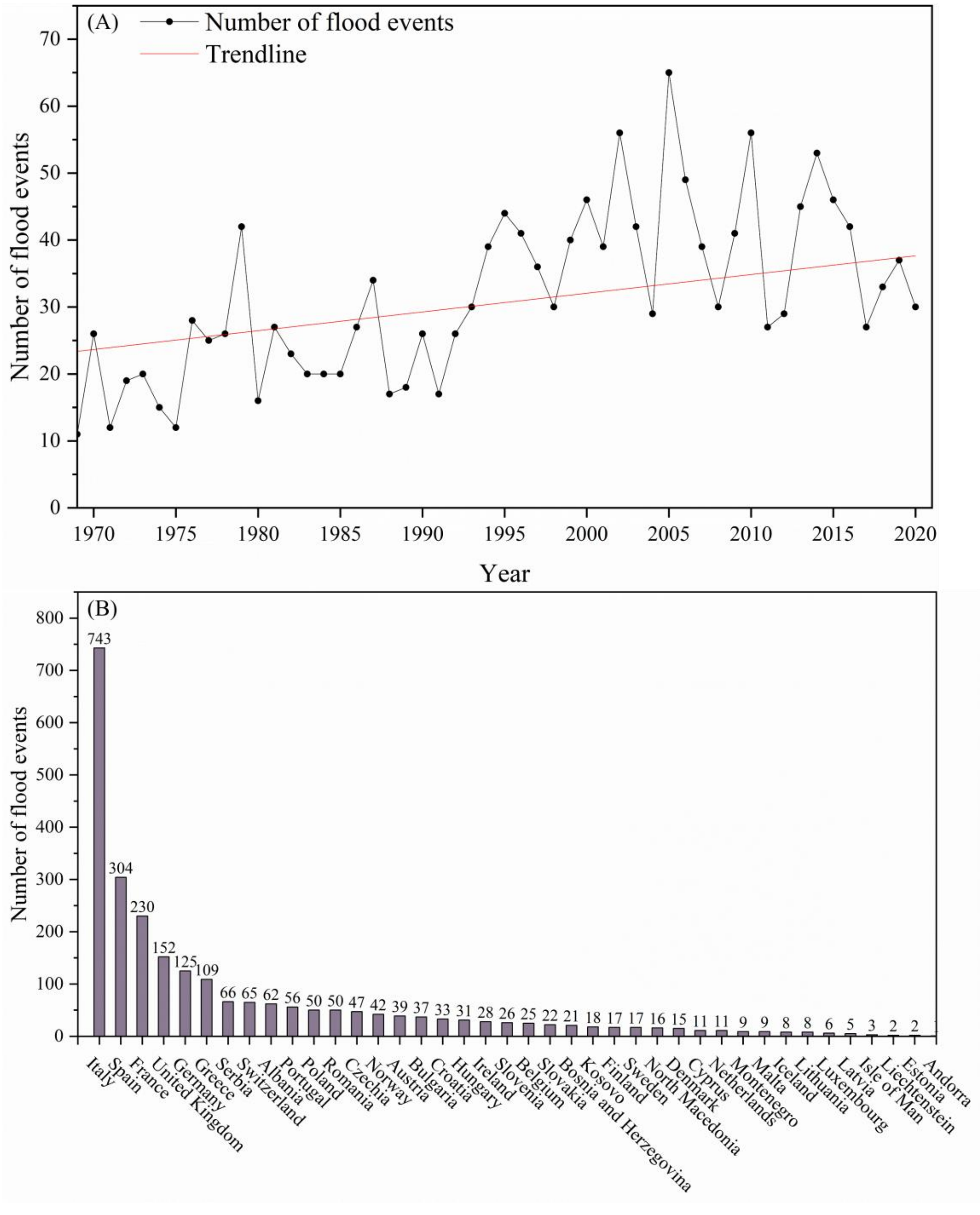

Figure 1-1. (A) Number of flood events recorded in Europe between 1970 and 2020, with trendline in red. (B) Number of floods occurred between 1970 and 2020 subdivided by impacted country.

Due to the huge damage caused by flood events, a wide variety of hydraulic models have been developed for the prediction and forecasting of river response to flood events and restoration actions (Barinas *et al.* 2024).

The accuracy of simulation results of hydrodynamic models is controlled by the quality of the input parameters (Tang *et al.* 2021). Among all the parameters, it was shown that roughness is one of the most critical for flood modelling (Keupers *et al.* 2015, Chen, Cao, *et al.* 2023, Aksoy *et al.* 2024, Niu *et al.* 2025).

Previous studies have demonstrated that increased channel roughness enhances flow resistance (Anderson *et al.* 2006, Acar 2025), leading to a decrease in peak discharge and a delay in the arrival of the peak at the outlet. From a hydraulic perspective, higher roughness increases energy losses and reduces flow conveyance, thereby slowing flood wave propagation (Chow 1959). Therefore, part of the flood volume is temporarily stored within the channel and floodplain, which not only lowers peak discharge but also modifies the stage-discharge relationship. In addition to its influence on discharge dynamics, increased roughness has been shown to significantly affect water levels. Both experimental and numerical studies indicate that higher roughness values result in increasing water level for a given discharge, particularly under shallow or overbank flow conditions where vegetation-induced resistance becomes dominant (Baptist *et al.* 2007, Nepf 2012a). Such effects are especially significant in vegetated channels and floodplains, where roughness-induced backwater effects can raise local water levels and prolong inundation duration (Green 2005, Stamou *et al.* 2012). Roughness parameterisation plays a critical role not only in shaping flood hydrographs but also in controlling simulated water levels and inundation patterns (Horritt and Bates 2002, Pappenberger *et al.* 2005, Anderson *et al.* 2006, Neal *et al.* 2012, Acar 2025). By regulating flow resistance, roughness modifies flow velocity and energy dissipation, altering peak discharge magnitude and hydrograph timing (Horritt and Bates 2002). Previous studies have shown that even when discharge simulations were well calibrated, different roughness values can lead to noticeable differences in simulated water levels and flood extent, particularly during high discharge conditions when floodplain storage becomes significant (Pappenberger *et al.* 2005, Neal *et al.* 2012). These highlight that roughness is not merely a calibration coefficient for matching discharge, but a key physical control on stage dynamics and inundation patterns (Anderson *et al.* 2006, Acar 2025).

However, most commonly used hydrodynamic models, such as Delft3D Flexible Mesh (FM), HEC-RAS, and MIKE 11, are generally driven by a fixed roughness value, under the assumption of a clear-water channel devoid of vegetation, or assuming it does not change over time, therefore ignoring the fact that bed roughness varies with vegetation spatiotemporal changes (Keupers *et al.* 2015, Jiang *et al.* 2021). Indeed, extreme floods can rapidly alter vegetation structure and distribution, causing significant shifts in hydraulic characteristics and compromising predictions of water levels and inundation extents (Guo *et al.* 2025). At the same time, vegetation seasonality could influence floods differently, depending on the timing of occurrence of such high-flow events (Thapa *et al.* 2016, Vermuyten *et al.* 2020).

From this overview, one can see that predictive models that incorporate temporally variable vegetation characteristics are vital for accurately estimating changes in flow resistance over time (Augustijn *et al.* 2008). To support such modelling efforts, robust and continuous monitoring of vegetation dynamics is indispensable. This includes tracking changes in vegetation height, density, spatial coverage, and species composition across different temporal scales, from seasonal growth cycles to rapid post-flood recovery periods (Guo *et al.* 2025).

Traditionally, vegetation monitoring is conducted through field measurements.

However, this method has significant challenges in terms of being time-consuming, costly, and poorly suited for long-term, large-scale applications (Boardman and Evans 2020, Dashpurev *et al.* 2021). To address this limitation, recent advancements demonstrated how remote sensing technologies could allow for monitoring vegetation along extended river reaches over long periods (Aguiar *et al.* 2015, Aishwarya *et al.* 2026). Satellite imagery provides long-term event records over large spatial scales, but its spatial resolution is mostly not high enough to allow for adequate tracking of small-scale vegetation changes (Francis *et al.* 2024, Radeloff *et al.* 2024, Wang *et al.* 2024). In contrast, uncrewed aerial vehicle (UAV) imagery offers very high spatial resolution, but lacks in ensuring an adequate time coverage, especially back in time (Dash *et al.* 2017, Lu and He 2017).

Improving existing knowledge, this thesis focuses on developing a workflow for near-real-time monitoring of vegetation by integrating limited times of UAV-based field measurements with satellite imagery. This innovative workflow will allow for deriving spatially and temporally variable information of riparian vegetation, which are then translated into spatiotemporal representations of bed roughness, to be used as a more realistic inputs for flood modelling.

1.2 Motivation and research questions

1.2.1 Research motivation

Flood modelling and forecasting are essential for flood risk management; however, the reliability of modelling outputs is highly subject to input parameters. Among all uncertainties, roughness has long been regarded as one of the most important factors controlling simulated water levels, discharges, and flow velocities, particularly in river floodplain systems. During flood periods, flow resistance caused by vegetation is often dynamic, further increasing the sensitivity of model results to roughness representation.

In current research, roughness used to drive hydrodynamic modelling is commonly set as a fixed parameter derived from land-use classifications, experience relationships, or limited field observations. This assumption fails to represent the vegetation dynamics in real river systems. Riparian and floodplain vegetation exhibits significant variability in height, density, and spatial distribution across growth stages and may experience rapid structural changes during flood events, directly modifying flow resistance. The inequality between vegetation conditions and roughness values can therefore lead to uncertainty in flood simulations.

Although previous studies have attempted to describe vegetation-related flow resistance using empirical or semi-experimental formulations, these approaches are often developed under laboratory conditions or calibrated for specific sites, which limits their applicability to real rivers. Field measurements can provide accurate vegetation condition information, but their limited spatial coverage and lack of temporal continuity limit their usefulness for large-scale and long-term flood modelling. Therefore, a practical approach for dynamically representing vegetation roughness in real river systems is still lacking.

Recent developments in remote sensing have created new opportunities for monitoring dynamic vegetation. UAV observations provide high-resolution and structurally explicit vegetation information, while satellite imagery enables large-scale and long-term monitoring through multispectral vegetation indices. However, these accessible data sources have insufficient spatial resolution to describe vegetation conditions and it is difficult to quantify the roughness required to drive the model. A key challenge, therefore, lies in bridging this scale gap and estimating satellite-based dynamic vegetation roughness to feed hydrodynamic modelling.

Motivated by these open questions, this thesis aims to systematically integrate vegetation dynamics into hydrodynamic modelling through dynamic roughness estimation, with a particular focus on river sandbars characterised by complex and heterogeneous vegetation rather than simplified conditions dominated by a single vegetation type. For the first time, this study demonstrates at the river scale that satellite-derived vegetation dynamics over sandbars covered by mixed vegetation (from grass to trees) can be translated into hydraulically meaningful roughness parameters and directly input into hydrodynamic flood simulations, enabling explicit representation of vegetation effects under realistic and spatially heterogeneous conditions. By comparison with traditional modelling approaches using fixed roughness values and simplified vegetation assumptions, this approach enhances the realism, transferability, and practical applicability of flood modelling in support of flood risk assessment and management.

1.2.2 Research questions

This study is based on four primary research questions.

1. How can vegetation characteristics that influence flow resistance be described in sandbars with complex vegetation conditions?

Vegetation characteristics that influence flow resistance can be described by focusing on key structural properties, such as vegetation height, rather than by assuming a single vegetation type. In sandbars with complex vegetation conditions, these characteristics can be represented as spatially heterogeneous patterns, reflecting the coexistence of grasses, shrubs, and woody vegetation. A UAV survey was conducted to collect the high spatial resolution imagery for analysing the vegetation height.

2. Can high spatial resolution UAV observations be used to support and improve vegetation monitoring based on long-term satellite imagery?

High spatial resolution UAV data are used to derive vegetation multispectral indices and vegetation height at selected sandbars. Datasets from UAV imagery are then used to train a machine learning model that learns the relationship between multispectral indices and vegetation height. Once this relationship is established, multispectral indices calculated from satellite imagery can be input into the trained model to estimate vegetation height for each satellite acquisition. Therefore, satellite imagery can be used for long-term vegetation monitoring, while UAV observations provide the necessary high-resolution reference data.

3. How can vegetation information derived from UAV and satellite data be

translated into spatial and temporal dynamic roughness for hydrodynamic models?

After vegetation height is estimated by inputting satellite-derived multispectral vegetation indices into the trained machine learning model, roughness is then calculated using roughness formulas (Manning's *n*). Therefore, satellite imagery is used to derive spatially distributed roughness, allowing roughness to vary across space and over time rather than being treated as a fixed value.

4. How does dynamic roughness affect simulated discharge compared to fixed roughness values in hydrodynamic models, and can satellite imagery be applied to improve the accuracy of flood modelling results?

After satellite-based vegetation roughness is estimated, it is applied in a hydrodynamic model to test its performance in flood simulations. The dynamic roughness derived from satellite imagery is used to simulate discharge and is compared with results obtained using a best fixed roughness value calibrated into the numerical model. The model performance is evaluated by comparing simulated discharge with observed discharge using three performance metrics. Through this comparison, the applicability of the satellite-based dynamic roughness in flood modelling is assessed, and its performance is evaluated against the traditional fixed roughness approach to determine whether it provides acceptable and improved simulation results.

1.3 State-of-the-art

Vegetation is an important component of river and floodplain systems (Vyawahare and Tatewar 2025) and has a strong influence on hydrodynamic processes by modifying hydraulic roughness (Vargas-Luna *et al.* 2015, Mewis 2021). Through its effect on flow resistance, vegetation can alter flow velocity, water levels, and flood waves (Gómez *et al.* 2024). These effects are particularly evident in low-gradient rivers, where flow conveyance is strongly limited by vegetation (Nepf 2012a). As a result, vegetative roughness is widely regarded as one of the most important parameters in hydrodynamic models.

With the development of hydrodynamic modelling and observation techniques, research on vegetative roughness and vegetation monitoring has increased rapidly. Searches on Google Scholar (data covering the period 1900-2025) show that more than 32,800 publications are related to vegetation roughness, while approximately 3,310,000 studies focus on vegetation monitoring. Among these, about 1,330,000 studies use remote sensing for vegetation monitoring, including around 115,000 based on UAVs and approximately 1,410,000 based on satellite imagery. In addition, more than 100,000 studies investigate the influence of roughness or vegetation on hydrodynamic model results. All these studies demonstrate the importance of vegetation roughness in hydraulic simulations.

Despite this large amount of literature, the quantification of vegetation roughness over long time series remains limited. Most studies use vegetation information from limited observation periods or represent vegetation using fixed roughness values in hydrodynamic models (Arcement and Verne R. Schneider 1989, Straatsma and Baptist

2008, Ballesteros *et al.* 2011, Forzieri *et al.* 2011), which cannot represent long-term changes related to seasonal changes or extreme events. At the same time, many vegetation monitoring studies focus on vegetation cover or classification, while vegetation structural characteristics directly relevant to flow resistance, such as vegetation height or density, are less frequently used for model parameterization (Straatsma and Baptist 2008, Forzieri *et al.* 2011, Cho *et al.* 2012, Nepf 2012a).

Therefore, it is necessary to summarize how vegetative roughness affects hydrodynamic models and how vegetation monitoring approaches can support its quantification. Accordingly, this section is organized into two main parts: 1) the influence of vegetative roughness on hydrodynamic modelling, and 2) vegetation monitoring studies, with particular attention to the use of UAV and satellite remote sensing for long-term vegetation roughness estimation.

1.3.1 Effects of hydraulic roughness on hydrodynamic simulations

Bed roughness is one of the key parameters controlling flow resistance and energy dissipation in hydrodynamic models (Anzani *et al.* 2025). Regardless of whether one-dimensional (1D), two-dimensional (2D), or three-dimensional (3D) formulations are used, roughness directly affects velocity distribution, water-level variation, and flood waves through resistance terms in the momentum equations (Horritt and Bates 2002, Werner 2004, Morvan *et al.* 2008).

From a physical perspective, roughness does not represent a single directly measurable quantity. Instead, it constitutes a parameterised expression of the integrated resistance effects induced by bed material characteristics, bedform irregularities, and various flow obstructions (Chow 1959, Morvan *et al.* 2008). In numerical models, roughness is usually represented by a single parameter that combines the effects of many small-scale resistance processes that cannot be resolved explicitly (Chow 1959). Although this approach is widely used in the literature, it implies that modelling results are highly sensitive to input roughness values.

Within the framework of depth-averaged hydrodynamic models, roughness is represented as a friction term in the momentum equations, and its interaction with flow depth and velocity controls energy loss and momentum dissipation. In 1D and 2D shallow-water models based on the Saint-Venant equations, which describe the conservation of mass and momentum for unsteady open-channel flow, flow resistance is explicitly accounted for through a friction term in the momentum formulation (Hodges 2019). In one-dimensional form, the Saint-Venant momentum equation can be explained as equation (1-1) and Figure 1-2 (Swastika *et al.* 2021).

$$\frac{\partial Q}{\partial t} + \frac{\partial}{\partial x}\left(\frac{Q^2}{A}\right) + gA\frac{\partial H}{\partial x} + gA\left(S_f - S_0\right) = 0 \qquad (1\text{-}1)$$

where Q is discharge [m^3/s], A is the area of cross section [m^2], H is the water level [m], S_0 is the bed slope, and S_f is the friction slope accounting for resistance effects.

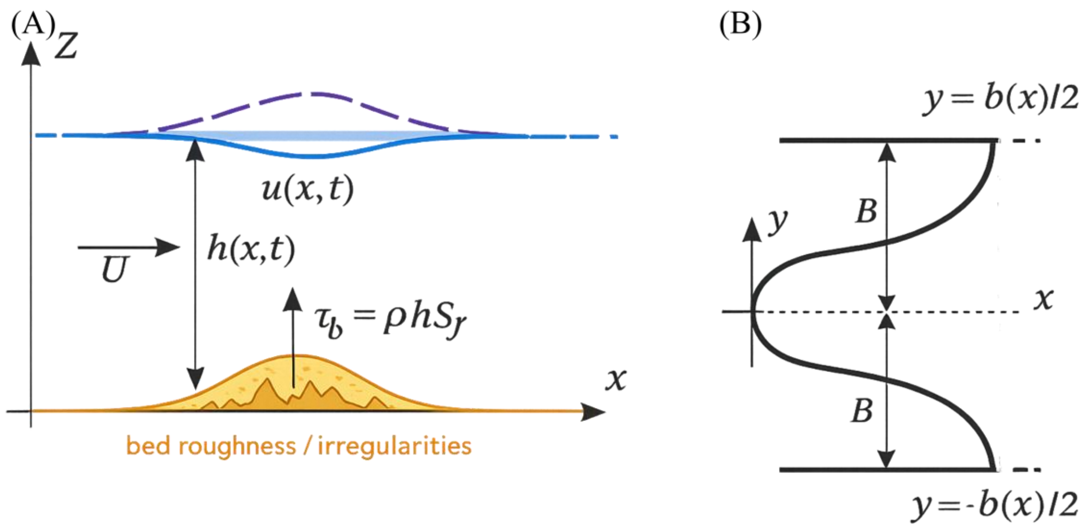

Figure 1-2. Conceptual scheme of depth-averaged hydrodynamic modelling. (A) Longitudinal section illustrating water depth, depth-averaged velocity, and the effect of bed roughness on flow resistance. (B) Plan view illustrating lateral flow redistribution associated with variations in channel width.

The friction slope S_f is commonly parameterized using empirical resistance laws, among which the Manning and Chézy formulations are the most widely applied (Crompton *et al.* 2025). Using the Manning formulation, the friction slope can be expressed as equation (1-2) (Crompton *et al.* 2025).

$$S_f = \left(\frac{nv}{R^{2/3}}\right)^2 \tag{1-2}$$

where v is the cross-sectionally averaged flow velocity [m/s], n is the Manning roughness coefficient, and R denotes the hydraulic radius [m]. The Manning equation can, therefore, be written in terms of velocity as equation (1-3) (Crompton *et al.* 2025).

$$v = \frac{1}{n} R^{2/3} S^{1/2} \tag{1-3}$$

where S represents the energy slope. Under the assumption of uniform flow, the energy slope is commonly approximated by the bed slope and the friction slope S_f , establishing a direct link between the prescribed roughness coefficient and momentum loss in the Saint-Venant momentum equation.

In numerical models, the friction slope is introduced into the momentum equations through the bed shear stress term (Hanif and Barber 2016, Hodges 2019). For example, in two-dimensional depth-averaged formulations, the bed shear stress is often written as equation (1-4) (Hanif and Barber 2016).

$$\tau_{b=\rho g h_1} S_f \frac{u}{\|u\|} \tag{1-4}$$

where $\boldsymbol{\tau}_b$ denotes the bed shear stress [kg·m⁻¹·s⁻²], ρ is the water density [kg/m³], g is the gravitational acceleration [m/s²], h_1 is the flow depth [m], and u is the depth-averaged velocity vector [m/s].

This formulation explicitly demonstrates how roughness, through the friction slope and bed shear stress, is embedded in the momentum equations, such that even minor variations in roughness can induce systematic changes in flow velocity and water levels under fixed topographic and boundary conditions.

In contrast to the Manning formulation, the Chézy equation adopts a different parameterization and can be expressed as equation (1-5) (Crompton *et al.* 2025).

$$v = C\sqrt{RS} \tag{1-5}$$

Where C is the Chézy coefficient representing the integrated resistance effects of the bed and boundaries.

Although empirical relationships are commonly used in engineering practice to convert between Chézy and Manning coefficients, the two resistance laws exhibit different dependencies on hydraulic radius and flow depth (Chow 1959, Vreugdenhil

1994). As a result, their sensitivities to roughness variations are not strictly equivalent in numerical models, particularly across different flow stages. Therefore, regardless of the roughness formulation used, the choice of resistance law can have a strong influence on simulated flow processes.

A large number of model-based studies have quantitatively demonstrated the high sensitivity of hydrodynamic simulations to roughness parameters. In 1D hydrodynamic models, roughness is widely recognized as the dominant control on the stage discharge relationship (Aronica *et al.* 2002, Pappenberger *et al.* 2005, Bozzi *et al.* 2015). Bozzi et al. (2015) demonstrated that water-level simulations are highly sensitive to roughness uncertainty in 1D hydraulic models, often more so than to upstream discharge uncertainty, and that roughness-related uncertainty can lead to systematic bias in predicted flood levels. Aronica et al. (2002) investigated the sensitivity of flood simulations to roughness parameters using 1D distributed hydrodynamic models and demonstrated that variations in roughness can lead to substantial differences in simulated water levels and inundation patterns. Similarly, the research of Pappenberger et al. (2005) found through uncertainty analyses that, in 1D flood simulations, roughness uncertainty often represents a primary source of water level error when compared with uncertainties in boundary conditions and channel geometry.

Compared with 1D models, 2D hydrodynamic models allow flow to redistribute laterally across the channel and floodplain, rather than being confined to a single downstream direction, enabling flow pathways to adjust in response to local resistance contrasts (Fleischmann *et al.* 2020). The research of Horritt and Bates (2002) showed that, in 2D flood models, simulated inundation extent and water-level distribution are highly sensitive to roughness parameters, indicating the important role of roughness in model uncertainty.

Previous studies using various 2D modelling platforms, including LISFLOOD-FP (Horritt and Bates 2002) and Delft3D (Al-Asadi and Duan 2017, Pasma *et al.* 2024), have reported consistent findings. All of them indicate that, under identical grid configurations and topographic conditions, variations in roughness alone can lead to substantial differences in velocity fields, flow pathways, and inundation extents, highlighting that roughness not only controls bulk energy dissipation but also governs flow redistribution and local hydrodynamic responses.

In 3D hydrodynamic models, although vertical velocity structures and turbulence processes are explicitly resolved, roughness remains a key parameter controlling near-bed hydrodynamics and energy dissipation. Glock et al. (2019) demonstrated that 3D hydrodynamic simulations are highly sensitive to bed roughness, particularly with respect to near-bed flow dynamics and bed shear stress. Similar sensitivity to roughness parameters can also be expected in three-dimensional Delft3D simulations, given the central role of bottom-friction formulations in controlling near-bed flow processes (Hsu *et al.* 2006, Pasma *et al.* 2024). These findings show that increasing model dimensionality does not diminish the importance of roughness, while it shows its role in controlling near-bed processes and energy dissipation more explicitly.

In conclusion, previous studies show that roughness is one of the most sensitive parameters in hydrodynamic modelling. Its interaction with flow depth, velocity, and model structure strongly affects simulated water levels, discharges, flood-wave propagation, and inundation patterns. This also highlights the limitations of using fixed roughness in complex river systems and motivates further investigation into the spatial variability and temporal dynamics of roughness.

1.3.2 Vegetation and hydraulic roughness

In hydrodynamic modelling of rivers and floodplains, vegetation is widely regarded as a key factor controlling hydraulic roughness and flood processes (Box *et al.* 2021). Early experimental and theoretical studies demonstrated that vegetation substantially increases flow resistance through form drag and additional momentum losses, finally modifying velocity distributions and stage–discharge relationships (Kouwen and Unny 1973, Petryk and Bosmajian 1975, Straatsma and Baptist 2008, Nepf 2012b, Penna *et al.* 2020). Nepf (2012b) provided a comprehensive synthesis of canopy flow dynamics, showing that stem diameter, spacing, and frontal area jointly govern turbulence structure and mean velocity profiles and thus represent the fundamental controls on vegetative resistance. From a resistance-law perspective, Poggi et al. (2004) and Baptist et al. (2007) established quantitative links between vegetation structure and hydraulic resistance, highlighting that vegetation dominates hydraulic response in floodplain environments. Numerical modelling studies further confirmed that vegetation-induced reductions in conveyance capacity can substantially amplify flood-stage responses and alter flood-wave propagation, particularly in low-gradient rivers (Järvelä 2002, Straatsma and Baptist 2008).

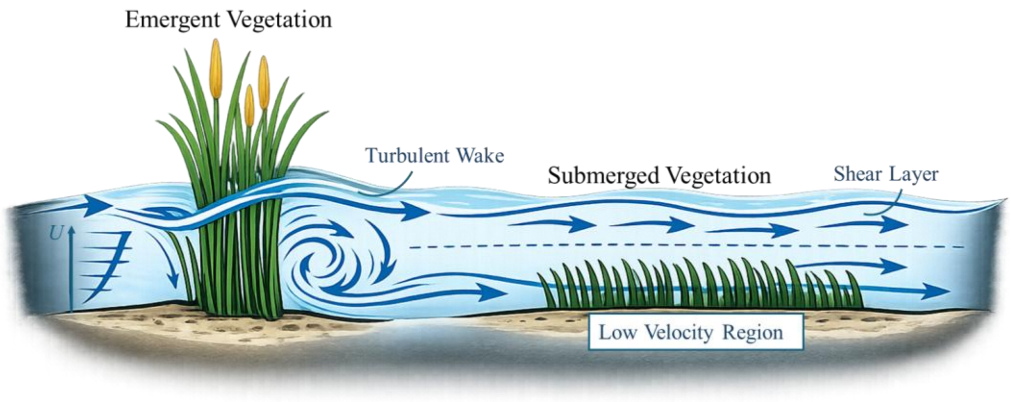

Figure 1-3. Conceptual illustration of flow-vegetation interactions under emergent and submerged conditions.

Different from bed roughness, however, vegetative roughness cannot be treated as a fixed physical property but represents a variable physical quantity dependent on flow depth, hydraulic conditions, and vegetation conditions. The two-layer analytical model proposed by Huthoff et al. (2007) pointed out that as vegetation transitions from emergent to submerged conditions, flow structure evolves from a single obstructed layer to a stratified system with distinct velocity profiles within and above the canopy, leading to depth-dependent resistance behavior (Figure 1-3). For flexible vegetation, Järvelä (2005) and Nepf (2012a) showed that bending and streamlining under increasing flow reduce effective frontal area and introduce strong nonlinearity in the relationship between discharge and resistance. These findings explain why a single, fixed and constant roughness is insufficient for representing hydraulic behavior across different flow stages and why vegetative roughness is among the most uncertain influential parameters in hydrodynamic models.

Sensitivity analyses conducted by previous studies consistently indicate that water levels are mostly sensitive to roughness variations, particularly under shallow-flow conditions, where even small roughness errors can produce pronounced stage deviations (Cowan 1956, Nepf 1999, Stone and Shen 2002, Wilson *et al.* 2003, Järvelä 2005, Pappenberger *et al.* 2005, Dalledonne *et al.* 2019).

However, measuring vegetative roughness directly is challenging, so many studies focus on hydrodynamically relevant vegetation characteristics, such as vegetation height (Cheng 2011, Zahidi *et al.* 2014), stem (Järvelä 2004, Cheng 2011) or branch diameter (D'ippolito *et al.* 2021), and density (Feng *et al.* 2024), which are subsequently translated into roughness parameters using physical or semi-empirical approaches. Łoboda et al. (2018) incorporated flexural rigidity into a drag–bending force framework and proposed a model linking stem diameter to hydraulic resistance.

Field-based vegetation surveys play a fundamental role by providing direct measurements of the physical properties that control flow resistance. For example, Järvelä (2002) quantified variations in roughness by measuring grass height and density under different vegetation configurations. However, field measurements are time-consuming and costly, and each survey can only reflect vegetation conditions during the survey period (Reinke and Jones 2006). Moreover, in riverine environments, field works are generally affected by local terrain conditions and flood events (Straatsma and Baptist 2008). In addition, hydrodynamic measurements conducted in natural rivers may be subject to substantial technical uncertainties. Przyborowski et al. (2018) conducted field-based velocity measurements around aquatic vegetation in a natural sandy-bed river and found that signal quality and correlation thresholds were strongly influenced by flow conditions and suspended sediment characteristics, which complicates the interpretation of instantaneous velocity profiles. As a result, field data are typically used for calibration and validation rather than for spatially continuous roughness mapping.

With the development of remote sensing, spatially continuous vegetation monitoring becomes possible. Early approaches relied on land cover-based roughness estimation; however, Straatsma & Baptist (2008) pointed out that such methods fail to capture the temporal and spatial variation of vegetation effects during flooding periods. Recently, more studies have increasingly focused on extracting vegetation conditions from LiDAR and optical data and incorporating these parameters into roughness estimations. Forzieri et al. (2011), for example, combined airborne LiDAR and multispectral imagery to estimate floodplain forest roughness and significantly improved water-level simulations. More recently, UAV imagery has been widely used to obtain high spatial resolution vegetation conditions over sandbars and floodplains (Prior *et al.* 2021), although its limited spatial coverage limits its applicability at reach or basin scales. Meanwhile, satellite imagery provides extensive spatial coverage and long series suitable for capturing seasonal vegetation dynamics, although its ability to resolve 3D structure typically depends on empirical relationships or machine learning techniques (Li *et al.* 2024).

Although both UAV and satellite imagery have been increasingly applied to vegetation monitoring for roughness estimation, each method exhibits inherent advantages and limitations (Guo *et al.* 2025). UAV-based observations provide high spatial resolution data, making them suitable for characterizing heterogeneous vegetation conditions over sandbars and floodplains. However, their limited spatial coverage, flight endurance, and logistical constraints restrict their applicability for large-scale or long-term monitoring. In contrast, satellite imagery provides extensive spatial coverage and consistent long-term time series, enabling the characterization of seasonal vegetation dynamics at the reach to basin scales, but it cannot directly obtain vegetation conditions and describe vegetation conditions using multispectral information. To address these limitations, several studies have attempted to integrate UAV and satellite data, using high-resolution UAV-derived vegetation structure as training or calibration information to upscale vegetation parameters across larger areas based on satellite imagery (Fortes *et al.* 2024, Guo *et al.* 2025). However, most existing studies focus on relatively simple or homogeneous vegetation types, and the roughness parameter is often correlated to a single vegetation type (Shu *et al.* 2023, Ferraz *et al.* 2024, Shi *et al.* 2025). Such approaches may be effective under uniform vegetation conditions, but are less suitable for floodplain environments, where grasses, shrubs, and woody vegetation commonly co-exist and jointly control flow resistance.

In this study, a combination of UAV measurements and satellite imagery is used to train a vegetation index - vegetation height relationship, which is then adopted for supporting vegetative roughness quantification from satellite imagery. The establishment of this relationship enables the quick estimation of vegetation roughness from satellite imagery without extra field measurements and pre-analysis field classification of vegetation.

Chapter 2 Study areas

The research focuses on two river reaches, namely the Vistula River (VR) in Poland and the Po River (PR) in Italy. Figure 2-1(B) and (C) show their locations in the watershed, while (D) and (E) show their respective digital elevation models (DEM).

The detailed description of the two study areas will be provided in sections 2.1 and 2.2, respectively.

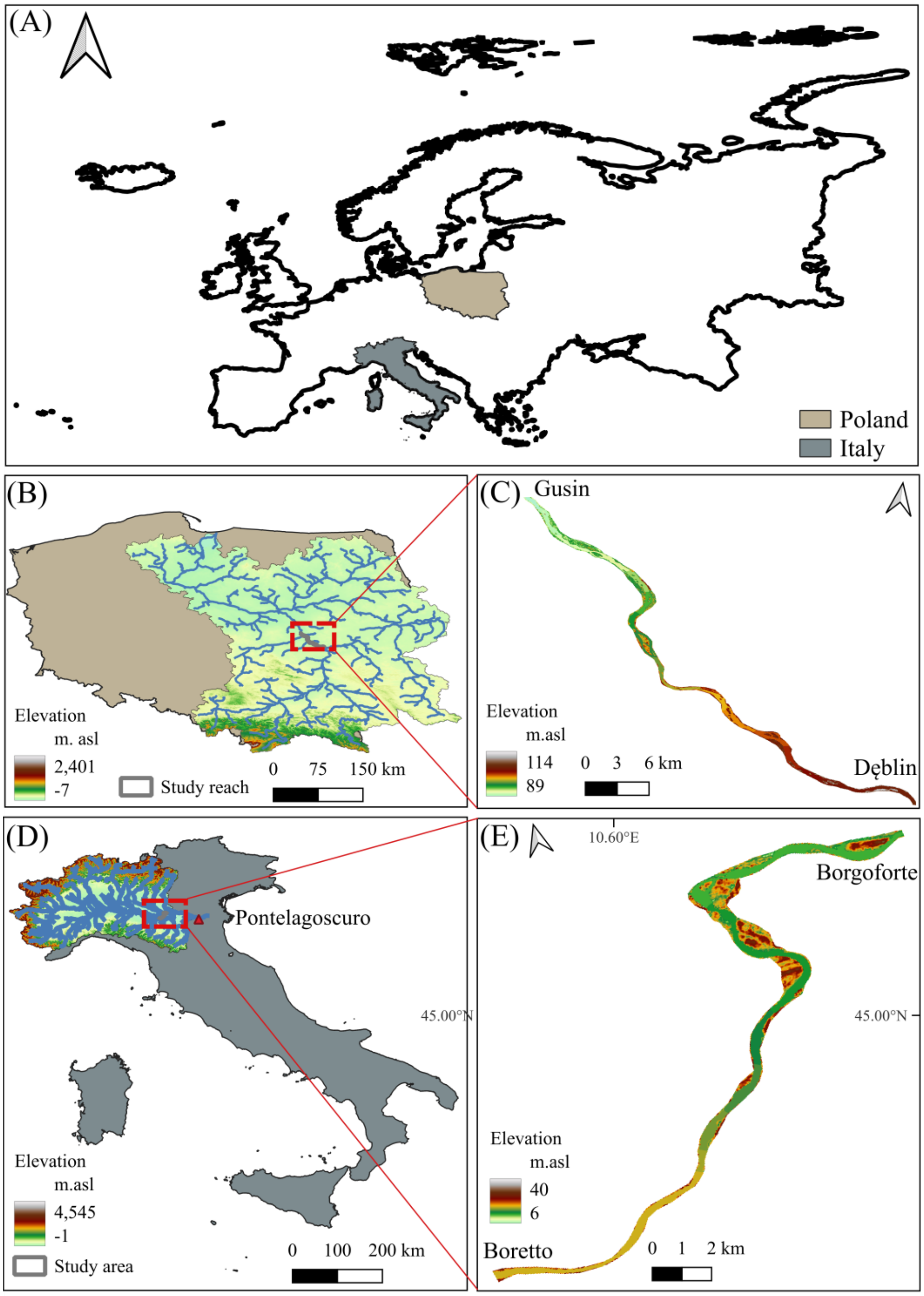

Figure 2-1. Overview of the two study areas. (A) The locations of Poland and Italy within Europe, (B) and (D) Watershed boundaries, and the locations of the study reaches for the VR (Poland) and the PR (Italy), respectively. (C) and (E) Digital elevation models (DEMs) of the two study reaches (sources: local water authorities).

2.1 Vistula River (Poland)

2.1.1 Vistula River

The Vistula River (Figure 2-1 (B)) is the longest watercourse in Poland, with a length of approximately 1,047 km (Cerkowniak *et al*. 2024, Osuch 2015), and its watershed is the second largest within the Baltic Sea basin, covering an area of about 183,176 km^2 (Räike *et al.* 2018).

Originating from the Barania Góra mountains of southern Poland and flowing northward until it flows into the Baltic Sea (Buszewski *et al.* 2005), the Vistula River has a pronounced asymmetrical drainage basin (Figure 2-1(B)) (Badora *et al.* 2023). The upper and middle reaches of the Vistula are dominated by right-bank tributaries, with a catchment area ratio of the right bank to the left bank of approximately 73:27 (Woźnica *et al.* 2023), while the distribution of the river network in the lower Vistula becomes more uniform (Badora *et al.* 2023). The upper reach of the Vistula is a mountain stream with a steep gradient, and is frequently impacted by flood events (Wyżga *et al.* 2018). The gradient decreases significantly in the middle Vistula (Sosnowska 2025), while in the lower reach, it is exceptionally low (around 0.018%) (Babiński and Habel 2013, Łajczak *et al.* 2021). This lower reach is characterized by extensive sandbars that hinder navigation (Kryniecka *et al.* 2022) and is impacted by spring floods caused by ice jams, which often damage embankments and bridges (Kordowski 2009). From a hydrological point of view, the Vistula River is characterized by common spring snowmelt floods and summer torrential rain floods.

The Vistula River Basin has a transitional climate between maritime and continental influences due to its location in a temperate climatic zone (Kubiak-

Wójcicka 2020), and the air temperature varies significantly throughout the year within the Vistula basin. The mean annual air temperature of the basin is 8.4°C, with mean monthly temperatures of -1.4°C in January and 18.4°C in July (Badora *et al.* 2023). The average annual precipitation across the Vistula basin is 678.8 mm, with a seasonal distribution of 117.8 mm in winter, 153.7 mm in spring, 247.1 mm in summer, and 160.0 mm in autumn (Kubiak-Wójcicka 2020). The average annual discharge (1951-2015) of the upper and lower Vistula are 341 m^3/s (Górnik 2020) and 1080 m^3/s, respectively (Bogdanowicz *et al.* 2021).

The soil composition of the Vistula River basin is diverse, mainly comprising approximately 41% sandy loams, 26% loamy sands, and 21% clays, collectively covering about 90% of the basin (Piniewski *et al.* 2017). When it comes to the land use/cover (LULC), according to the Corine Land Cover 2018 data (Copernicus Land Monitoring Service (CLMS) 2020), the Vistula basin is dominated by agricultural land: cropland constitutes approximately 58% of the total basin area, followed by forest (29%), grassland and pasture (8%), and orchards and plantations (4%) (Wojkowski *et al.* 2022).

2.1.2 Study reach

The reach between the gauging stations of Dęblin and Gusin stations (around 65 km, Figure 2-2) was selected for this study. This reach has an elevation that ranges between 89 and 114 m asl. The annual average discharges recorded at the Dęblin and Gusin stations from 1991 to 2024 are 486.18 m^3/s and 545.59 m^3/s, respectively. Apart from water bodies, the primary land use types within the study area are arable land and forest land, accounting for 12.74% and 20.89% of the total area, respectively.

Due to the distinctive geographic and climatic conditions, and its dynamic physical behavior, the middle Vistula experiences flood events rather frequently and is at high flood risk. (Kiczko *et al.* 2013). Functioning as a transitional zone between the upland areas upstream and the lowlands downstream, this reach annually accumulates substantial snowmelt runoff from the Carpathian Mountains during spring, leading to a pronounced snowmelt-induced flood season (Krasiewicz and Wierzbicki 2023). Meanwhile, intense convective storms in summer frequently bring localized heavy rainfall, which can trigger sudden rainstorm floods (Pietras and Pyrc 2025). These two dominant hydrological patterns establish the fundamental climatic drivers of flood occurrences in the region. Located in the middle course of the Vistula River upstream of the Polish capital Warsaw, this reach experiences less human influence than the section crossing the city, while being hydrologically similar to it. Consequently, it serves as a valuable reference for flood management in Warsaw.

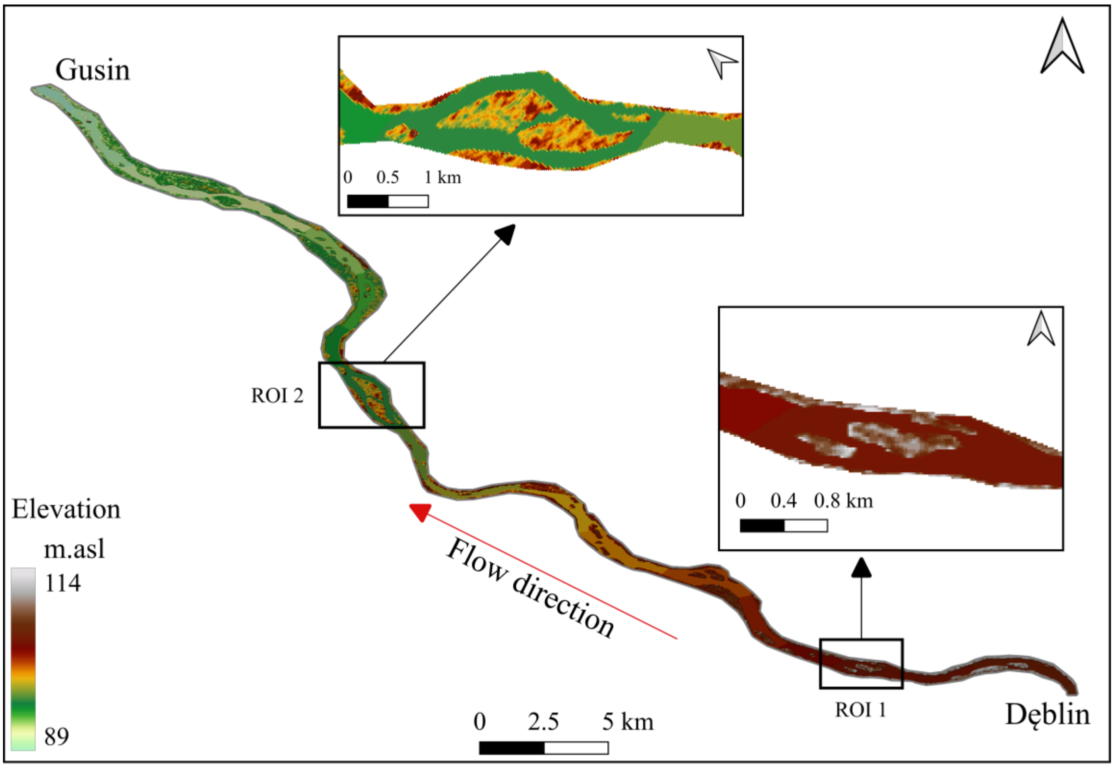

Figure 2-2. Overview of the Vistula River, with the two ROIs highlighted. The red arrow indicates the flow direction.

2.2 Po River (Italy)

2.2.1 Po River

The Po River (Figure 2-1(D)) originates from Pian del Re on the Monte Viso, in Piedmont, and flows eastward into the Adriatic Sea near Venice. It is the longest river in Italy, with a total length of approximately 651 km (Zanchettin *et al.* 2008). As the largest watershed in the country, the Po River basin covers an area of about 74,000 km^2, most of which (around 70,000 km^2) lies within Italy (Bozzola and Swanson 2014). The Po River basin is characterized by a heterogeneous orography, with an altitude varying from 0 to 4793 m asl.

Fed by tributaries originating from both the Alps and the Apennines, the Po River is supported by a network of more than 140 tributaries with a total length exceeding 6,700 km (Soana *et al.* 2019). From a hydrological point of view, this watercourse is characterized by two flood periods (spring and late autumn) and two periods of low flow (winter and summer) due to snowmelt and precipitation, respectively (Soana *et al.* 2023). According to the observed discharge at the Pontelagoscuro hydrological station (Figure 2-1 (D)), which is regarded as a benchmark for the discharge of the Po River, the annual average discharge from 1961 to 2025 is 1485 m^3/s, with a highest discharge of 9515 m^3/s observed on 21 October 2000 and a lowest discharge of 104 m^3/s occurred on 25 July 2022 (Montanari 2012).

The basin has a warm-temperate climate, owing to its location across the transition zone between the subcontinental climate of Central Europe and the Mediterranean climate (Soana *et al.* 2023). The average annual precipitation over the Po River basin is approximately 1,200 mm, ranging from a minimum of about 700 mm in the deltaic region to a maximum of around 2,000 mm in the Alpine sector (Vezzoli *et al.* 2015). Air temperature within the basin exhibits pronounced altitudinal variability, with mean annual temperatures of around 5 °C in high mountain areas and approximately 10–15 °C in the valley regions (Cavallini *et al.* 2024).

The spatial distribution of major soil types in the Po Basin has a clear geomorphic pattern. The upper terraces and foothills are characterized by more weathered and developed soils such as Luvisols and Cambisols, which typically exhibit good drainage properties (Hiederer 2013). In contrast, the floodplains and deltaic areas are dominated by Fluvisols, which are fertile, young soils composed of stratified layers of recent alluvial deposits.

The Po River Basin, particularly its lower plains and delta region, is one of the most intensively farmed areas in Europe and is dominated by agricultural land use, featuring intensive cultivation of rice, cereals, forage, and commercial tree plantations (Blasi *et al.* 2014). The land use/cover of the basin, as derived from Corine Land Cover 2018 data (Copernicus Land Monitoring Service (CLMS) 2020), is dominated by agricultural and forested areas. Cropland is the predominant land cover type, representing 41.07% of the basin, forest ranks second at 38.61%, grassland and urban areas account for 11.90% and 7.10%, respectively, while bare land and water bodies together comprise less than 2%.

2.2.2 Study reach

Located in the midstream of the Po River, a 30-km reach between the Boretto and Borgoforte stations was selected as the study area (Figure 2-3). The elevation of this reach ranges from 13 to 37 m a.s.l. According to records from the Boretto and Borgoforte hydrological stations (1961–2025), the mean annual discharge is 1,212.74 m^3/s at Boretto and 1,354.51 m^3/s at Borgoforte. The maximum daily flows at these stations occurred on 19 October 2000, reaching 11,459.60 m^3/s and 11,752.52 m^3/s, respectively. In contrast, the minimum daily discharges were recorded on 23 July 2022, at 127.52 m^3/s and 140.94 m^3/s, respectively. In the reach, the LULC is predominantly water bodies and forest land, accounting for 55.6% and 41.85% of the total area, respectively. In contrast, agricultural land and construction land together account for only about 2.6% (2.28% and 0.3%, respectively).

Since this reach has been shaped by long-term human interventions, including sediment extraction, navigation-oriented river training works, and upstream flow regulation (Goldsmith *et al.* 2014), it has experienced river degradation and associated morphological adjustments. These alterations have resulted in a relatively deep and confined main channel, while the interaction between the main channel and adjacent floodplains is constrained by embankments. Under such hydraulically constrained conditions, variations in vegetation-related roughness can exert a disproportionately strong influence on flow conveyance and water levels, especially during flood events. Consequently, this reach provides a suitable natural setting to investigate the role of vegetation in modulating flood dynamics under realistic yet controlled river conditions.

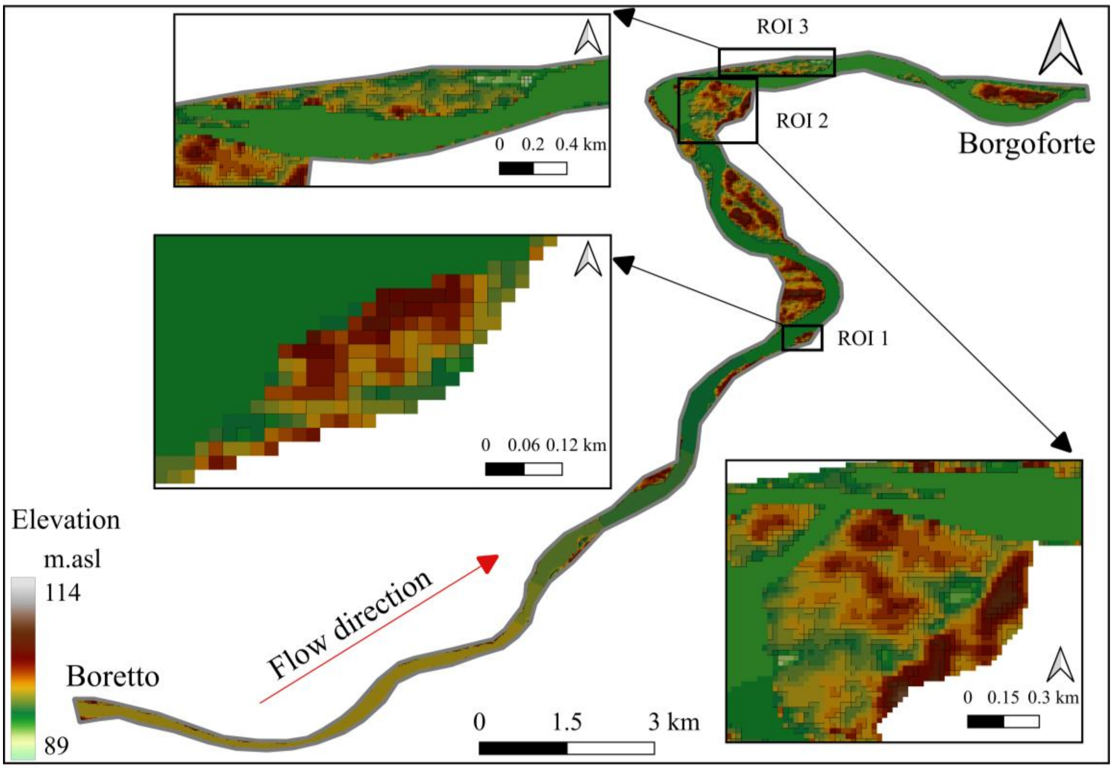

Figure 2-3. Overview of the Po River, with the three ROIs highlighted. The red arrow indicates the flow direction.

Chapter 3 Data and Methods

The study workflow is composed of seven main steps, as illustrated in Figure 3-1. A brief summary is provided below, while each step is described in detail in the following sections.

1. The first step is to conduct field measurements with an uncrewed aerial vehicle (UAV). In this case, a DJI Mavic 3 Multispectral was used.
2. The second step is to categorize and process the collected data.
3. Machine learning models are then trained to establish the relationships between multispectral vegetation indices (MVIs) and vegetation height (h).
4. Fourthly, satellite-based MVIs are calculated via Google Earth Engine (GEE).
5. The vegetation roughness is, thus, estimated by substituting satellite-based MVIs into the trained model and subsequently calculating roughness into Manning's n (n) formulation.
6. Using Manning's formula, satellite-based vegetation roughness is calculated.
7. Finally, a hydrodynamic model is applied to investigate the impact of the estimated vegetation roughness on the reach hydrodynamics.

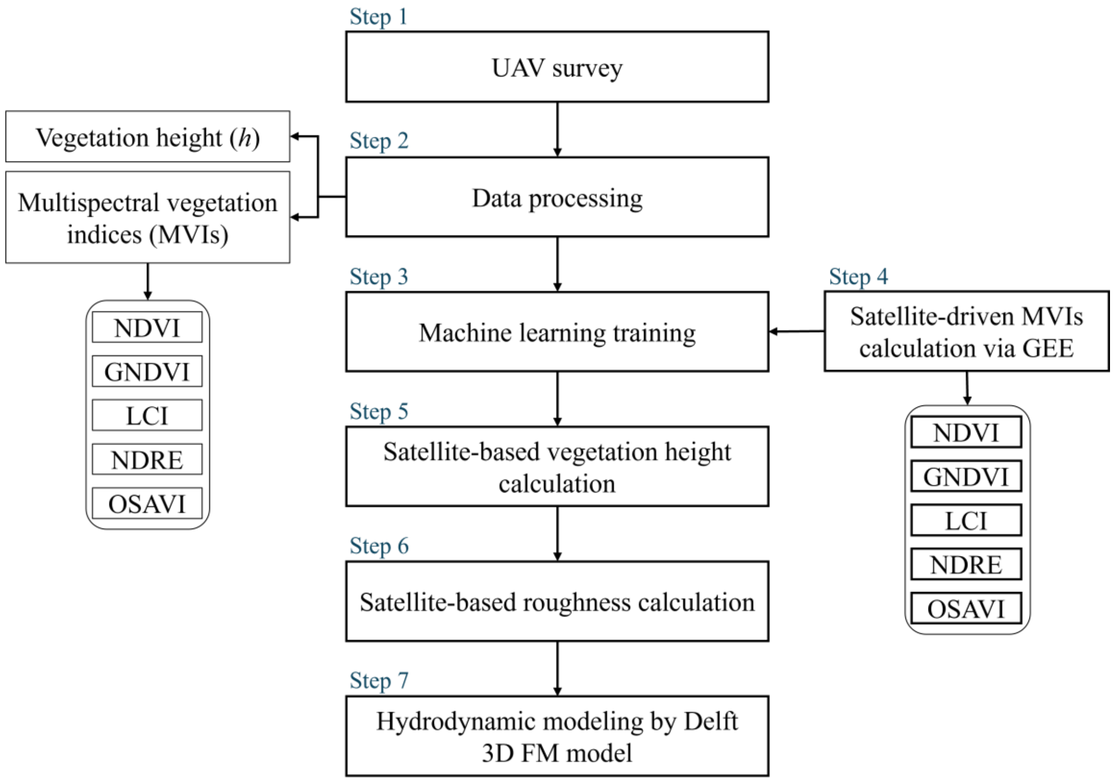

Figure 3-1. Flowchart illustrating the seven main steps of this research.

3.1 UAV field measurement

A DJI Mavic 3 Multispectral (M3M) UAV (SZ DJI Technology Co., Ltd., Shenzhen, China), equipped with a 20 MP RGB main camera and four 5 MP multispectral cameras (Figure 3-2), was used to investigate the study reaches and collect vegetation conditions. The RGB sensor is a 20-megapixel 4/3″ CMOS sensor with an 84° field of view, and the multispectral imaging system comprises four independent 5-megapixel 1/2.8″ CMOS sensors, each with a field of view of 73.91° (DJI 2022). Four cameras cover the green, red, red edge, and near-infrared bands, with central wavelengths of 560 nm, 650 nm, 730 nm, and 860 nm and bandwidths of 50 nm, 53 nm, 55 nm, and 85 nm, respectively (Kuurasuo 2025). With a takeoff weight of 1050 g and a rated flight endurance of 43 minutes, the DJI M3M can operate in wind speeds up to 12 m/s and within a temperature range of -10 °C to 40 °C. The drone features a built-in RTK module, enabling centimeter-level high-precision positioning. Additionally, its integrated sunlight sensor captures solar irradiance and records it in the image files, allowing for light compensation of the image data during 2D reconstruction. The sunlight sensor not only enables more accurate MVI results but also improves the consistency and overall accuracy of data acquired over time (Tan *et al.* 2024). Furthermore, it is equipped with an omnidirectional vision and infrared sensing system for obstacle avoidance (Carp 2023).

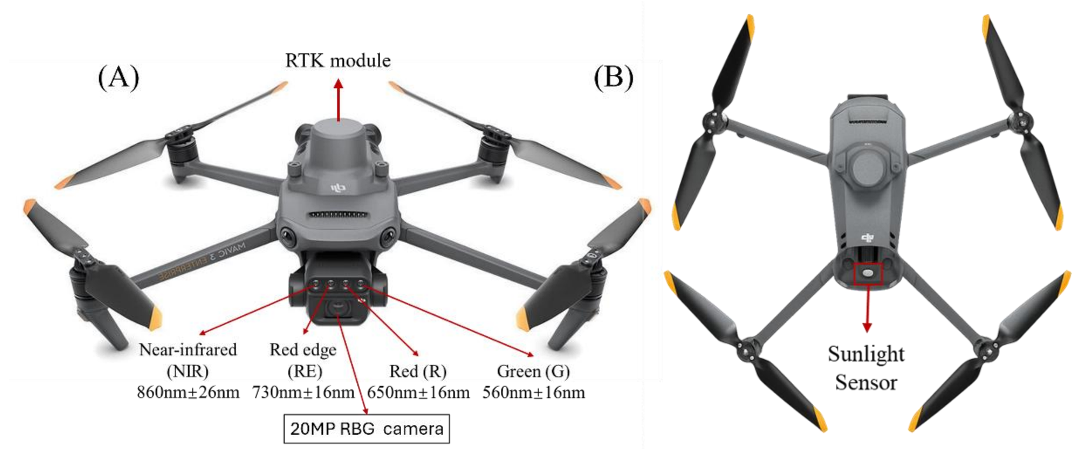

Figure 3-2. Illustrative image of the unmanned aerial vehicle (UAV) used in this study during the field surveys.

Field measurements were conducted at two study sites (the Po River and Vistula River) on 27 May and 29 May, 2025, respectively. Both days featured overcast conditions. A photograph of the measurement day is shown in Figure 3-3.

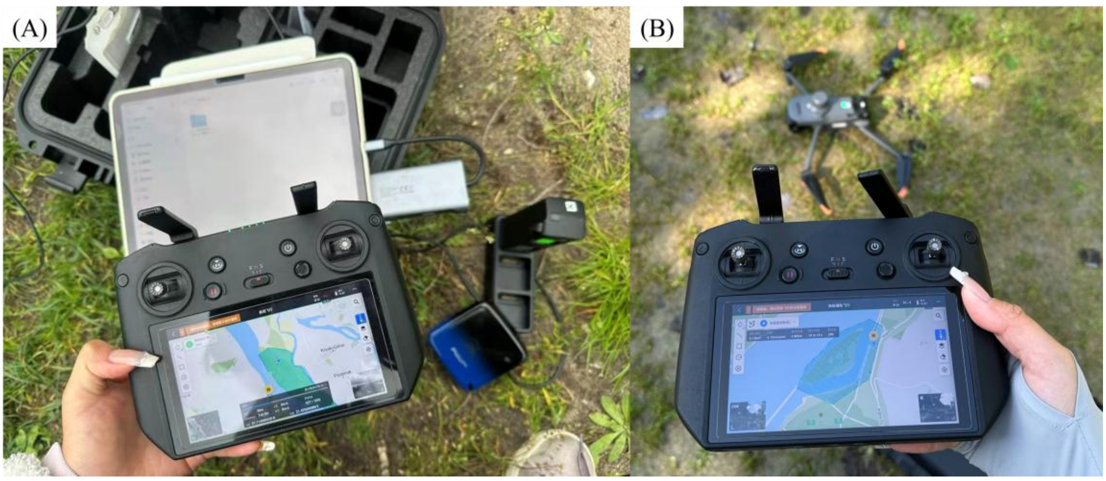

Figure 3-3. Field photographs showing the measurement using UAV (A) Vistula Reach and (B) Po Reach.

During the mission, the DJI Pilot 2 application was used to operate the UAV. This included, but was not limited to, pre-programming the flight route (Figure 3-4) and setting the coordinates for the takeoff and return points, as well as the flying height that was set to 90 m. The flight paths of ROI 1 in Poland and ROI 2 in Italy partially overlap because the sandbars are relatively large and cannot be fully covered within the endurance of a single flight. Therefore, a second flight was conducted, with its starting point partially overlapping the endpoint of the first flight.

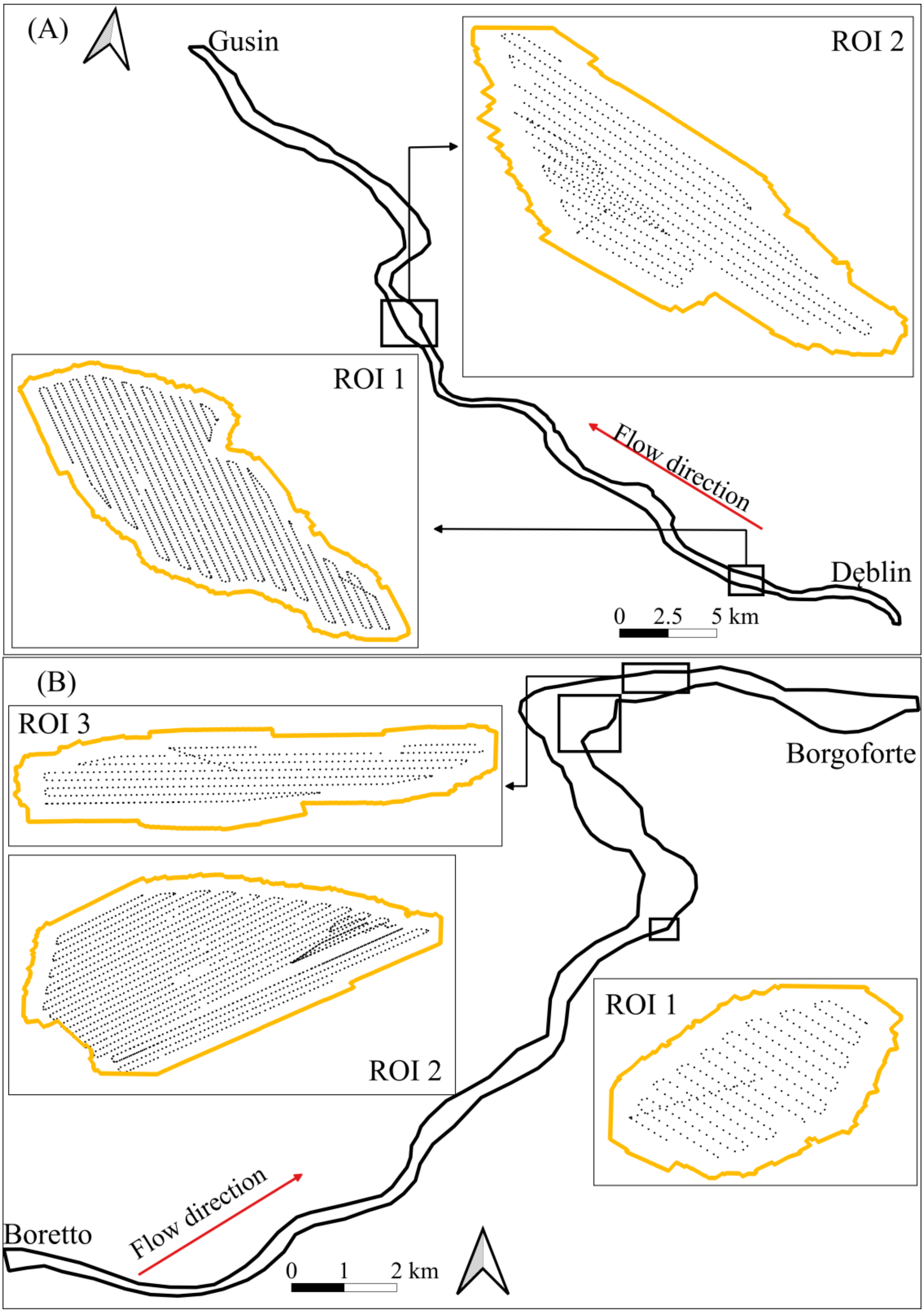

Figure 3-4 (A) and (B) show the UAV flight paths of the surveys conducted over the Vistula and Po rivers, respectively. The red arrow indicates the flow direction. Each point represents an image captured by the UAV.

3.2 Processing of the drone data

3.2.1 Multispectral indices

Given that the study aims to investigate how vegetation condition could be derived from drone flights and correlated to satellite-derived information, five multispectral vegetation indices (MVIs) are selected: Normalized Difference Vegetation Index (NDVI), Green Normalized Difference Vegetation Index (GNDVI), Leaf Chlorophyll Index (LCI), Normalized Difference Red Edge Index (NDRE), and Optimized Soil Adjusted Vegetation Index (OSAVI).

3.2.1.1 NDVI

As the most widely used and classic vegetation index in remote sensing, the Normalized Difference Vegetation Index (NDVI) was first proposed in 1974 by Rouse et al. (Rouse *et al.* 1974) and is defined as equation (3-1).

$$NDVI = \frac{NIR-R}{NIR+R} \tag{3-1}$$

where NIR and R are the near-infrared band and the red band, respectively.

With a value range from -1 to 1, NDVI quantitatively assesses vegetation density, growth vigor, and biomass by calculating the normalized difference between the NIR and R (Rouse *et al.* 1974). A positive NDVI value indicates the presence of vegetation, and higher values generally represent more lush and healthy vegetation, while a negative value means that the land is without vegetation (Ruan *et al.* 2022). Although NDVI is easy to calculate and able to reduce the influence of illumination and topographic variations to some extent, it tends to saturate in areas with high biomass and is susceptible to soil background effects and atmospheric conditions (Mutanga and Skidmore 2004).

3.2.1.2 GNDVI

The Green Normalized Difference Vegetation Index (GNDVI) is an important variant of NDVI (Gitelson *et al.* 1996), replacing the red band in the formula with the green band (equation (3-2)).

$$GNDVI = \frac{NIR-G}{NIR+G} \tag{3-2}$$

where G is green bands.

Because of the small reflectance peak in G and strong reflectance in NIR of the healthy vegetation, GNDVI is more sensitive to changes in leaf chlorophyll content, particularly at high chlorophyll concentrations (Gitelson *et al.* 1996).

3.2.1.3 LCI

Proposed by Gitelson et al. in 2005, the Leaf Chlorophyll Index (LCI) is specifically designed for the high-precision estimation of leaf chlorophyll content, and is defined by Equation (3-3).

$$LCI = \frac{NIR-RE}{NIR-R} \tag{3-3}$$

where RE is red edge band.

By utilizing the extreme sensitivity of RE to chlorophyll concentration, LCI maximizes the reflection of chlorophyll absorption features while remaining relatively insensitive to leaf structural variations and background interference (Datt 1999). LCI has been proven to perform better in precisely assessing plant physiological status (Main *et al.* 2011, Liu *et al.* 2019).

3.2.1.4 NDRE

Aiming to address the saturation problem of NDVI during the mid-to-late growth stages, when crop canopies become dense, Barnes et al. proposed the Normalized Difference Red Edge Index (NDRE) in 2000 (Barnes *et al.* 2000). Similar to LCI, NDRE also utilizes RE, but it employs the standard normalized difference form, as defined in Equation (3-4).

$$NDRE = \frac{NIR-RE}{NIR+RE} \quad (3\text{-}4)$$

Due to the high sensitivity of the red-edge band to changes in leaf internal structure and chlorophyll content, NDRE can penetrate denser canopies and retrieve information from middle and lower leaves, which is highly suitable for monitoring crops in their mid-to-late growth stages (Barnes *et al.* 2000, Clevers and Gitelson 2013).

3.2.1.5 OSAVI

The Optimized Soil Adjusted Vegetation Index (OSAVI) was introduced by Rondeaux et al. (Rondeaux *et al.* 1996) to minimize the interference of bare soil background reflectance on the vegetation signal when vegetation cover is moderate or low (Equation (3-5)).

$$OSAVI = \frac{NIR-R}{NIR+R+0.16} \tag{3-5}$$

By adding an optimized soil adjustment factor to the NDVI formula, OSAVI can effectively lower the influence of soil brightness variations, thereby reflecting vegetation information more accurately (Steven 1998). Considering variations in soil moisture and roughness, Rondeaux et al. simulated various soil types and conditions and found that setting the adjustment factor to 0.16 minimized the soil background interference on the vegetation signal most effectively (Rondeaux *et al.* 1996).

3.2.2 Data processing

During UAV-based remote sensing data acquisition, the collected imagery is inevitably affected by atmospheric inhomogeneity and intrinsic sensor-related factors, which may lead to image distortion and accuracy deviations. Therefore, to ensure the effective use of UAV imagery in subsequent analyses, preprocessing of the raw data is required. The preprocessing workflow mainly consists of three core steps, which are: i) image mosaicking, ii) geometric correction, iii) image cropping. These procedures aim to eliminate factors that degrade data quality, enhance the overall clarity and accuracy of the imagery, and produce more complete and reliable remote sensing products.

Image processing was conducted using the DJI Terra software (DJI 2024). Firstly, a new project and workspace were created in DJI Terra, and the multispectral processing mode was selected. All acquired remote sensing images were stored in the same directory and imported into the software. Camera parameters were then adjusted to ensure accurate image mosaicking. In the aerial triangulation settings, the standard scene and single-machine computation options were selected, and the distance to the imaged objects was set according to the flight altitude. The 2D map option was subsequently enabled to perform radiometric calibration, and illumination normalization was carried out using the onboard light sensor of the DJI M3M. After these steps, orthophotos, multispectral index layers, as well as digital surface models (DSM) and digital elevation models (DEM) were automatically generated and exported by the software.

The vegetation height (*h*) is estimated from the difference between DSM and DEM (Figure 3-5). The DSM-DEM approach used to calculate the vegetation height has been tested by many researchers and is defined as reliable (Radke *et al.* 2020, Tang *et al.* 2021, Zhao *et al.* 2021, Zhang *et al.* 2024, Guo *et al.* 2025).

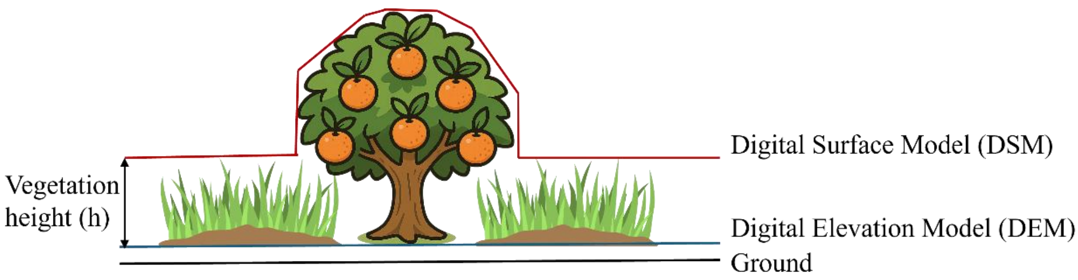

Figure 3-5. Sketch of the computation of vegetation height as DSM-DEM.

The flight coverage is often extended to ensure complete coverage of the study area when conducting UAV field measurements. Based on satellite imagery from 26 May 2025, the boundaries of the sandbar were extracted for use in cropping the captured images (Landsat 9 dataset). QGIS 3.40 was thus used to crop the generated remote sensing images, removing redundant areas and retaining only the imagery corresponding to the study area.

All layers, including the DSM, DEM, and MVIs, were overlapped, and the center coordinate of each grid cell was taken as the spatial location of that cell. Each grid cell was treated as an individual data sample. The vegetation height (h), together with the corresponding MVIs for each point, was exported and used as input data for the subsequent model training.

3.3 Machine learning model

To estimate *h* from UAV-derived samples, this study developed a machine-learning model. The main steps of the model training workflow are illustrated in Figure3-6, while all procedures were implemented in MATLAB.

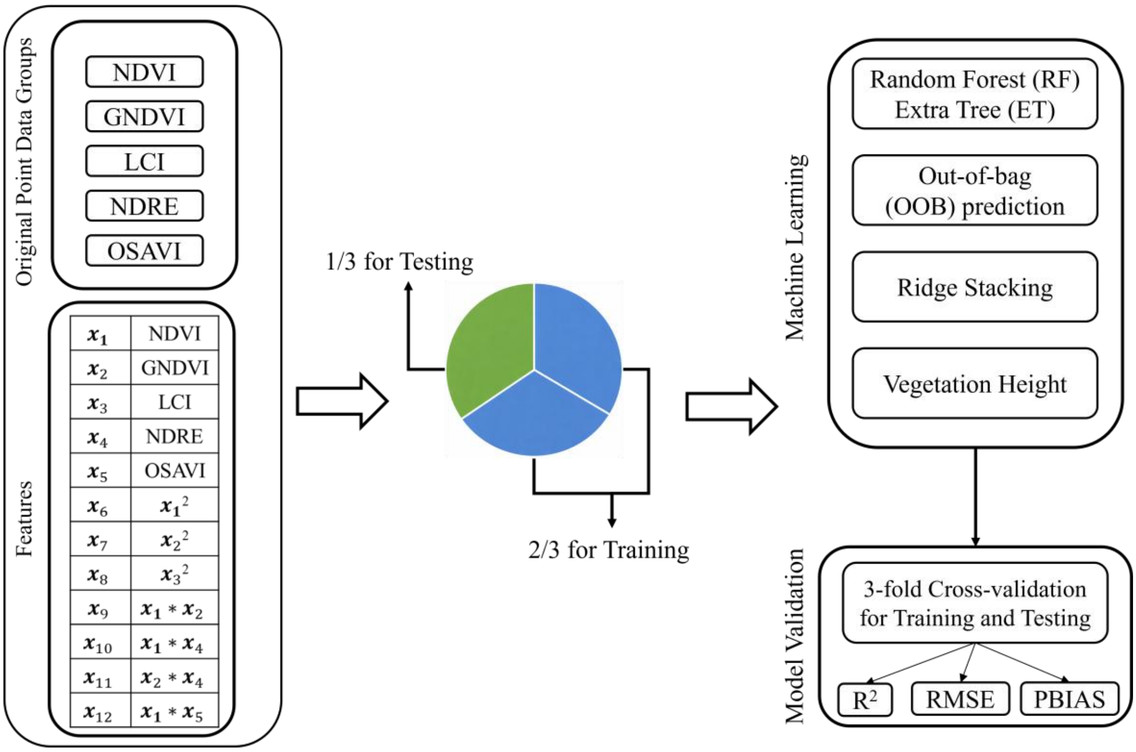

Figure 3-6. The flowchart of the machine learning model.

Firstly, a pre-processed file including *h* and positional information for each grid cell (treated as single points, as described in the previous section) is imported. The dataset is then filtered to remove points with missing values and those with vegetation height values less than or equal to zero, as these represent UAV errors in data acquisition. Usually, the vegetation height value cannot be zero, however, due to the vertical uncertainties in UAV-structure-from-motion (UAV-structure) reconstruction and minor co-registration mismatches between DSM and DEM, some values are lower than zero (James and Robson 2012, Westoby *et al.* 2012). Given that typical vertical errors of UAV-derived DSM are within the centimeter to decimeter range (Westoby *et al.* 2012), these negative values were considered reconstruction artefacts rather than real terrain features and were therefore removed prior to model training.

Except for the original MVIs, a limited set of features (Table 3-1) was introduced to capture potential non-linear relationships between spectral information and h. Squared terms were included to account for saturation effects commonly observed in reflectance-based indices at higher canopy density. A small number of interaction terms combining indices with complementary sensitivities were also tested to better represent joint structural and physiological variability. It is worth noting that not all possible combinations were included in order to avoid redundancy, strong collinearity, and unnecessary model complexity. Only those features that provided consistent improvements under three-fold cross-validation were retained in the final model.

Table 3-1. Features (x_1–x_{12}) used for the machine-learning model.

Features	**Definition**
x_1	NDVI
x_2	GNDVI
x_3	LCI
x_4	NDRE
x_5	OSAVI
x_6	NDVI^2
x_7	GNDVI^2
x_8	LCI^2
x_9	NDVI*GNDVI
x_{10}	NDVI*NDRE

x_{11}	GNDVI*NDRE
x_{12}	NDVI*OSAVI

To characterize local differences and improve model generalization, to each point a site identifier was assigned, according to the sandbar on which it is located. Specifically, points located in ROI 1 and ROI 2 in Poland were assigned site identifiers 1 and 2, respectively, while points located in ROI1 to ROI3 in Italy were assigned site identifiers 3 to 5. Model training and evaluation were then conducted independently under three configurations: Poland-only, Italy-only, and All (Poland + Italy).

Model performance was evaluated using an outer three-fold cross-validation (outer 3-fold CV) scheme. In each outer fold (Fold *i*), the dataset was split into a training subset comprising two-thirds of the data and a validation subset comprising the remaining one-third. By providing a more stable estimate of generalization error than a single train/test split, while maintaining a manageable computational cost, and by being simple to use, broadly applicable, and less sensitive to the randomness of one-off data partitioning, 3-fold cross-validation is widely adopted for risk/error estimation and model selection (Arlot and Celisse 2010). Namely, a 3-fold CV scheme splits the data into three parts, trains on two parts, and validates on the remaining part in rotation, and then averages the three validation results, ensuring that every sample serves as unseen validation data once, which is generally closer to an out-of-sample assessment than a single split (Arlot and Celisse 2010). Actually, 3-fold cross-validation in random forest modeling is not statistically optimal, but it provides a practical compromise between computational cost, estimation stability, and engineering feasibility (Wilimitis and Walsh 2023). Compared with a single train/test split, 3-fold cross-validation substantially reduces the uncertainty caused by random data partitioning, while it limits the number of model trainings to three, compared with 5- or 10-fold cross-validation, which is particularly important when the dataset is large or when individual model runs are computationally expensive (Kohavi 1995, Arlot and Celisse 2010). Similar to previous studies (Kohavi 1995, Speiser 2021, Noviana and Itje Sela 2024), Random Forest (RF) is here used for feature selection, parameter comparison, or multi-scheme experiments, where the main interest lies in the relative performance differences between models rather than in obtaining the most precise estimate of the generalization error. Therefore, 3-fold cross-validation already provides sufficiently stable performance ranking, while ensuring that each sample is used once as independent validation data, making it a commonly adopted baseline validation strategy (Ziegel *et al.* 2009, Bertalan *et al.* 2022, Chen *et al.* 2022, Abedin *et al.* 2026). In the study, models were trained exclusively on the training subset and used to generate predictions for the corresponding validation subset.

Random Forest (RF) and Extra Trees (ET) regressors were used as base learners (Breiman 2001, Geurts *et al.* 2006). Both methods are based on bootstrap sampling, whereby each tree is trained on a random subset of the original dataset, leaving a fraction of samples unused during the construction of individual trees (Biau and Scornet 2016). Predictions obtained for these unused samples are referred to as out-of-bag (OOB) predictions and provide an internal estimate of model generalization without the need for an explicit train–validation split (Breiman 2001, Biau and Scornet 2016).

For the Vistula-only and Po-only cases, bootstrap sampling was enabled, and OOB predictions were adopted as an approximate out-of-fold (OOF) signal. These region-specific datasets originated from a single river system and exhibited relatively homogeneous hydromorphological characteristics. In this setting, relying on OOB predictions may introduce implicit information leakage across regions, particularly when such predictions are subsequently used within a stacked learning framework (Ziegel *et al.* 2009, Biau and Scornet 2016).

In contrast, for the Vistula+Po case, data from both the Vistula and the Po were combined, resulting in a larger and more heterogeneous dataset. Therefore, relying on OOB predictions could introduce implicit information leakage across regions, particularly when predictions are later used in a stacked learning framework (Wolpert 1992). To avoid this issue and ensure an unbiased meta-learning signal, OOF predictions were generated explicitly using an inner three-fold cross-validation, such that each prediction was produced by a model that had not been trained on the corresponding sample (Van Der Laan *et al.* 2007, Ziegel *et al.* 2009).

The resulting OOF predictions from RF and ET were concatenated to form a two-dimensional meta-feature vector, which served as input to the subsequent stacking stage. This strategy balanced computational efficiency for region-specific models with robustness against information leakage in the merged configuration (Wolpert 1992, Van Der Laan *et al.* 2007).

The resulting OOF meta-features were standardized and passed to a Ridge regression meta-learner (Ridge, $\alpha = 10^{-4}$) to perform stacking. On top of the stacking output, an optional isotonic regression calibration step was applied to enforce monotonic consistency. The calibrator was activated only when the calibrated OOF R^2 demonstrated a measurable improvement over the uncalibrated stacking R^2, when the calibrated OOF R^2 exceeded the uncalibrated stacking OOF R^2 by more than 0.01 (Kuhn and Johnson 2013), thereby reducing the risk of overfitting induced by calibration.

Model performance is quantified using the coefficient of determination (R^2, Equation (3-6)), the root mean square error (*RMSE*, Equation (3-7)), and the Percent bias (*PBIAS*, Equation (3-8)).

$$R^2 = 1 - \frac{\sum_{i=1}^{N}(y_i - \bar{y}_i)^2}{\sum_{i=1}^{N}(y_i - \bar{y})^2} \tag{3-6}$$

$$RMSE = \sqrt{\frac{1}{n}\sum_{i=1}^{N}(y_i - \bar{y}_i)^2} \tag{3-7}$$

$$PBIAS = 100 * \frac{\sum_{i=1}^{N}(\bar{y}_i - y_i)}{\sum_{i=1}^{N} y_i} \tag{3-8}$$

Where y_i denotes the observed value of the i-th sample, $\bar{y}_i$ is the corresponding model prediction, $\bar{y}$ represents the mean of the observed values, and N is the number of samples.

The R^2 is defined as the proportion of the total variance in the observed data that is explained by the model in a statistical sense, typically derived within a least-squares regression framework. It reflects the overall goodness-of-fit of the model in terms of variance explanation rather than mere correlation (Legates and McCabe 1999). An R^2 of 1 indicates perfect agreement between predictions and observations, whereas $R^2 = 0$ implies that the model performs no better than using the mean of the observations (Kvålseth 1985).

PBIAS is a statistical bias metric that quantifies the average tendency of model predictions to deviate from observations, indicating whether the model systematically overestimates or underestimates the target variable (Moriasi *et al.* 2007). Different from R^2, *PBIAS* does not describe correlation or variance explanation, but focuses on the mean directional error of predictions. Owing to its sensitivity to systematic bias, *PBIAS* is widely used as a complementary metric alongside variance- or correlation-based performance measures (Pandit *et al.* 2025).

RMSE indicates the average magnitude of the differences between predicted and observed values, with larger errors being penalized more heavily. *RMSE* has the same units as the target variable, which makes it straightforward to interpret. Lower *RMSE* values indicate higher predictive accuracy, while high *RMSE* values indicate overestimation or underestimation, depending on the sign.

As the last step, a model bundle was trained using the full dataset, and the trained model was saved as .joblib type files. The bundle contains trained RF and ET base models, the scaler, the Ridge meta-learner, the optional isotonic calibrator, and the optional Stage-2 residual model together with its weight.

3.4 Calculation of satellite-based VMIs via GEE

To meet the needs of rapidly extracting useful information from enormous remote sensing Earth observation datasets, cloud-based high-performance computing platforms, such as Microsoft Azure HPC and Materials Cloud, have developed rapidly in recent years (Chou *et al.* 2024, Le Piane *et al.* 2024). Compared with the traditional workflow of local processing and analysis after downloading, cloud computing platforms enable users to process data directly on the platform, which significantly lowers the entry barrier for remote sensing data utilization, as well as the computational effort, and greatly improves efficiency.

Among various cloud computing platforms, the Google Earth Engine (GEE) platform, featuring a global geospatial database with petabyte-scale data and a cloud-based analytical service system supporting high-performance parallel computing, is currently one of the most advanced and widely used platforms in the field of Earth sciences (Tamiminia *et al.* 2020). Built upon Google's globally distributed data centers and massive server clusters, GEE offers powerful capabilities in data storage, parallel computation, spatial analysis, and result visualization (Gorelick *et al.* 2017). By accessing Google Earth Engine via its web-based interactive development environment and application programming interfaces (APIs), users can process and analyze complex data without having to install specialized remote sensing or GIS software locally (Gorelick *et al.* 2017).

GEE integrates a wide range of public geospatial datasets, which have been preprocessed in a standardized manner and can be directly accessed for analysis. The datasets include multi-source remote sensing imagery such as the Landsat series, Sentinel series, MODIS, and regional high-spatial-resolution imagery, topographic and elevation data, including SRTM and ArcticDEM, land cover and land use datasets like GlobCover and NLCD. GEE gives users access to historical meteorological and future projection data, including land surface temperature, air temperature, precipitation, evapotranspiration, and weather observations and forecasts, population datasets such as WorldPop and the Gridded Population of the World (GPW), and also other important raster datasets like global forest canopy height products, and selected vector and statistical datasets. In addition, GEE allows users to upload their own vector or raster data to GEE Assets for unified cloud-based management and further analysis (Fu *et al.* 2021).

GEE (Figure 3-7) integrates a large number of built-in functions and algorithms for remote sensing and geospatial analysis, covering the entire workflow from basic numerical operations to advanced spatial analysis and machine learning. These functions can be broadly categorized into numerical operations, array/matrix operations, machine learning, per-pixel image operations, kernel operations, other image operations, data reducers, geometry operations, table/collection operations, vector/raster operations, and other data types (Tamiminia *et al.* 2020). The computational paradigms include per-pixel, per-feature, per-image, per-image-tile, per-tile, context-dependent, stream-based, and scatter/gather processing (Gorelick *et al.* 2017).

In conclusion, by integrating powerful cloud-based parallel computing capabilities with freely accessible remote sensing datasets and mature data processing and machine learning algorithms (Gorelick *et al.* 2017), GEE provides strong technical support for regional to global-scale Earth system science research (Tamiminia *et al.* 2020). The platform significantly improves the efficiency of remote sensing data processing and analysis (Boothroyd *et al*. 2021a), accelerates algorithm testing and model iteration (Boothroyd et al. 2021b), and enables rapid global-scale analyses and applications that were previously difficult to achieve using traditional computing environments (Gorelick *et al.* 2017).

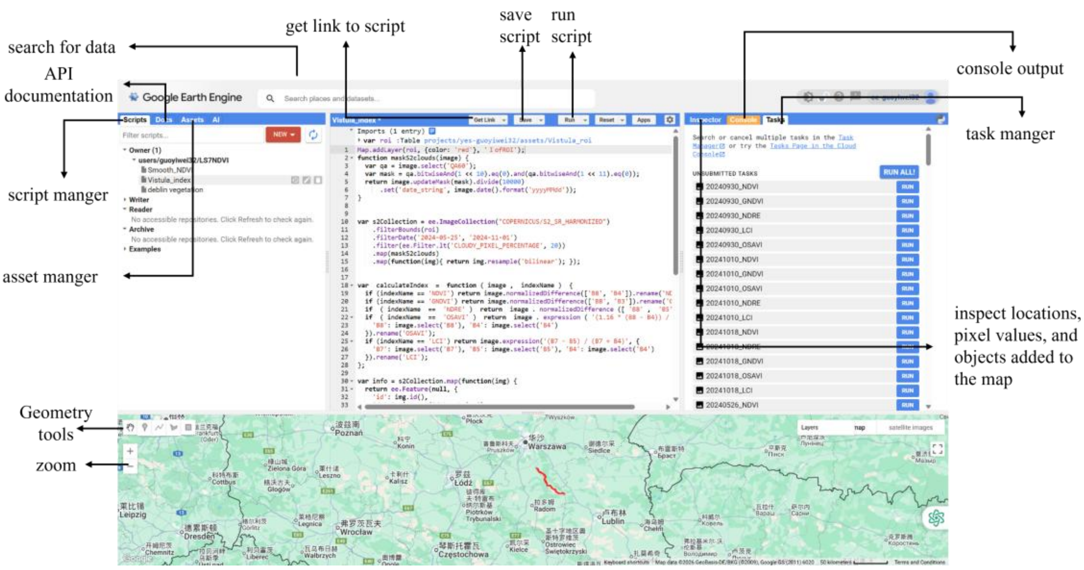

Figure 3-7. Example of Google Earth Engine (GEE) web-based Interactive Development Environment (IDE).

As shown in Figure 3-8, the calculation of the five indices (MVIs, section 3.2.1) on the GEE platform comprises five main steps, which are i) data input and selection, ii) initial image quality control, iii) multispectral indices calculation, iv) clipping index imagery to the study area, and v) data output.

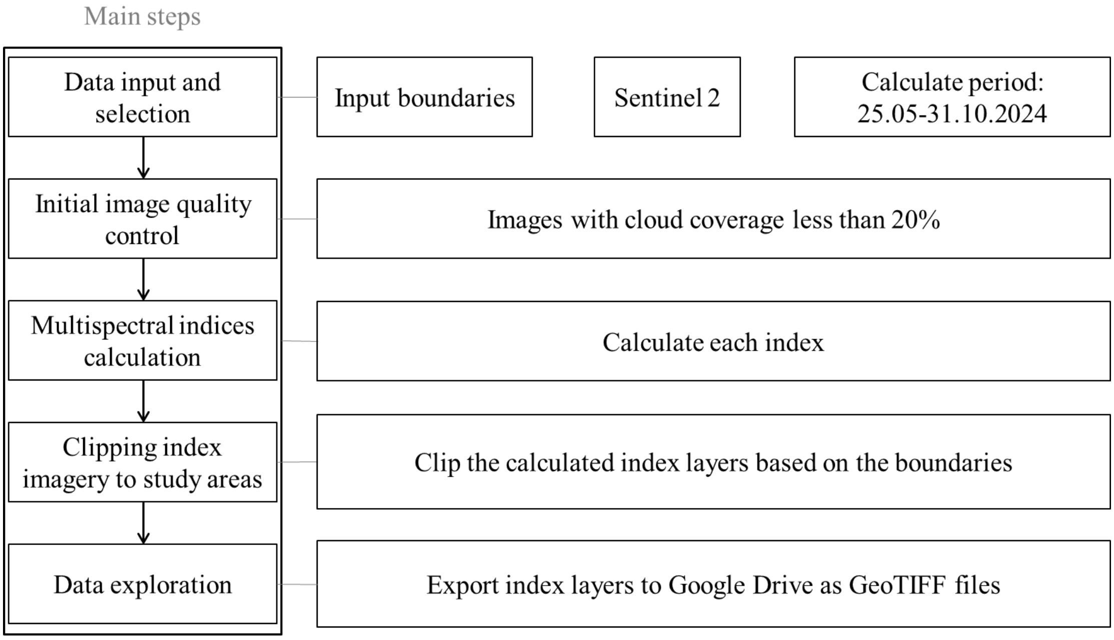

Figure 3-8. The flowchart of processing MVIs via the GEE platform.

The vegetation indices required in this study rely on red-edge spectral information. Among commonly used satellite remote sensing datasets (e.g., Landsat series and Sentinel-2), only Sentinel-2 provides red-edge bands (Gascon *et al.* 2017, Wulder *et al.* 2019), and, therefore, the Sentinel-2 Level-2A surface reflectance product was chosen on the GEE platform. The shapefile boundaries of the two study areas were then uploaded to the platform as an asset. The image collections were then constrained to the selected regions to ensure that all subsequent processing steps were restricted to the study area. The images acquired between 25 May 2024 and 01 November 2024, were selected to capture the main vegetation growth period within the study region, following literature evidence (Boothroyd *et al*. 2021, Szyga-Pluta *et al.* 2023, Kubiak-Wójcicka *et al.* 2024). The satellite imagery on the survey date is shown in Figure 3-9.

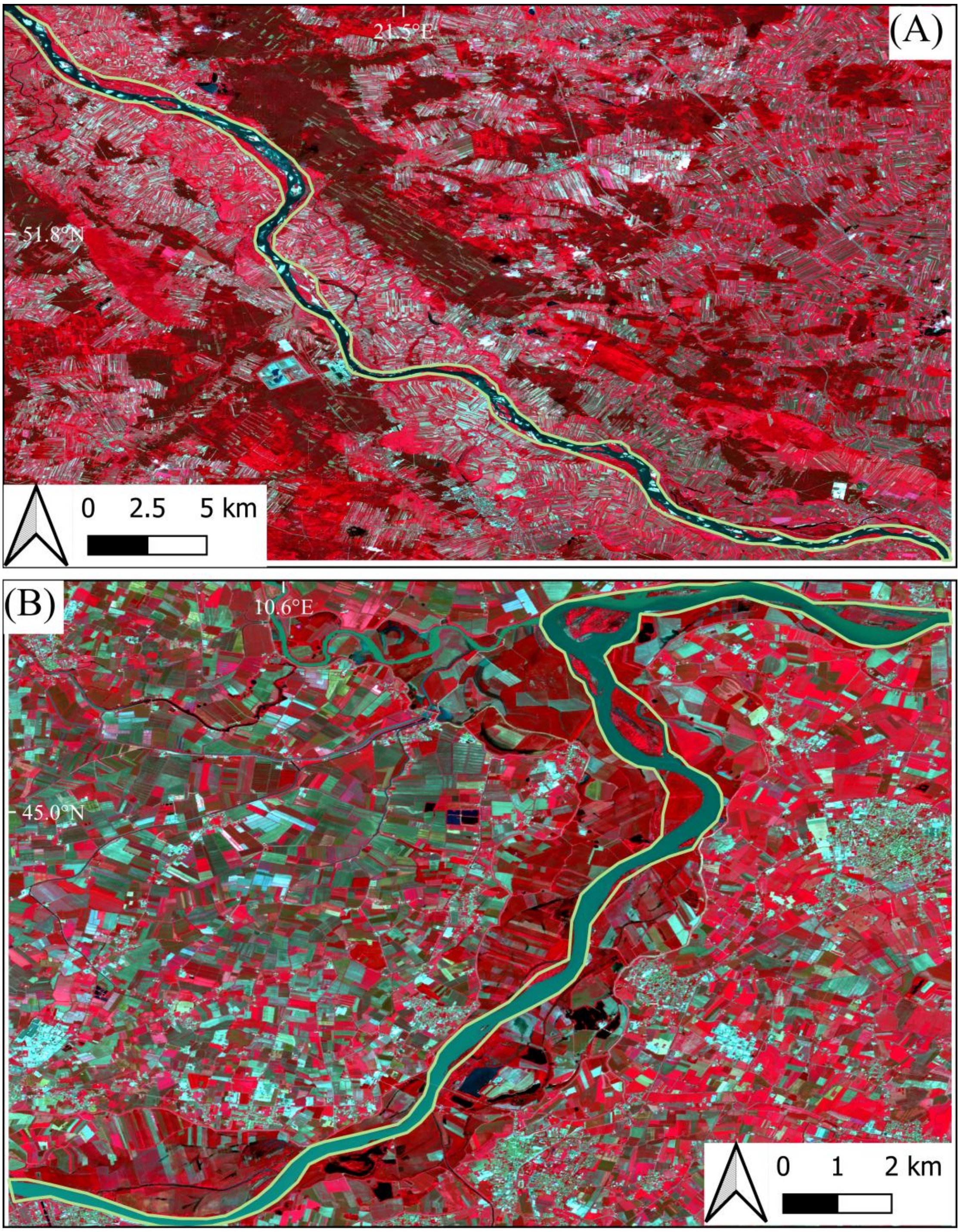

Figure 3-9. False color combination of Sentinel-2 imagery of (A) Vistula Reach and (B) Po Reach on 25.05.2024. The spectral band combination is 5-4-3, which represents the vegetation cover in red.

All images were processed to remove clouds. Bits 10 and 11 of the QA60 quality assurance band provided with the Level-2A product, which indicate opaque cloud and cirrus contamination, respectively, were used to identify pixels unaffected by opaque clouds and cirrus clouds. Pixels with both bits equal to zero were considered cloud-free and retained for further analysis (Claverie *et al.* 2018). This cloud removal procedure effectively minimizes residual atmospheric contamination and improves the robustness of vegetation index calculations, particularly for multi-temporal analyses (Claverie *et al.* 2018).

Pixel values were converted to physically meaningful surface reflectance by applying the standard scaling factor (division by 10000) after removing clouds, since Sentinel-2 reflectance values are stored as integers. Because Sentinel-2 multispectral bands are provided at different native spatial resolutions, red-edge bands are delivered at 20 m, while the visible (red and green) and near-infrared bands are available at 10 m (Drusch *et al.* 2012), the spatial resolution of the imagery was resampled to 10 m using bilinear interpolation before index calculation (Delegido *et al.* 2011, Immitzer *et al.* 2016). Resampling all bands to a common 10 m grid prior to index calculation ensures that all vegetation indices are computed on a consistent spatial support, avoids inconsistencies caused by mixing information from different native resolutions, and improves the spatial correspondence with UAV-derived vegetation height during pixel-level comparison (Zhu *et al.* 2017). At the same time, a 10 m resolution is sufficient to describe vegetation patterns on riverine sandbars without over-interpreting sub-pixel variability (Woodcock and Strahler 1987).

After the preparatory work was completed, five selected vegetation indices were calculated using equations (3-1) to (3-5). Each index layer was clipped to the study area's boundary to remove regions outside the area of interest. To preserve the independence and traceability of each index, they were generated as individual single-band images rather than being combined into a single multi-band composite.

Finally, all index layers were exported as GeoTIFF files to a Google Drive folder, adhering to a consistent naming convention (e.g., 20240525_NDVI.tif). The exports were configured with a spatial resolution of 10 m, and the WGS 84 geographic coordinate system (EPSG:4326) was imposed.

3.5 Satellite-based vegetation height estimation

To evaluate the applicability of satellite-based vegetation height estimation, satellite-derived vegetation height was compared with UAV-derived vegetation height.

Satellite-derived vegetation height was obtained by inputting vegetation indices derived from Sentinel-2 imagery on the Google Earth Engine platform into the trained machine learning model. The calculation procedures followed exactly the same steps as described in Section 3.4.

After index calculation, the satellite-derived vegetation index products were spatially co-registered with the UAV-derived vegetation height data and resampled to a common projection (EPSG:4326) and spatial resolution (10 m) to ensure pixel-level consistency and comparability. Each satellite grid cell was then treated as an independent analysis unit. The corresponding vegetation index values were extracted and used as input variables for the machine learning model that had been previously trained using UAV-derived vegetation height observations, yielding satellite-scale vegetation height estimates. It is emphasised that this step represents a model application and validation procedure rather than a re-training of the model.

For the validation analysis, only grid cells identified as vegetated were included in the comparison in order to avoid potential bias introduced by non-vegetated surfaces such as bare soil or water bodies. A pixel-by-pixel comparison was then conducted between the satellite-derived vegetation height estimates and the UAV-derived vegetation height observations.

Model performance was quantitatively evaluated using R^2, *RMSE*, and *PBIAS*, which have been described in detail in previous sections. The combination of these three metrics evaluates the model's ability to estimate vegetation height based on remote sensing data and provides a methodological basis for subsequent applications involving satellite time series and the derivation of dynamic vegetation height and roughness parameters for hydrodynamic modelling.

3.6 Calculation of vegetation roughness

The vegetation roughness is calculated based on equations 3-9 and 3-10 (Chaulagain *et al.* 2022). In this study, the n values are calculated from the C values. Although both Chézy and Manning's n are supported in Delft3D-FM, Manning's n is selected to enhance the general applicability of this approach, as many hydrodynamic models commonly use Manning's n to represent flow resistance (Chow 1959).

$$n = \frac{1}{C} {H_h}^{\frac{1}{6}} \tag{3-9}$$

$$C = \sqrt{\frac{1}{C_b^2} + \frac{C_D m D H_h}{2g}} + \frac{\sqrt{g}}{0.41} \log(\frac{H_h}{h}) \tag{3-10}$$

Where C is the composite Chézy resistance coefficient [$m^{1/2}$/s], C_b is the bed-related Chézy coefficient [$m^{1/2}$/s], C_D is the drag coefficient [-], m is vegetation stem density [-], D is the characteristic stem diameter [m], H_h is the water depth [m], g is the gravitational acceleration [9.81 m^2/s], h is the vegetation height, and n is Manning's roughness coefficient [s/$m^{1/3}$].

In this study, the bed n for both simulation reaches was set to 0.06, which represents the calibrated optimal bed roughness. Based on Equation (3-9), the C_b for each cell was calculated accordingly. According to previous studies, a C_D value of 1 was adopted (Chaulagain *et al.*, 2022). The vegetation density parameter (m) was derived from UAV imagery, with a stem diameter (D) of 0.02 m assigned to cells with NDVI values between 0 and 0.5, and 2 m assigned to cells with NDVI values greater than 0.5. The h for each cell corresponds to the vegetation height estimated in Section 3.5.

3.7 Hydrodynamic modelling: Delft3D FM

3.7.1 Overview of the Delft3D FM model

Developed by WL Delft Hydraulics from Delft University, the Delft3D Flexible Mesh (Delft3D FM) model is a powerful open-source numerical modelling suite based on the Delft3D modelling framework (Lee *et al.* 2024, Akter *et al.* 2025, Deltares 2025, Rajendiran *et al.* 2025). The software integrates multiple modules, including hydrodynamics (D-Flow FM), hydrology (D-Hydrology), real-time control (D-Real Time Control), morphodynamics (D-Morphology), wave modelling (D-Waves), and water quality simulation (D-Water Quality), and is widely applied in engineering studies of coastal, estuarine, and riverine environments (Zhu 2022, López-Ramade *et al.* 2023). Delft3D FM features a highly integrated system architecture and user interface, in which model setup, numerical computation, and post-processing are unified within a single platform, as illustrated by the initial interface of the software shown in Figure 3-10.

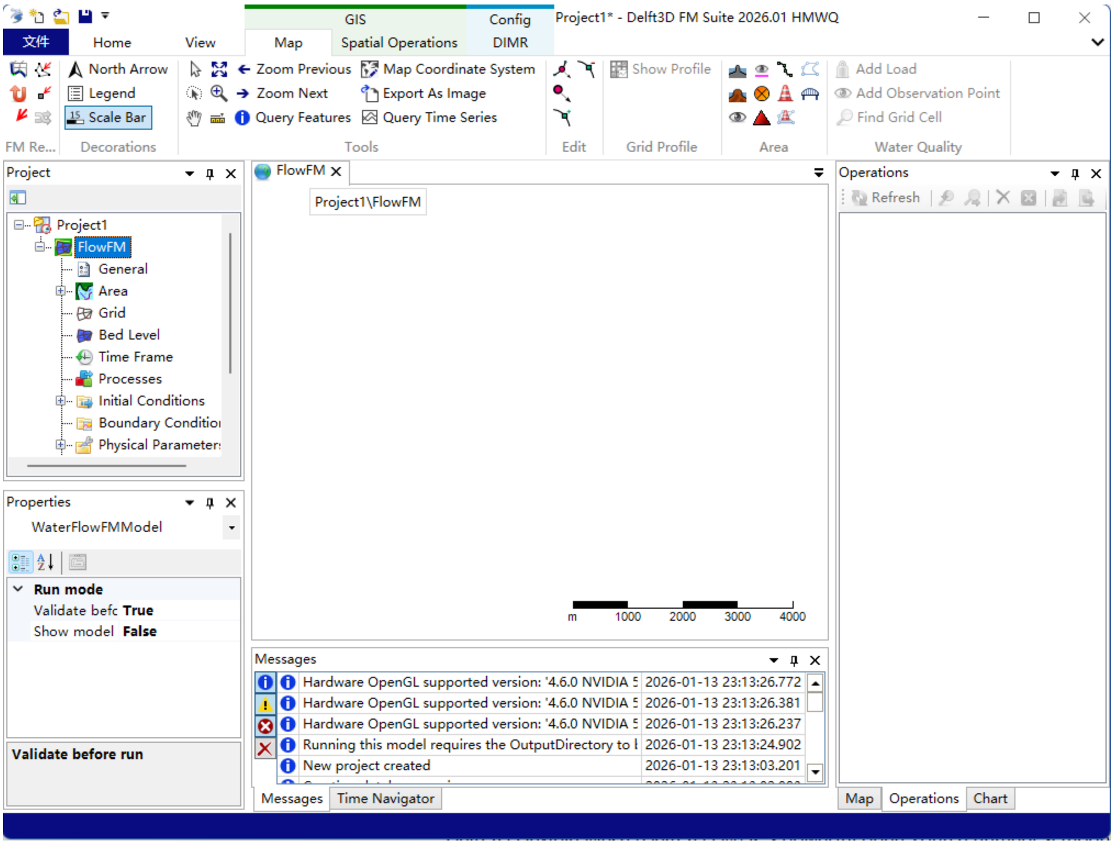

Figure 3-10. The interface of the Delft3D FM software.

Different from traditional structured-grid models, Delft3D FM allow to apply both a structured grid and an unstructured mesh system that is not constrained by regular row–column arrangements (Kernkamp *et al.* 2011, Deltares 2024). In this second case, computational cells can be coupled in any direction and location (Kernkamp *et al.* 2011), and various cell types, such as triangles, pentagons, and hexagons, can be flexibly adopted (Deltares 2024), which significantly enhances mesh flexibility and geometric adaptability in large-scale domains with complex topography (Casulli and Walters 2000).

Delft3D FM does not apply the traditional Alternating Direction Implicit (ADI) time-integration scheme, but instead implicitly solves the continuity equations for all computational nodes within a single combined system, while selected advection terms are treated explicitly in time. As a result, the time step is dynamically adjusted according to the Courant–Friedrichs–Lewy (CFL) stability criterion, which ensures that flow information does not propagate across more than one computational cell within a single time step, thereby maintaining numerical stability and physically consistent solution accuracy on the unstructured mesh (Ferziger and Perić 2002, Deltares 2024, Yu *et al.* 2025). In the D-Flow FM module, advection processes are computed explicitly, and the maximum CFL per time step is strictly limited to $\leqslant 0.7$ to ensure numerical stability and accuracy (Deltares 2024, Akter *et al.* 2025).

3.7.2 Governing Equations of the Two-Dimensional (2D) Hydrodynamic Model

The Delft3D FM numerical modelling system is used to simulate incompressible flow, for which the continuity condition $\nabla \cdot u = 0$ is satisfied. By vertically integrating the governing equations over the total water depth, the depth-averaged continuity equation is derived and solved to construct a two-dimensional depth-averaged hydrodynamic model.

The depth-averaged continuity equation is given by equation (3-11):

$$\frac{\partial h}{\partial t} + \frac{\partial hu}{\partial x} + v\frac{\partial hv}{\partial y} = Q_f \tag{3-11}$$

Where u and v denote the depth-averaged velocity components in the Cartesian system, with u representing the streamwise component and v the crosswise one, h indicates the water level, and Q_f represents the net water flux per unit area due to precipitation and evaporation.

The depth-averaged momentum equations in the horizontal directions can be expressed as equations (3-12) and (3-13).

$$\frac{\partial u}{\partial t}+u\frac{\partial u}{\partial x}+v\frac{\partial u}{\partial y}-f_u=-\frac{1}{\rho}P_x-\frac{gu\sqrt{u^2+v^2}}{C^2h_1}+F_x+F_{Sx}+M_x \tag{3-12}$$

$$\frac{\partial u}{\partial t}+u\frac{\partial v}{\partial x}+v\frac{\partial v}{\partial y}-f_v=-\frac{1}{\rho}P_y-\frac{gv\sqrt{u^2+v^2}}{C^2h_1}+F_y+F_{Sy}+M_y \tag{3-13}$$

Where u and v are the velocity components in the x- and y-directions, respectively, ρ is the water density [kg/m³], P_x and P_y denote the hydrostatic pressure gradients [m²/s], f_u and f_v represent the Coriolis force terms, F_x and F_y describe the imbalance of horizontal Reynolds stresses [m²/s], M_x and M_y account for the effects of external momentum sources or sinks [m²/s], and F_{sx} and F_{sy} represent the influence of secondary flow on the depth-averaged velocity [m²/s], in which shear stresses are incorporated through the depth-averaged nonlinear acceleration terms. Furthermore, C denotes the bed roughness coefficient, h_1 is the water depth [m], g is the gravitational acceleration [m²/s], and t represents time [s].

3.7.3 Model setting

This study focuses on the main river channel, including the vegetated sandbars located within the channel. The modelling domain is restricted to the in-channel area that is regularly affected by flowing water, where vegetation can directly influence hydraulic resistance. This study thus concentrates on vegetation growing on channel bars and does not extend to the entire floodplain. Vegetation outside the main channel is not considered in this modelling framework, as these areas are generally not exposed to continuous channel flow, and consistent time-varying vegetation data are not available at that scale. Therefore, the dynamic roughness approach developed in this study represents a channel-scale parameterization of vegetation effects within the main river channel, rather than a full channel-to-floodplain model.

Figure 3-11 illustrates the main steps involved in running the Delft3D FM model.

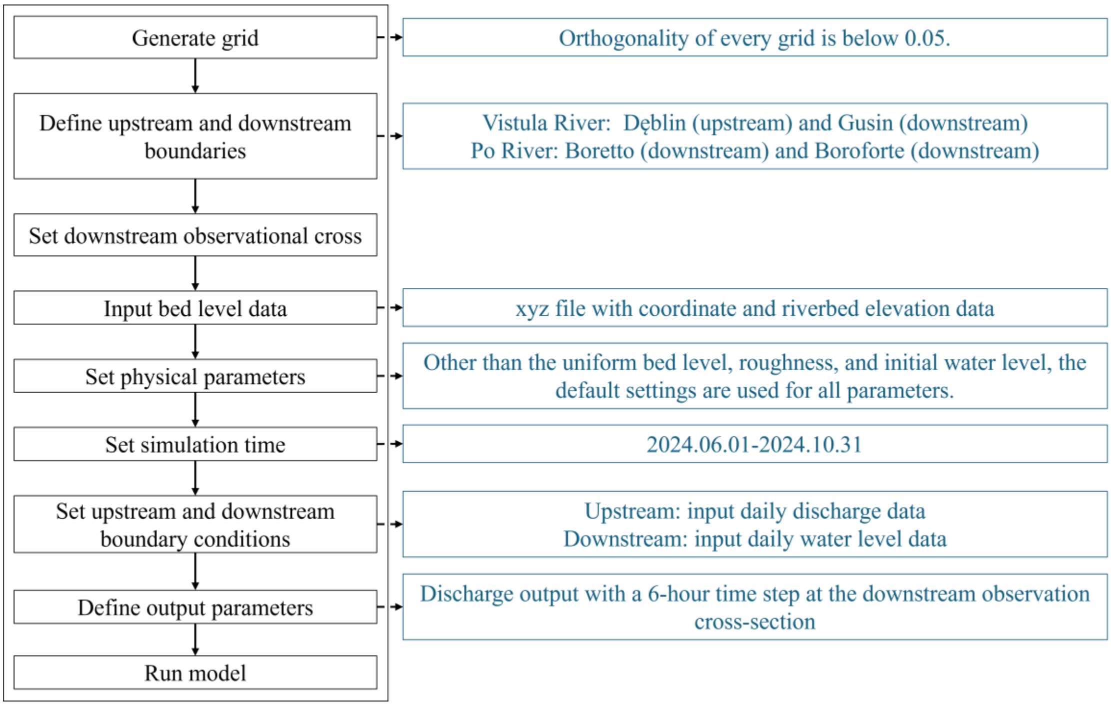

Figure 3-11. Numerical modelling flow chart.

The first and basic step is to create the grid. Although Delft3D FM supports unstructured meshes, a structured grid was intentionally adopted in this study (Figure 3-11) because the river reach exhibits a relatively regular and continuous channel geometry, for which a structured mesh is sufficient to resolve the dominant hydrodynamic processes, guaranteeing a proper reliability without compromising hydrodynamic accuracy. Although the study reach includes curved river sections, the channel geometry remains continuous and can be adequately represented using a structured curvilinear grid for hydrodynamic simulations (Hosseini *et al.* 2011). In addition, the use of a structured grid improves computational efficiency, also facilitating a consistent comparison between different roughness parameterizations (Hoch *et al.* 2018).

Since the accuracy of flux calculations in the finite-volume formulation is affected by grid orthogonality, poor orthogonality might introduce numerical diffusion and reduce the accuracy of mass and momentum conservation (Deltares 2025). Moreover, because advection is treated explicitly and constrained by the CFL condition, low grid orthogonality may limit the allowable time step or even cause numerical instability, making good mesh orthogonality essential for reliable simulations.

Therefore, the orthogonality of all computational grids used in this study was maintained below 0.05, following the recommendations of Deltares (Deltares 2020). The structured grid was designed with spatially varying grid spacing, with finer resolution applied in the main river channel and sandbar areas to better resolve bathymetric variability and flow dynamics, while coarser grid spacing was used in the floodplain to reduce computational cost (Lesser *et al.* 2004, Roelvink *et al.* 2009, Deltares 2024). Secondly, the upstream and downstream boundaries are defined, and an observation cross-section is drawn at the downstream boundary (Figure 3-12).

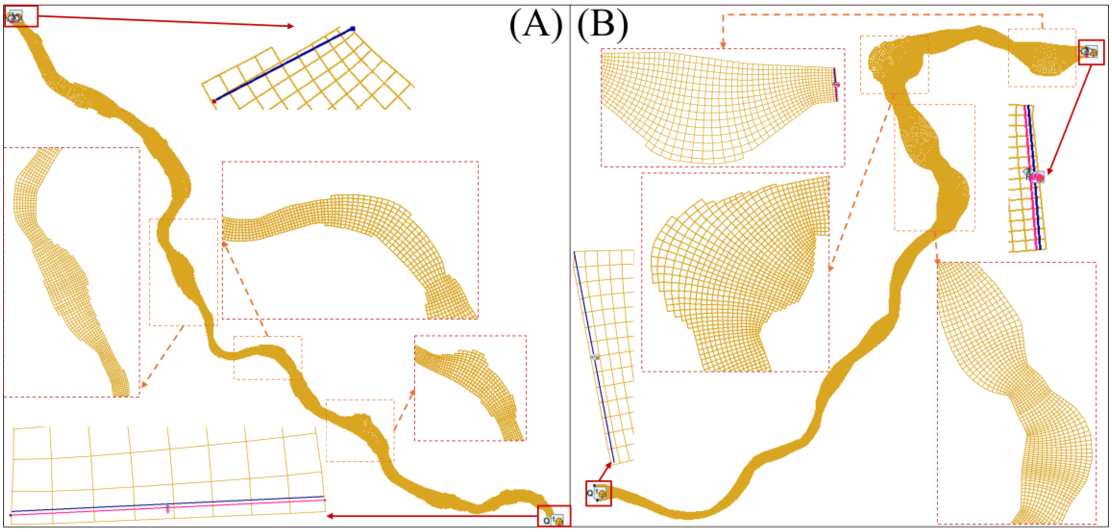

Figure 3-12. Modelling grids for the two case studies: Main channels of the (A) Vistula River and (B) Po River reaches. Blue lines represent the upstream and downstream boundaries, while the pink lines indicate the observation cross-sections at the downstream reach. Selected parts of the grid are zoomed for clarity.

Thirdly, an XYZ file containing pre-processed coordinate (XY) and riverbed elevation (Z) data of the main channel is used as model input. As the XYZ points were generally irregularly distributed and did not fully cover the computational domain, missing elevation values were interpolated using a triangulation-based method. Therefore, a Delaunay triangulation was first constructed from the input points, and linear interpolation was then applied within each triangle to generate a continuous riverbed elevation surface. The bed elevation maps of two reaches were retrieved from the local water authorities and are shown in Figure 3-13. This method has been widely adopted in previous Delft3D FM and river hydrodynamic modelling studies to reconstruct bathymetry from irregular survey data (Kernkamp *et al.* 2011, Deltares 2024). It is worth noting that the model allows for defining the slope (Figure 3-14) but, if the bed elevation data is provided as XYZ input like in this case, the model does not use the bed level set in the physical parameters (Deltares, 2024), but the actual elevation model (Figure 3-13).

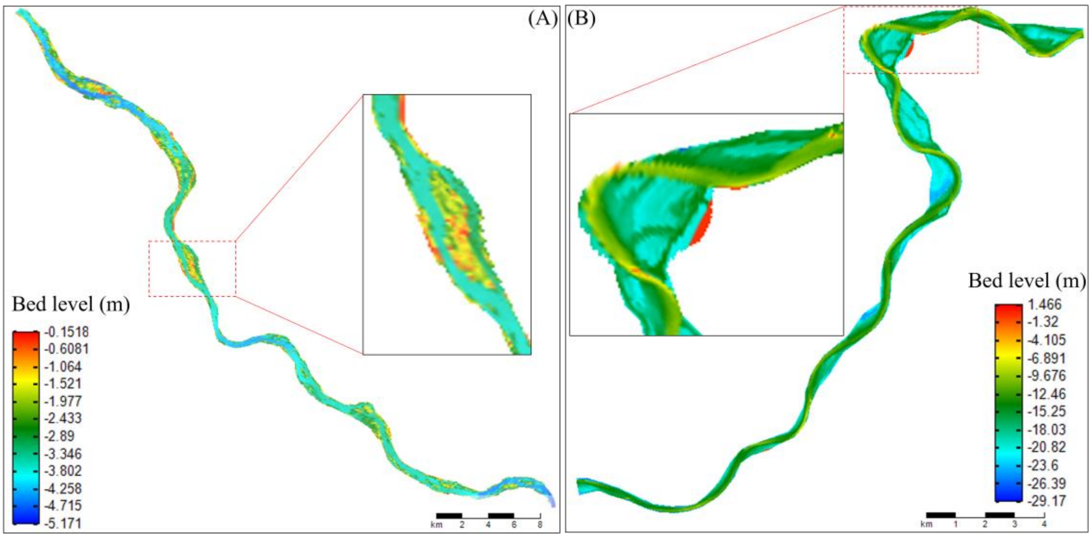

Figure 3-13. Bed elevation maps of two reaches used in the Delft3D FM model as input: (A) Vistula Reach and (B) Po Reach. Data was gathered from local water authorities. The zoomed areas are shown as examples to illustrate variations in riverbed elevation.

The fourth step is to set the physical parameters and the simulation time. Except for the uniform bed level, roughness, and initial water level, default settings are used for all other parameters and shown in Figure 3-14. The upstream water level at the beginning of the simulation period is set as the initial water level, which is assumed equal to the measured water level at the upstream gauging stations.

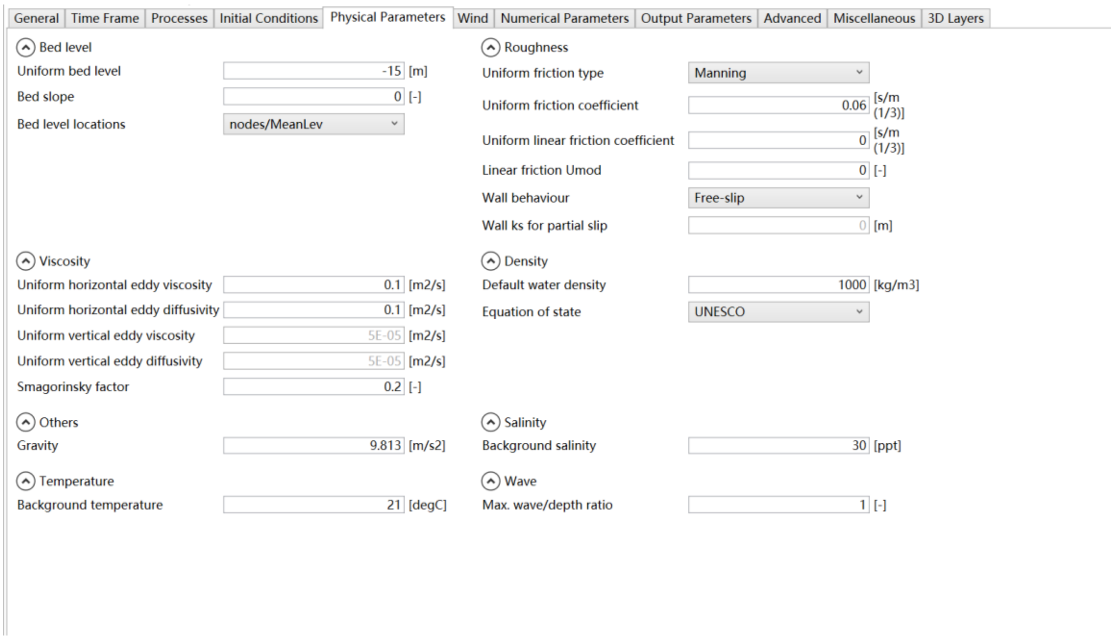

Figure 3-14. An example showing the physical parameters setting tab of the Delft3D FM software. Noting that the bed level parameters (Uniform bed level, bed slope, and bed level locations) are not used if the *bed evaluation* model is provided as input.

It is worth noting that the use of dynamic roughness in Delft3D FM requires additional model settings beyond the standard physical parameter settings (Deltares 2024). In this study, according to the user's manual, spatially varying bed roughness influenced by dynamic roughness was introduced using the IniField mechanism. All simulations were performed in depth-averaged mode (the value of Kmx is selected 0 in model definition file (MDU), hereafter, the parameters setting in MDU are referred to as Kmx=0), and the built-in trachytope-based roughness formulation for alluvial and vegetation effects was disabled (TrtRou = N) to avoid the use of the internal vegetation roughness model. Therefore, the Manning formulation (*n*, UnifFrictType = 1) was used to represent bed roughness in the model calculations. Instead of modeling with a uniform *n*, spatial variability in roughness was explicitly imposed through an external parameter field specified via the IniFieldFile keyword in the MDU. The IniField configuration defined roughness as the “frictioncoefficient” quantity and linked it to an XYZ sample file containing spatially distributed *n* values (Figure 4-12). These roughness values were interpolated onto the 2D computational grid using triangulation, following the standard implementation in Delft3D FM. During model initialization, the dynamic roughness map was read, processed, and applied to the flow grid, and the default uniform roughness setting was overridden. The effective use of dynamic roughness in the hydrodynamic simulations was verified through multiple methods. Firstly, diagnostic model logs confirmed that the IniField configuration file and the associated roughness sample data were successfully read and used during model initialization. Secondly, the output spatial distributions of roughness from simulations with and without the use of the IniFieldFile differed markedly, demonstrating that the externally different roughness map was actively applied to the computational grid. Finally, additional comparisons of simulated water levels at additional observation points within the river reach, which were only used for testing the use of the roughness map, revealed differences between dynamic and fixed roughness *n*, further confirming that the dynamic roughness participated in the hydrodynamic calculations. The upstream daily discharge and downstream daily water level are specified as the upstream and downstream boundary conditions, respectively. This was done to simulate both subcritical and supercritical flow regimes, as a mixed behaviour was observed in the study reaches (Nones *et al.* 2020, Hamidifar *et al.* 2026). To analyse the performance of the model, the modelled output discharge at the observation cross-section is set as daily discharge, allowing its comparison with the observed discharge. Given the flood wave celerity of the analysed reaches, the output discharge at the observation cross-section is modelled at a sub-daily (6h) time scale, and then averaged to allow its comparison with the observed discharge, which is provided only at the daily scale (Nones, 2019).

3.7.4 Performance evaluation metrics

The coefficient of determination (r_P^2), calculated as the square of the Pearson correlation coefficient (equation 3-14), Percent Bias (*PBIAS*, equation (3-15)), and Nash–Sutcliffe Efficiency (*NSE*, equation (3-16)) are used to evaluate the performance of model simulations, as those statistics are among the most commonly adopted criteria for hydrodynamic model evaluation (Boyle *et al.* 2000, Moriasi *et al.* 2007).

$$r_P^2 = \frac{\sum_{i=1}^{N}(Q_i-\bar{Q})(S_i-\bar{S})}{\sqrt{\sum_{i=1}^{N}(Q_i-\bar{Q})^2}\sqrt{\sum_{i=1}^{N}(S_i-\bar{S})^2}} \tag{3-14}$$

$$PBIAS = 100 * \frac{\sum_{i=1}^{N}(S_i-Q_i)}{\sum_{i=1}^{N}Q_i} \tag{3-15}$$

$$NSE = 1 - \frac{\sum_{i=1}^{N}(S_i-Q_i)^2}{\sum_{i=1}^{N}(Q_i-\bar{Q})^2} \tag{3-16}$$

where Q_i and S_i denotes the observed and estimated value of the i-th sample, respectively, $\bar{Q}$ and $\bar{S}$ represent the corresponding model prediction, and N is the number of samples.

Different from the R^2 defined as equation (3-6), here r_P^2 quantifies the degree of linear association between simulated and observed values and is used to assess the consistency of temporal variations and overall trends (Legates and McCabe 1999). r_P^2 mainly reflects how well the model captures the timing and relative fluctuations of the target variable rather than the absolute magnitude of errors: a high r_P^2 indicates that the simulated results follow the observed temporal dynamics well, even if systematic bias exists (Guo *et al.* 2022). Therefore, r_P^2 is particularly useful for assessing whether the governing processes and boundary conditions enable the model to reproduce the dominant variability patterns of the system. However, due to the insensitivity of r_P^2 to systematic overestimation or underestimation, and error magnitude (Onyutha 2020), it should be interpreted together with complementary metrics that quantify bias (*PBIAS*) and accuracy (*NSE*).

PBIAS is a dimensionless statistical indicator that quantifies the average tendency of simulated values to be systematically higher or lower than the corresponding observations (Gupta *et al.* 1999). A positive *PBIAS* indicates overall model overestimation, while a negative *PBIAS* indicates underestimation, making it particularly useful for diagnosing directional model bias rather than random error magnitude (Akkala *et al.* 2025). Because *PBIAS* is based on the sum of residuals, it is insensitive to error variance and extreme values (Moriasi *et al.* 2007). In hydrodynamic modeling, *PBIAS* is widely used to identify systematic deficiencies related to the used parameterization, such as channel roughness, resistance formulations, or boundary condition specification (Moriasi *et al.* 2007, Zhang 2018). In combination with efficiency and error metrics, *PBIAS* provides a more interpretable and physically meaningful assessment of model performance.

The *NSE* is also a widely used index that evaluates the predictive ability of a model by comparing the residual variance of simulations with the variance of observations relative to their mean (McCuen *et al.* 2006). *NSE* assesses how well a model performs relative to a simple baseline prediction using the observed mean, therefore providing an integrated measure of model efficiency (Schaefli and Gupta 2007, Duc and Sawada 2023). *NSE* values approaching unity indicate excellent performance between simulated and observed values, while values close to or below zero suggest that the model performs no better than, or even worse than, the baseline prediction (Schaefli and Gupta 2007). In hydrodynamic modeling, *NSE* is particularly valuable since it simultaneously accounts for error magnitude, variability, and extreme values, making it a robust criterion for overall model performance (Moriasi *et al.* 2007).

In conclusion, the combination of r_P^2, *PBIAS*, and *NSE* provides a comprehensive assessment of model performance. The r_P^2 metric describes the consistency of temporal variations between simulated and observed values, *PBIAS* quantifies the direction and magnitude of systematic bias, and *NSE* evaluates the overall predictive skill of the model relative to a baseline prediction using the observed mean. These three complementary metrics capture trend consistency, systematic deviation, and overall efficiency, allowing the model performance to be fully characterized without redundancy.

3.7.5 Model output, calibration, and evaluation

The modeling results can be viewed and exported by inputting the .his and .map files generated by the Delft3D FM model into the Quick Plot software supported by Delft University (Figure 3-15).

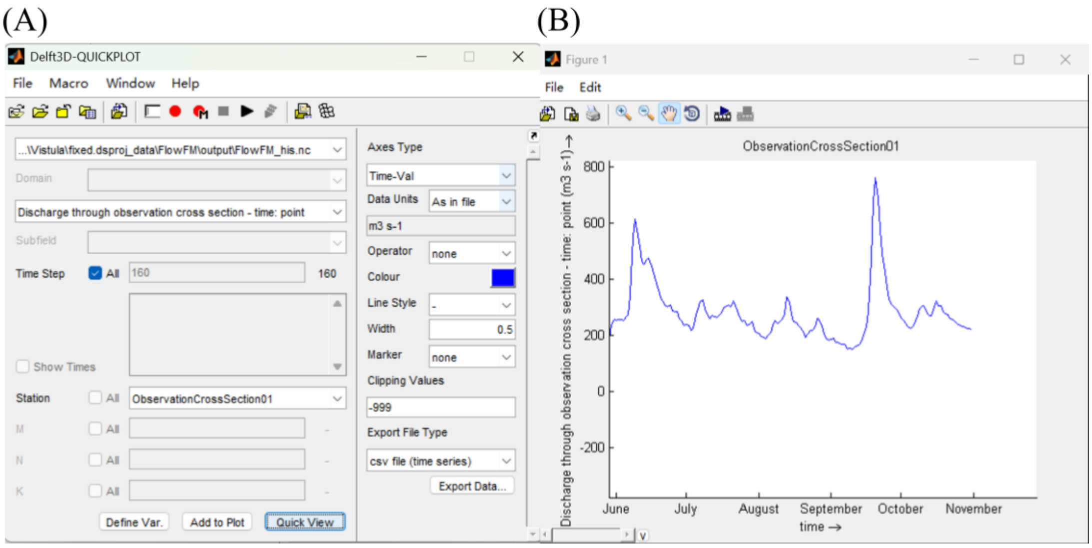

Figure 3-15. An example of Delft3D QuickPlot. (A) User interface of Delft3D QuickPlot, (B) Quick view discharge plot by Delft3D QuickPlot

Model calibration and validation are fundamental procedures in hydrodynamic modeling to ensure reliable model performance for a given application, as calibration allows uncertain model parameters to be adjusted to better reproduce observations (Gupta *et al.* 1999b, Refsgaard and Henriksen 2004, Moriasi *et al.* 2007, Beven 2012), while validation verifies that those parameters are actually able to reproduce the observations.

The main aim of the calibration period is to adjust uncertain model parameters within physically reasonable ranges to achieve optimal agreement between simulated and observed values (Gupta *et al.* 1999b, Refsgaard and Henriksen 2004), ultimately reducing systematic errors associated with parameter uncertainty while preserving the physical consistency of the model structure (Vrugt *et al.* 2003, Beven 2012).

The validation period is subsequently used to evaluate the predictive capability of the calibrated model using an independent dataset that was not involved in the calibration process (Refsgaard and Henriksen 2004, Moriasi *et al.* 2007). By assessing model performance under different conditions, the validation step helps to identify potential overfitting and to verify whether the calibrated parameters remain transferable beyond the calibration period (KlemeŠ 1986).

In this study, fixed and satellite-based roughness values were both used to drive the model for the period from 1 May to 31 October 2024. This period was chosen because the UAV data were collected during the same season in 2025, assuming that vegetation types are similar within the same river section during the same season, while the 2025 hydrological data verified by the local water authorities, are not yet available. The model was calibrated and validated based on the daily discharges measured and computed at the two downstream gauging stations (Figure 3-12).

For the fixed-roughness-driven model, a model warm-up period of one month was performed from 1 May to 31 May 2024, and the uniform bed roughness value (Manning's n) was used as a calibration parameter over the period from 1 June to 31 August 2024. The model was subsequently run for validation during the period from 1 September to 31 October 2024. It is worth noting that, due to limitations in hydrological data availability, the modeling period was set from June to October 2024, while the field measurements were conducted in 2025. This temporal mismatch is acceptable, as supported by the similar average MVIs values and maps derived from satellite imagery (Table D2-1 and Figure D2-1 to D2-5). Take average NDVI value as an example, the NDVI values are 0.26 in 2024 and 0.30 in 2025 for the Vistula River, and 0.11 in 2024 and 0.18 in 2025 for the Po River, indicating comparable vegetation conditions between the two periods. The average NDVI maps of Vistula and Po Reaches from 1 June to 31 October 2024 and 2025 are shown in Figure 3-16. The spatial distributions of average NDVI in the Vistula and Po Reaches were similar in 2024 and 2025, which is consistent with the similarity in the average NDVI values.

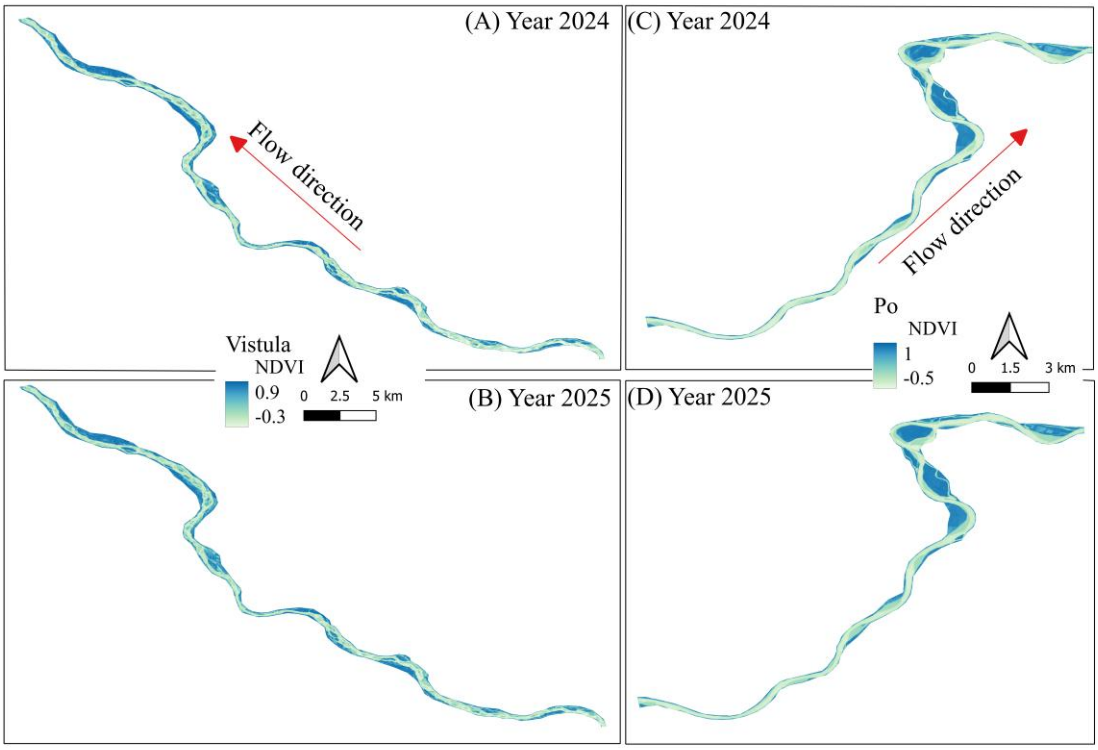

Figure 3-16. Average NDVI maps of the Vistula and Po Reaches from 1 June to 31 October in 2024 and 2025. (A) and (B) show the Vistula Reach in 2024 and 2025, respectively. (C) and (D) show the Po Reach in 2024 and 2025.

Given that the study aimed at comparing satellite-based and fixed roughness models, the best fixed roughness value (Manning's *n*, derived from the previous calibration+validation model) was adopted in the satellite-based roughness-driven model. With a one-month warm-up period from 1 May to 31 May 2024, the satellite-based-roughness-driven model was therefore run for the whole period (1 June - 31 October 2024), without distinguishing between calibration and validation.

Chapter 4 Results

Following the methodology described in the previous chapters, this chapter presents the results from vegetation observations from UAV survey and satellite imagery, machine learning–based vegetation height estimation, and hydrodynamic simulations of discharge by the Delft3D FM model. The discussion focuses on how uncertainties and patterns propagate across these stages and influence flood modelling performance.

4.1 Vegetation conditions on sandbars based on UAV surveys

The two-dimensional (2D) models of the five sandbars derived from UAV measurements are shown in Figure 4-1. The areas of the five sandbars are around 0.5 km^2 (ROI 1 in Vistula), 1.2 km^2 (ROI 2 in Vistula), 0.2 km^2 (ROI 1 in Po), 1.1 km^2 (ROI 2 in Po), and 0.45 km^2 (ROI 3 in Po), respectively (Table 4-1).

Table 4-1. Overall information of five ROIs, noting that the vegetation type coverages are classified by human eyes.

	ROI Area (km^2)	**Reach area(km^2)**	**Percentage of reach area (%)**		**Grass coverage**	**Trees coverage**	**Bare land coverage**
Vistula Reach							
ROI 1	0.5	54.58	0.92	Area (km^2)	0.24	0.10	0.16
				Percentage of sandbar area (%)	48	20	32
ROI 2	1.2		2.20	Area (km^2)	0.99	0.11	0.01
				Percentage of sandbar area (%)	82.50	9.17	8.33
Po Reach							
RO1 1	0.2	16.95	1.18	Area (km^2)	0.16	0.03	0.01
				Percentage of sandbar area (%)	80	15	5
ROI 2	1.1		6.49	Area (km^2)	0.84	0.17	0.09
				Percentage of sandbar area (%)	76.36	15.45	8.19
ROI 3	0.45		2.65	Area (km^2)	Almost cannot be classified by eye.		
				Percentage of sandbar area (%)			

4.1.1 Vistula Reach

According to Figure 4-1 and Table 4-1, ROI 1 in Vistula is covered by grassland for 48%. On the northern side of the sandbar, there are two unvegetated bare lands, while low woody vegetation (i.e., shrubs) is distributed along the boundaries of the sandbar and around the edges of the bare lands. For ROI 2 in the Vistula Reach, unvegetated bare areas were present within the sandbar but accounted for only 8.33% of the area. Grassland clearly dominated the vegetation cover (82.5%), while tree cover (9.17%) was substantially lower than in ROI 1 (20%). Grassland is mainly concentrated in the central–northern section of the sandbar, while the remaining areas are predominantly covered by low woody vegetation.

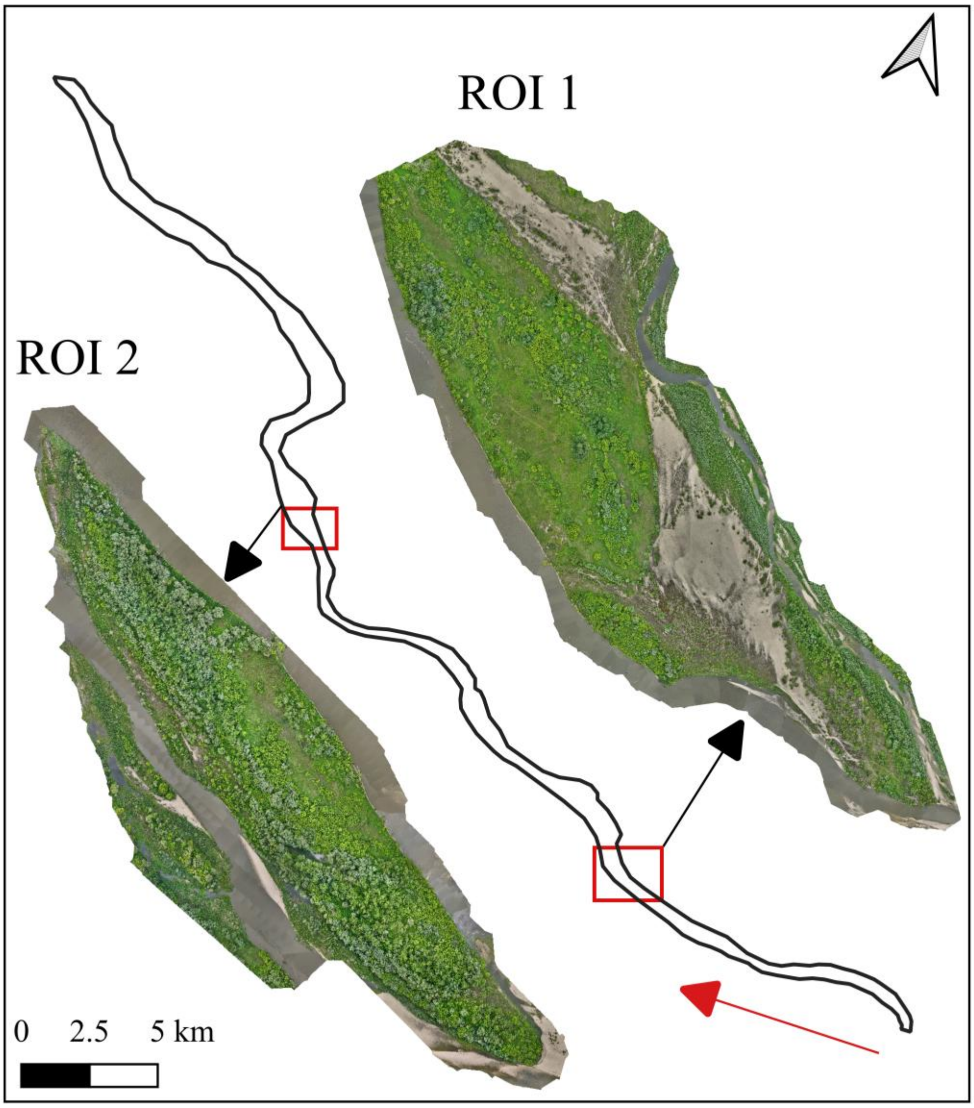

Figure 4-1 UAV survey RGB imagery of two ROIs in the Vistula Reach. The red arrow indicates the flow direction. The darker the vegetation, the higher and denser it is. Shrubs and trees show a rough texture, while grass appears smoother and light green.

4.1.2 Po Reach

Compared with the vegetation distribution in the Vistula ROIs, the Po ROIs (Figure 4-2, Table 4-1) have a significantly higher proportion of tree cover. In the Po reach, ROI 1 is dominated by tall woody vegetation, with grassland distributed in patchy patterns between woody patches and accompanied by small area bare surfaces. While ROI 2 is primarily grass-dominated, with grassland mainly concentrated in the southeastern part of the sandbar, tall wood vegetation is mainly located in the northwestern part. The area of grassland and tall trees is 0.84 km^2 and 0.17 km^2, respectively, and accounts for 76.36% and 15.45% of the total area, respectively. Scattered low woody vegetation is also observed within the grass-dominated areas. Sandy bare surfaces occur along the sandbar beside the main channel, with an area of 0.09 km^2. Unlike the bare areas observed on the Vistula, these sandy surfaces exhibit sparse and discontinuous vegetation patches. The Po ROI 3 has a smaller area than the other two sandbars and is mainly covered by tall woody vegetation. Grassland occurs in the gaps between woody vegetation, with two distinct grass-dominated areas located in the central–eastern part of the sandbar. There is no obvious bare surface observed in ROI 3.

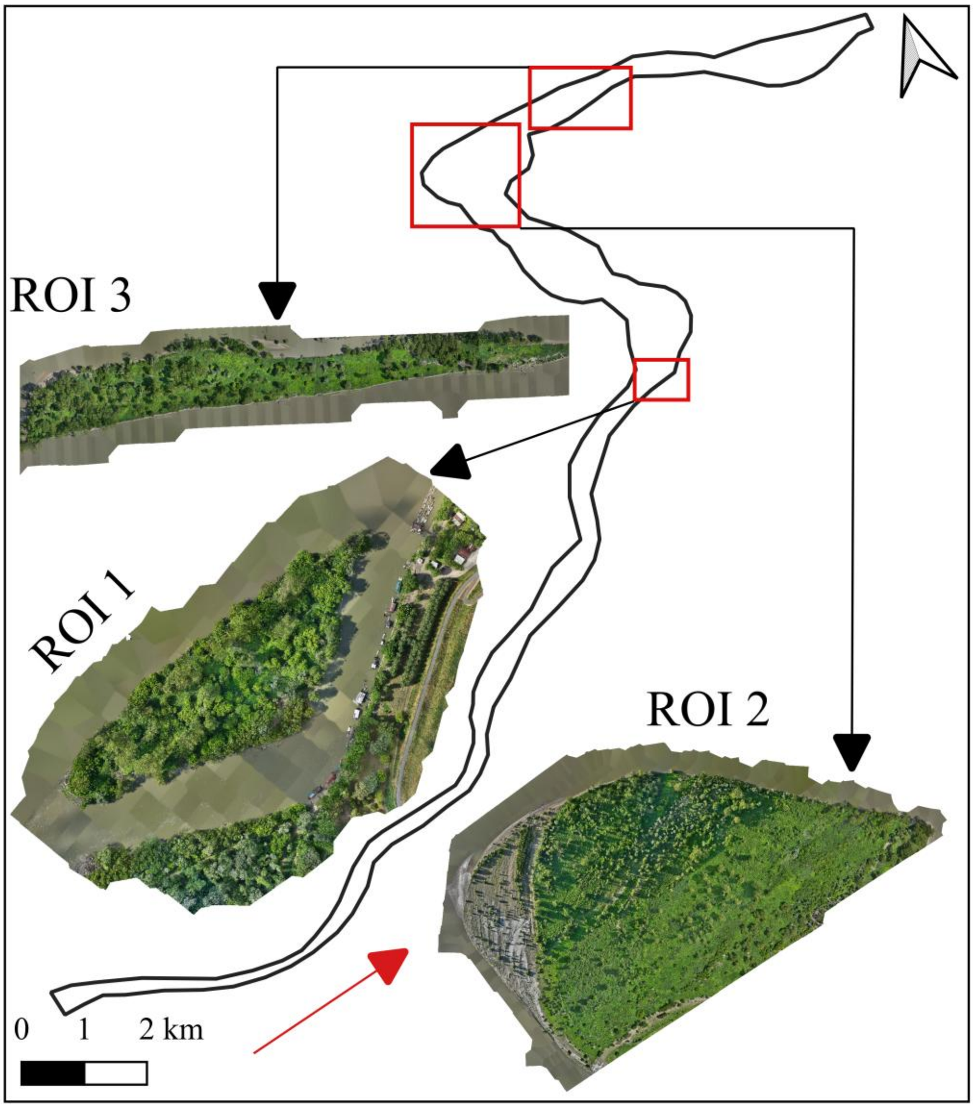

Figure 4-2 UAV survey RGB imagery of three ROIs in the Po Reach. The red arrow indicates the flow direction. The darker the vegetation, the higher and denser it is. Shrubs and trees show a rough texture, while grass appears smoother and light green.

4.2 Machine learning–based vegetation height estimation

The evaluation results of the machine learning (ML) models trained on data from the Vistula reach, the Po reach, and the combined Vistula+Po dataset are presented in this section. The evaluation metrics (R^2, *PBIAS*, and *RMSE*) for the three training regions are summarized in Tables 4-2 for comparison. More detailed results are discussed in the following sections.

Table 4-2. Comparison of three metrics of the ML models trained in Vistula Reach, Po Reach, and Vistula+Po Reaches

	Vistula		**Po**		**Vistula+Po**	
	0-3 m	3-20 m	0-3 m	3-20 m	0-3 m	3-20 m
R^2	0.74	0.61	0.74	0.63	0.72	0.57
PBIAS **(%)**	6.74	3.75	7.40	3.79	8.03	4.40
RMSE **(m)**	0.29	2.18	0.30	2.11	0.33	2.30

4.2.1 Vistula Reach

The results of machine learning (ML) in Vistula Reach are shown in Table 4-2.

Figure 4-3 (A) shows that simulated values show good agreement with observations in the 0-3 m vegetation height, with most points distributed close to the 1:1 reference line. The R^2, *PBIAS*, and *RMSE* between the observed and simulated *h* are 0.74, 6.74%, and 0.29 m (Table 4-2). The R^2 value indicates that approximately 74% of the variance in the observed vegetation height is explained by the model, suggesting that the overall spatial and magnitude-related variability of *h* is well captured. The *PBIAS* value of 6.74% shows a small overall bias, indicating a slight overall overestimation of vegetation height. The *RMSE* of 0.29 m is low relative to the 0–3 m height range considered, implying that the typical absolute deviation between simulated and observed *h* is below 10% of the maximum vegetation height. The combination of these three metrics proves that the model provides a reliable representation of low vegetation height, with good explanatory power, limited overall bias, and small absolute errors.

When vegetation height is between approximately 0.5 and 2 m, the scatter is relatively compact, indicating a stable correspondence between simulated and observed heights. At the same time, clear horizontal banding can be observed, particularly in the 1 to 2 m range, where simulated heights concentrate at a small number of fixed values, resulting in such horizontal bands. Moreover, very few points appear in the lower-right part of the scatter plot, meaning that cases with low observed height and high simulated height are relatively rare.

In the 3 to 20 m range (Figure 4-3 (B)), dispersion increases noticeably, with R^2 decreasing to 0.61 and *RMSE* increasing to 2.18 m (Table 4-2). Despite increased scatter, the point cloud still follows the general direction of the 1:1 line, indicating that the overall variation in taller vegetation is captured. Banding structures become more pronounced, especially between 6 and 12 m, and a similar empty region appears in the lower-right corner, where few samples combine high observed height with low simulated height.

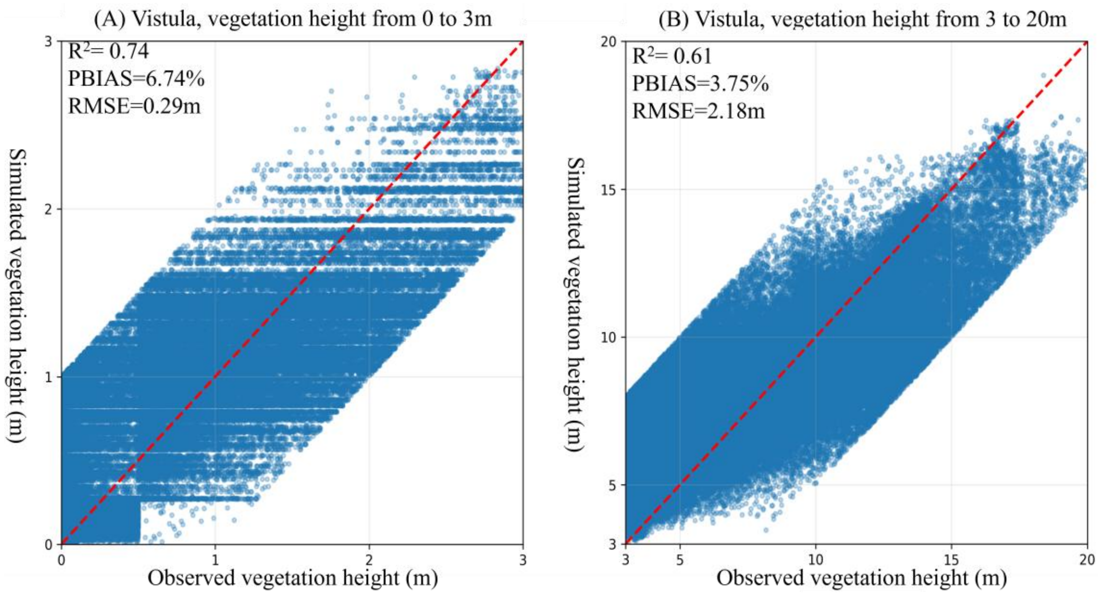

Figure 4-3. Comparison of the vegetation height predicted by the trained ML model (y-axis) and UAV-observed vegetation height (x-axis) in the Vistula Reach. Notably, the red dashed line is the $y = x$ line.

4.2.2 Po Reach

For the Po reach, model performance in the 0 to 3 m range is comparable to that of the Vistula reach (Table 4-2), and the results are summarized in Figure 4-4(A). The R^2 value of 0.74 indicates that the model explains approximately 74% of the observed variability in vegetation height and well captures the main spatial patterns and height variations. An *RMSE* of 0.30 m is small relative to the 0 to 3 m target range, showing that the typical difference between simulated and observed heights is around 0.3 m (10% of the maximum *h*). The positive *PBIAS* reflects a slight overall overestimation of vegetation height. Moreover, most points lie close to the 1:1 line, particularly between 0.5 and 2 m, indicating a consistent relationship between simulated and observed heights. Distinct horizontal bands appear again, with simulated values concentrated at several fixed levels. As in the Vistula reach, the lower-right part of the scatter plot contains very few points, showing that strong overestimation at low observed heights is uncommon. In summary, one can conclude that, in Po Reach, the model provides a reliable representation of low vegetation height, with good overall performance and only modest systematic bias.

When it comes to the 3–20 m range (Figure 4-4(B)), the Po reach shows slightly better performance, with values of R^2 and *RMSE* of 0.63 and 2.11 m, respectively. The scatter distribution is more continuous, although pronounced banding remains evident, particularly between 8 and 15 m. A rectangular empty region is still present in the lower-right corner, indicating limited sample coverage for combinations of high observed height and low simulated height.

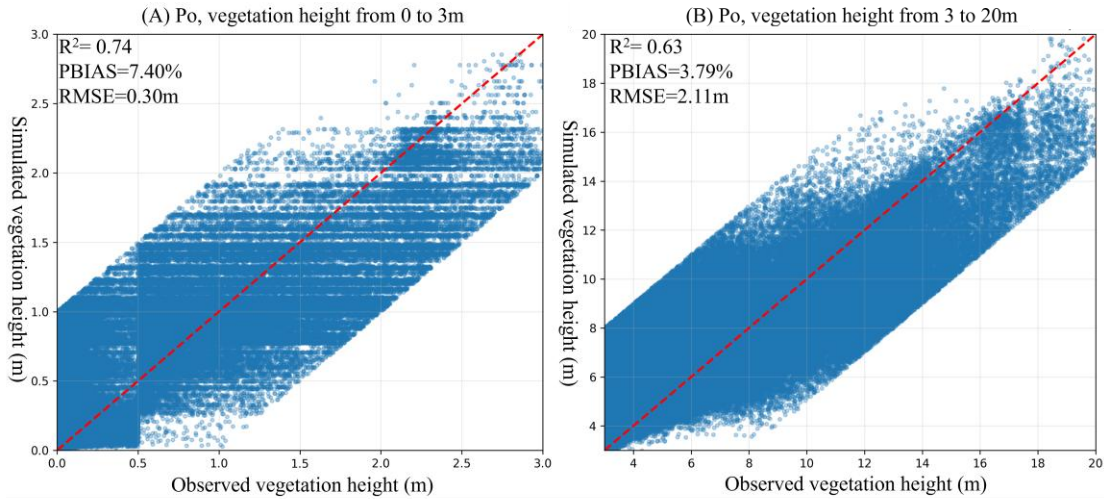

Figure 4-4. Comparison of the vegetation height predicted by the trained ML model (y-axis) and UAV-observed vegetation height (x-axis) in Po Reach. Notably, the red dashed line is the $y = x$ line.

4.2.3 Vistula and Po Reach

When combining the data in the Po and Vistula to train the model, the results are displayed in Figure 4-5.

The model performance in the 0 to 3 m range (Figure 4-5(A)) decreases slightly, with values of R^2 and $RMSE$ of 0.72 and 0.33, respectively, and a similar overall distribution pattern to that of the individual reaches.

Points from both river reaches overlap along the 1:1 line, and horizontal banding becomes denser due to the superposition of samples. The lower-right empty region remains visible, confirming that this feature is not reach-specific.

In the 3 to 20 m range (Figure 4-5(B)), the R^2 and $RMSE$ are 0.57 and 2.03m, respectively, and scatter increases further. Points form a broad band around the 1:1 line at intermediate and higher vegetation heights, with persistent banding and a clear empty region in the lower-right corner. Despite the increased dispersion, the model still reproduces the overall trend of vegetation height variation across the combined dataset.

Overall, the ML model exhibits consistent behavior across the three datasets (Vistula, Po, and the Vistula+Po). In the 0–3 m vegetation height range, the model reproduces the observed height variations reasonably well for all regions, with relatively small errors and good agreement with observations, indicating a stable performance for low vegetation. In contrast, model performance decreases in the 3–20 m range for all regions, where scatter increases, and banding patterns become more pronounced, suggesting a reduced ability to represent medium to tall vegetation.

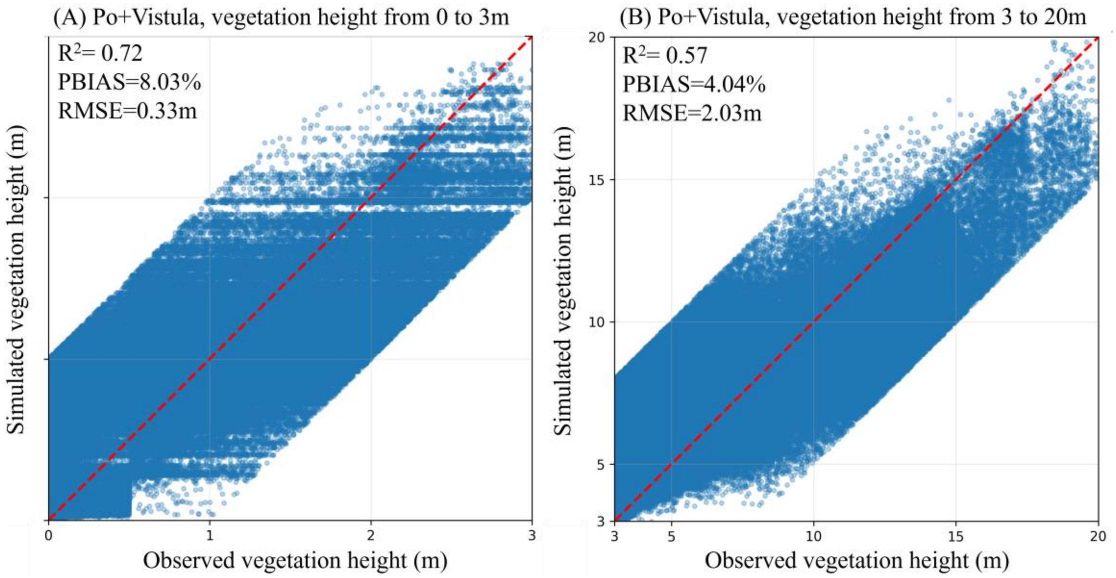

Figure 4-5. Comparison of the vegetation height predicted by the trained ML model (y-axis) and UAV-observed vegetation height (x-axis) in the Vistula and Po reaches together. Notably, the red dashed line is the $y = x$ line.

4.3 UAV vs satellite-derived vegetation height

4.3.1 Vistula Reach

The relationship between satellite-based estimated vegetation height (*h*) and drone-measured *h* for the Vistula Reach is illustrated in Figure 4-6.

In general, the distribution of scatter shows a clear positive relationship, with the majority of points distributed along the 1:1 reference line. The high R^2 with the value of 0.88 indicates a large proportion (88%) of the variance in drone-measured *h* can be explained by satellite-based estimates. The *RMSE* between satellite-based *h* and UAV-measured *h* is 0.0.23, indicating that, on average, the deviation between satellite-based *h* and drone-measured *h* is approximately 0.23m. The negative *PBIAS* value, which is -5.26%, shows a slight overall underestimation of vegetation height by the model. In conclusion, the high R^2 demonstrates that the model effectively captures the spatial variability of *h*, while the low *RMSE* confirms its numerical accuracy. Meanwhile, the low value of *PBIAS* indicates that the systematic bias is small, demonstrating that the ML model for estimating *h* from satellite imagery is reliable.

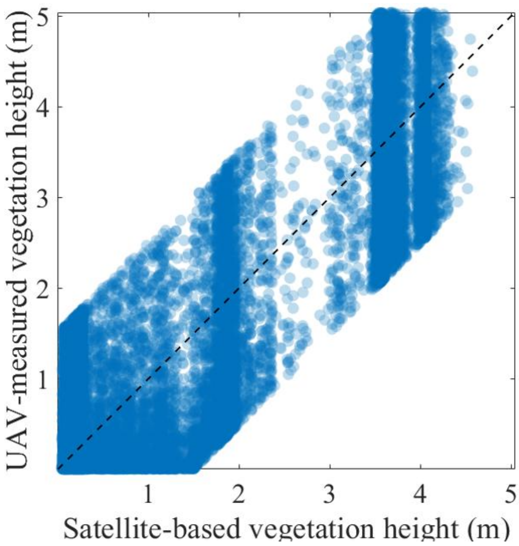

Figure 4-6. Comparison of vegetation heights derived from satellite and UAV measurements in the Vistula Reach on 29 May 2025. The black dashed line is the $y = x$ line.

It can be noticed that, at low *h* areas (below approximately 1.0 m), the point cloud is densely clustered and closely aligned with the 1:1 line, indicating a high level of consistency between satellite estimates and UAV observations for small vegetation. This result implies that the spectral features derived from multispectral imagery are particularly sensitive to low vegetation, allowing the model to achieve relatively accurate height retrievals in this range.

For intermediate vegetation heights (approximately 1.0 to 3.0 m), the scatter gradually increases, although the majority of points remain centered around the 1:1 line. This indicates that the model still preserves a reasonable predictive capability across this height range, even if it is visible that uncertainty increases with vegetation height.

At higher vegetation heights (>3.0 m), a noticeable increase in dispersion is observed. In this height range, both underestimation and overestimation occur, although a slight tendency to underestimation can be identified, where satellite-based estimates are generally lower than the corresponding UAV-measured *h*.

4.3.2 Po Reach

Figure 4-7 presents the comparison between satellite-based *h* and UAV-measured *h* for the Po Reach. Similar to the Vistula case study, a positive relationship between estimated and observed *h* is positive. Quantitatively, the model has an R^2 of 0.89, an *RMSE* of 0.15 m, and a *PBIAS* of −1.32%, indicating a slightly higher overall accuracy and lower systematic bias compared to the Vistula Reach. Namely, the model effectively captures the dominant spatial variability of vegetation height while maintaining a high level of accuracy and exhibiting only a marginal tendency towards underestimation at the reach scale.

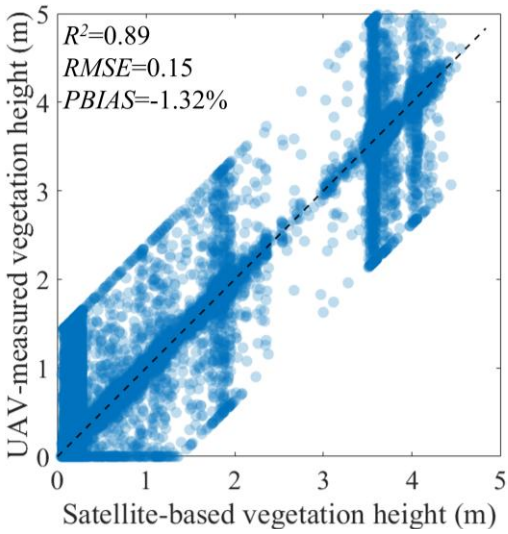

Figure 4-7. Comparison of vegetation heights derived from satellite and UAV measurements in Po Reach on 27 May 2025. The black dashed line is the $y = x$ line.

At vegetation heights below approximately 1.5 m, where Po Reach is covered by short vegetation, the point cloud exhibits substantial dispersion, with a large proportion of points located below the 1:1 line, suggesting that, compared to UAV-derived vegetation height, satellite-based estimates tend to estimate lower values for short vegetation. Although the overall *RMSE* is low, larger errors are mainly observed for very short vegetation (<1.5 m), since the multispectral information of low *h* vegetation is difficult to distinguish from that of the bare land from satellite imagery.

For intermediate to high vegetation heights, which are approximately 2.0 to 5.0 m, the scatter gradually becomes more aligned with the 1:1 line. Similarly to the short vegetation range, larger errors are observed for *h* higher than 5 m, where increased canopy structural complexity and height variability within individual grids weaken the sensitivity of multispectral features to vegetation height. In addition, canopy shadowing can cause vegetation with different heights to exhibit similar multispectral signals, further reducing height discrimination and contributing to increased prediction errors. It is worth noticing that vegetation in the Po Reach is generally higher than in the Vistula Reach, which reflects the more complex spatial distribution and vegetation structure in this river.

4.4 Hydrodynamic simulations

The hydrodynamic modeling results are explained in detail in this section. It is worth noting that, in both case studies, the period from 01 May to 31 May 2024 was set as the warm-up period, from 01 June to 31 August 2024 as the calibration period, and from 01 September to 31 October 2024 as the validation period.

4.4.1 Model calibration in the Vistula Reach

The hydrodynamics model was calibrated by varying Manning's roughness *n*, considering three different metrics to evaluate the model performance (Figure 4-8).

As the *n* increases from 0.02 to 0.09, both the r_P^2 and the *NSE* first increase and then decrease slightly. The r_P^2 rises from about 0.92 at lower *n* values to its highest values at *n* values around 0.05, while *NSE* shows a similar increasing trend and reaches its maximum at *n* values around 0.05, indicating that the simulated discharge follows the observed discharge more closely as roughness increases from low values. When *n* further increases to more than 0.05, both r_P^2 and *NSE* show a decreasing trend, suggesting that too high roughness values reduce the model performance.

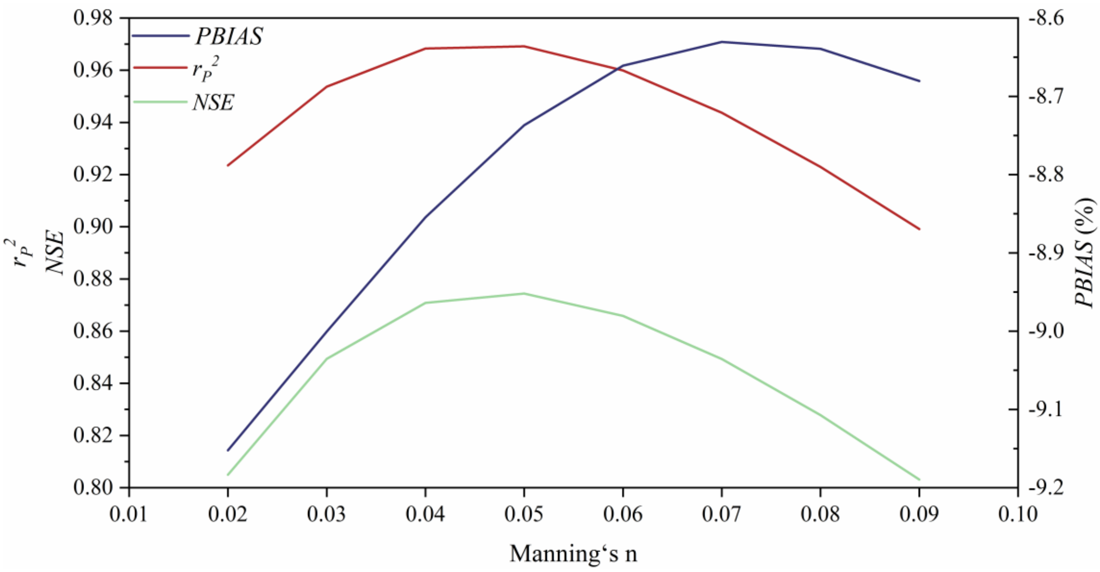

Figure 4-8. Variations in model performance metrics (r_P^2, *PBIAS*, and *NSE*) as a function of Manning's roughness coefficient *n* in the Vistula Reach.

At the same time, the *PBIAS* decreases with increasing roughness and reaches its minimum at *n* is 0.06, after which it remains nearly constant. Although *PBIAS* has a smaller variation than r_P^2 and *NSE*, its minimum value occurs at nearly the same *n* where r_P^2 and *NSE* show their best performance, indicating that all three metrics show a similar optimal roughness range.

When considering r_P^2, *PBIAS*, and *NSE* together, as we can notice from Figure 4-8, a single intersection point can be identified around the *n* value with 0.06, representing a transition between improving and deteriorating model performance. The roughness value at this intersection provides a balanced representation of model performance across the different metrics. Therefore, an *n* value of 0.06 is selected as the calibrated roughness value, as its r_P^2 and *NSE* are the biggest, while having the lowest *PBIAS* among the calibrated roughness values. Previous studies shown a similar *n* value (Hamidifar *et al.* 2026, Osuch 2015).

Over the period from 1 June to 31 August 2024, the observed discharge presented a clear transition from an initial high discharge regime to progressively lower discharge conditions, with several flood events of decreasing magnitude (Figure 4-9).

At the beginning of the period (1–6 June), discharge remained relatively stable, with values around 300–350 m³/s. Discharge then rose rapidly between 7 and 8 June, increasing sharply from 346 m³/s to a peak of 689 m³/s, followed by a slightly lower peak of 682 m³/s on June 9. This event represents the largest flood during the simulation period.

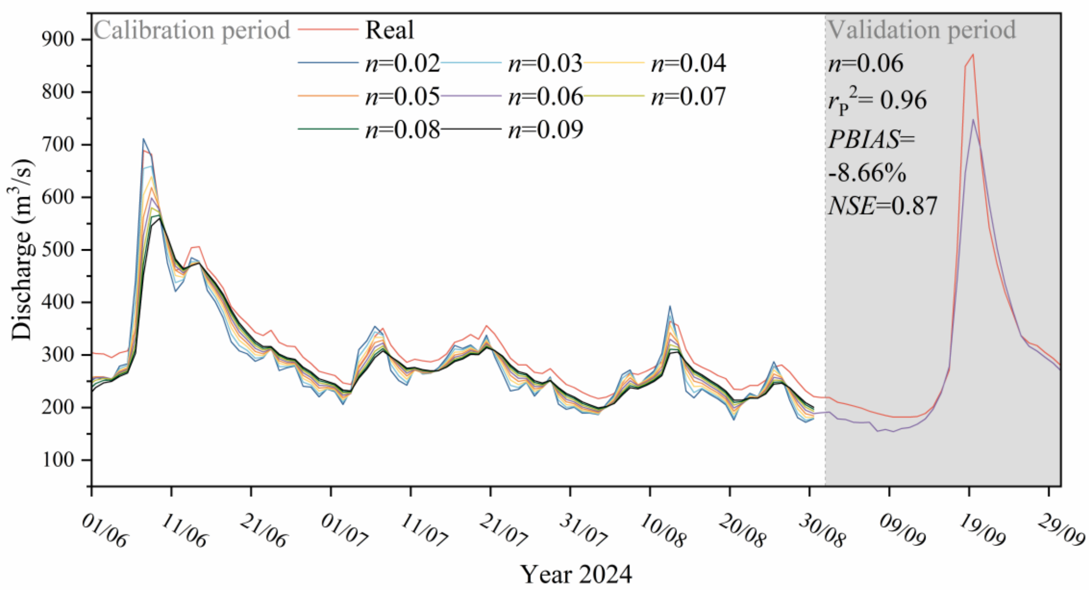

Figure 4-9. Simulated discharges obtained using different *n* values during the calibration period in Vistula Reach, together with a comparison between the observed discharge and the discharge simulated using the optimal roughness coefficient (*n* = 0.06) as validation. Note that the validation period is marked as grey, and the x-axis reports the time as day/month of 2024.

After the flood peak in early June, discharge decreased but remained elevated during 10 to 15 June, with values generally exceeding 460 m³/s, indicating a period of sustained high discharge following the main flood event. From mid to late June, discharge showed a gradual reduction, with several moderate secondary peaks observed, notably 392 m³/s on 19 June and 347 m³/s on 24 June.

In early July, discharge continued to decline and fell below 300 m³/s between 1 and 4 July. A secondary flood event occurred between 5 and 8 July, with discharge rising from 278 m³/s to 351 m³/s, after which discharge decreased and returned to lower levels. Another moderate peak was observed on 21 July, reaching 356 m^3/s, followed by relatively stable discharge conditions during the remainder of July, typically ranging between 260 and 300 m^3/s.

Discharge continued to decrease overall in August, with values of approximately 220–240 m^3/s during early August. A further secondary flood event occurred in mid-August, with discharge increasing from 287 m^3/s on 12 August to 364 m^3/s on 13 August, followed by a gradual decline. By late August, discharge reached the lowest levels of the period, dropping below 240 m^3/s during 29–31 August.

The discharges simulated by different n during the period are shown in Figure 4-9 as well. For the biggest flood peak on 8 to 9 June 2024, simulations with lower roughness values (n from 0.02 to 0.03) reproduced peak magnitudes that were close to or slightly higher than the observed values on 8 June, while simulations with intermediate roughness (n from 0.04 to 0.05) yielded calculated lower peak discharges than observed. When the n increased further (n higher than 0.06), the simulated peak discharge decreased progressively and became markedly lower than the observed peak, indicating increasing underestimation of the main flood magnitude.

A similar pattern was observed during the secondary peak on 10 June. Simulations with n lower than 0.03 slightly overestimated or closely matched the observed discharge, while simulations with n higher than 0.05 produced lower discharges, with underestimation becoming more pronounced for n higher than 0.07.

During the moderate flood events in mid to late June, such as those on 19 June and 24 June, differences among simulations were reduced compared to the main flood event. However, simulations with lower roughness values tended to produce higher discharges than observed, while simulations with higher roughness values remained consistently lower than the observations. The transition from relative overestimation to underestimation occurred between n from 0.04 to 0.06, depending on the specific event.

For the secondary flood event in early July, simulations with n from 0.02 to 0.03

generally overestimated discharge throughout the rising and peak periods. Simulations with *n* from 0.04 to 0.05 yielded peak discharges close to the observed value, while simulations with *n* higher than 0.06 increasingly underestimated the peak.

During the peaks on 21 July and 13 August, simulated discharges showed a comparable dependence on roughness. Lower roughness values resulted in higher simulated discharges, while higher roughness values led to reduced peak magnitudes, with systematic underestimation evident for *n* higher than 0.07.

In the low-flow periods, particularly from late July to late August, simulations with lower roughness values ($n < 0.03$) tended to remain closer to the observed discharge, while simulations with higher roughness values ($n > 0.07$) consistently produced lower discharges. Simulations with intermediate roughness values ($0.04 < n < 0.06$) fell between these two regimes and remained closer to the observed discharge throughout the low-flow phase.

During the validation period from September to October 2024, the model using an *n* value of 0.06 generally underestimated the flow discharge in the Vistula Reach. Under low discharge conditions, such as in early September and late October, observed discharge typically ranged between 180 and 260 m^3/s, while the simulated discharge was mostly lower, indicating a persistent underestimation during low-discharge periods. During the main flood event in mid-September, the flood peak occurred on the same day in both the simulated and observed discharge, with no clear delay or advance in peak timing. However, the magnitude of the flood peak was underestimated, as the simulated peak remained clearly lower than the observed discharge. After the flood peak and during the following smaller flow increases, the simulated discharge followed the overall rising and falling trend of the observations but remained generally lower throughout this period.

Overall, the model captured the shape and timing of discharge variations reasonably well, but, during the validation period, it tended to underestimate discharge under both low and high discharge conditions.

4.4.2 Model calibration in the Po Reach

For the Po Reach, model performance according to three metrics shows a systematic but contrasting response to increasing n (Figure 4-10). As n increases from 0.02 to 0.09, both the r_P^2 and NSE improve steadily, indicating improved correspondence between simulated and observed discharge. Specifically, r_P^2 increases from 0.89 to 0.97, and NSE rises from 0.81 to 0.87. However, the $PBIAS$ shows a decreasing trend with increasing n, varying only slightly from −15.86% to −16.04%. Although higher n improves the consistency between simulated and observed discharge, the model continues to underestimate discharge across the n range from 0.02 to 0.09.

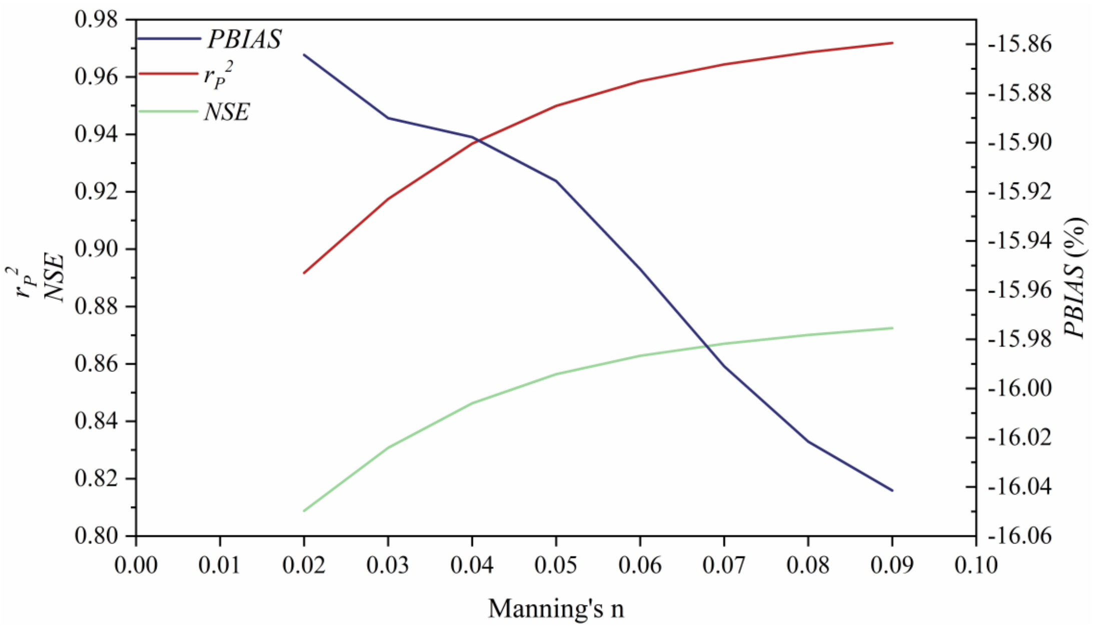

Figure 4-10. Variations in model performance metrics (r_P^2, *PBIAS*, and *NSE*) as a function of Manning's roughness coefficient n in the Po Reach.

To balance improvements in model fit (r_P^2 and NSE) against stability in bias ($PBIAS$), the intermediate n value between the two intersection points of the three curves is selected as the optimal calibrated parameter. Therefore, an n value of 0.06 is adopted for the Po Reach simulation, previous studies also had a similar n value (Nones 2019, Nones *et al.* 2020).

Noticing from Figure 4-11, during the calibration period from 1 June to 31 August 2024, the observed discharge in the Po River Reach presented large variability, with several clear flood events, after which the discharge gradually decreased to lower levels.

At the beginning of June, discharge was extremely high, reaching 3142 m^3/s on 1 June and further increasing to 3199 m^3/s on 2 June. From 3 to 7 June, discharge decreased rapidly, falling from around 2880 m^3/s to approximately 2170 m^3/s, indicating a strong recession following the early high discharge conditions.

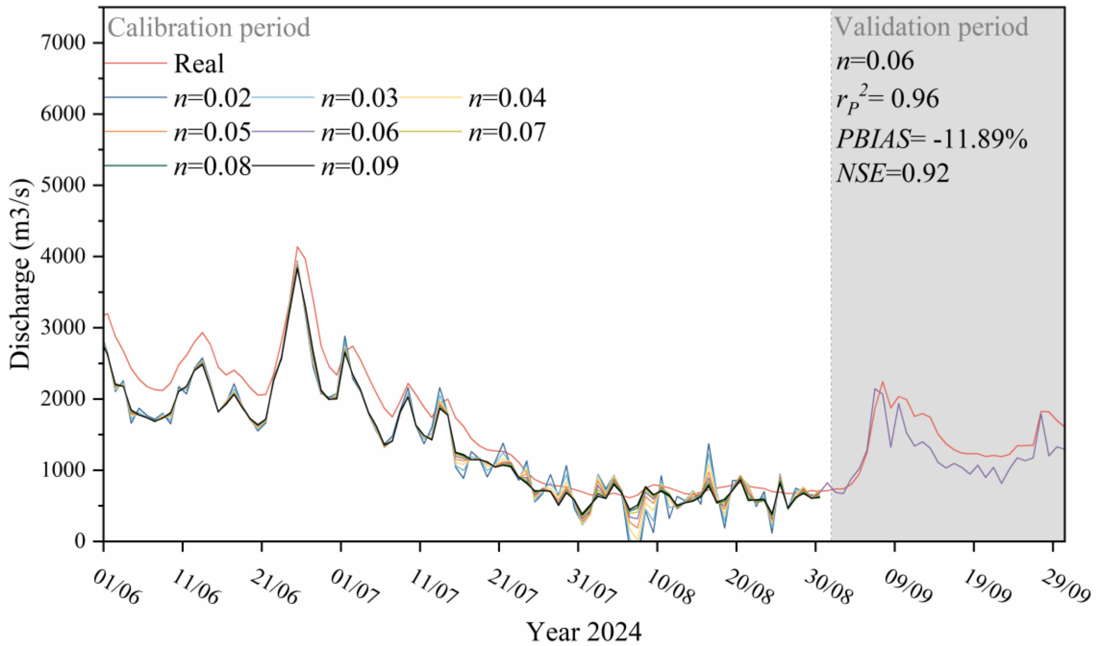

Figure 4-11. Simulated discharges obtained using different n values during the calibration period in Po Reach, together with a comparison between the observed discharge and the discharge simulated using the optimal roughness coefficient (n = 0.06) during validation. Note that the validation period is marked as grey, and the x-axis reports the time as day/month of 2024.

Between 8 and 14 June, discharge remained relatively high, generally ranging between 2100 and 2900 m^3/s, with moderate day-to-day fluctuations. A second major flood event developed in late June, with discharge increasing largely after 24 June and reaching a peak of 4139 m^3/s on 26 June, which was the largest flood during the study period. Following this peak, discharge declined but remained high on 27 June at nearly 4000 m^3/s, before decreasing steadily to the end of June.

In early July, observed discharge continued to decrease, falling to approximately 2300 m^3/s on 1 July and further declining to around 1750 m^3/s by 8 July. Several moderate discharge increases occurred during mid-July, but their magnitudes were much smaller than those observed in June.

From late July into August, discharge remained low and continued to decrease, dropping from around 1300 m^3/s to below 800 m^3/s by the end of August.

The discharge simulations using different n in the calibration period are displayed in Figure 4-11. The simulated discharge showed a strong sensitivity to the roughness during flood periods. For flood events with higher discharge, particularly the large flood around 26 June, simulations with lower n, roughly between 0.02 and 0.03, tended to simulate discharge values that were closer to the observed peak and, in some cases, slightly higher than the observations. As the n increased to the 0.04-0.05 range, the simulated peak discharge decreased and became lower than the observed peak. When the roughness increased further, above about 0.06, the simulated discharge was clearly lower than the observations, indicating a consistent underestimation of flood magnitude at higher roughness values.

The occurrence of flood peaks was generally reproduced on the same days as the observed discharge across all tested roughness values. There is no obvious systematic advance or delay of the flood wave peak as n increased. However, increased roughness enhanced flow resistance, which attenuated the flood wave and reduced the sharpness of the peak compared to lower roughness simulations.

A similar roughness-related response was also evident during secondary flood events in early and mid-July. Simulations with lower n produced higher discharge during both the rising stage and the peak, while simulations with n above approximately 0.06 consistently resulted in lower discharge throughout these events. The difference in roughness change occurred during periods of rapidly increasing discharge.

During low discharge conditions, particularly from late July through August, the influence of roughness on simulated discharge became smaller. Simulations with lower n, below approximately 0.03, tended to slightly overestimate discharge, while simulations with higher roughness values, above approximately 0.06, generally underestimated discharge. Simulations using intermediate roughness values, from 0.04 to 0.05, produced results between the high- and low-roughness cases and matched the observed discharge better during low-flow periods.

Overall, increasing the roughness n consistently reduced simulated discharge across both high and low discharge conditions, with the strongest effects observed during flood events.

The differences between the observed discharge and the simulated discharge using $n = 0.06$ during the validation period, which is from 1 September to 31 October, were also displayed in Figure 4-11.

At the beginning of September 2024, when observed discharge remained relatively low, the simulated discharge was generally higher than the observations, indicating an overestimation under low discharge conditions. This overestimation was most evident from 1 to 5 September, when the simulated values were consistently higher than the observed ones.

During the first flood event in early September, the model reproduced the rapid rise in discharge, but the simulated peak on 7 September was higher than observed, while the peak on 8 September was slightly underestimated. Overall, the timing of the peak was captured, but the magnitude differed between the simulated and observed discharges.

From mid to late September, the simulated discharge using n = 0.06 was consistently lower than the observed discharge, indicating systematic underestimation during moderate discharge conditions.

During the major flood events in October, the model simulated the timing of the main flood peaks rather well, with simulated and observed peaks occurring on the same days. However, the peak magnitudes were underestimated, particularly during the largest flood around 21 October, when the simulated discharge remained noticeably lower than the observed maximum discharge.

After the flood peak, during the decline period to late October, the simulated discharge followed the overall decreasing trend of the observations, but stayed consistently lower, showing that the model continued to underestimate discharge during the decreasing stage.

Overall, during the validation period (01 September to 31 October 2024), the model with n = 0.06 showed a tendency to overestimate discharge at low levels and underestimate discharge during moderate to high flood conditions, while the timing of major discharge variations was generally well simulated.

4.4.3 Satellite-based vegetation roughness map

All dynamic roughness maps were derived from Sentinel-2 imagery. Based on the imagery quality of the Sentinel-2 dataset, the time interval between two contiguous dynamic roughness maps is not the same. This is due to both the acquisition characteristics (revisit time of 10 days at the equator with one satellite, and 5 days with 2 satellites, which results in 2-3 days at mid-latitudes), and to operational constraints. In fact, images with excessive cloud coverage (more than 20%) were excluded from the analysis, resulting in irregular temporal spacing. In addition, the number of active cells varies between dates because only cloud-free pixels were retained for vegetation height estimation and subsequent roughness calculation. Therefore, the differences in active cells reflect data availability after cloud masking rather than hydrological conditions.

This means that, although the total number of computational cells in the hydrodynamic mesh (i.e., the primary grid generated in the first modelling step) remains constant throughout all simulations, the number of cells participating in dynamic roughness modelling (i.e., active cells) varies due to differences in image quality (Table 4-3). For the Vistula Reach, the number of active cells remains relatively stable across the study period, ranging from approximately 3.3×10^5 to 5.9×10^5. Although some variability is observed between runs, all simulation dates involve several hundred thousand active cells, indicating a consistently extensive spatial coverage of roughness parameterization throughout the modeling period.

In contrast, the Po Reach exhibits significant variability in the number of active cells depending on the simulation. Grid numbers range from values on the order of 10^3 on several dates (e.g., early to mid-July and late September) to values exceeding 10^5 on other dates. This results in a markedly wider spread of cell numbers compared to the Vistula Reach.

Overall, the two study reaches show distinct temporal patterns in the spatial extent of grids involved in dynamic roughness simulations, with the Vistula Reach characterized by consistently high grid numbers and the Po Reach displaying strong inter-date variability. The date of every map and the number of grids used for modeling are shown in Table 4-3.

Table 4-3. Date of roughness maps and number of cells involved in the numerical modeling. The date is displayed as day/month of 2024.

Vistula		**Po**	
Date (Year 2024)	Number of cells for modeling	Date (Year 2024)	Number of cells for modeling
15/05	540799	27/05	42494
17/06	336655	01/06	88278
27/06	481082	16/06	97302
30/06	563598	06/07	99698

10/07	511748	09/07	1345
15/07	414435	11/07	12141
30/07	389784	16/07	1317
14/08	455244	21/07	1829
16/08	519498	26/07	133745
29/08	539837	29/07	138404
03/09	492076	31/07	2202
08/09	589726	08/08	2015
18/09	332454	10/08	2029
20/09	422757	13/08	1986
25/09	469676	23/08	146961
30/09	571628	25/08	2082
10/10	505206	28/08	2107
18/10	356055	30/08	2112
		09/09	122603
		29/09	1615
		22/10	1969

Three roughness maps were selected for each reach as an example to illustrate the variation in roughness throughout the simulation period (Figure 4-12).

For the Vistula Reach, the representative roughness maps display a high degree of spatial variations across the selected dates. Roughness values show a continuous banded pattern along the channel. Across the three examples, the overall spatial configuration remains comparable, with similar extents of low roughness and high roughness areas persisting between dates. Temporal differences among the maps are mainly expressed as localized changes in roughness magnitude within these reaches, rather than substantial changes in the spatial arrangement of roughness patterns.

In contrast, the representative roughness maps for the Po Reach show greater spatial complexity and stronger variability among the selected dates. Roughness values exhibit a more fragmented distribution, with distinct patches and sharper spatial contrasts between neighboring grid cells. The spatial extent and configuration of roughness maps differ visibly between dates, indicating less temporal consistency in the grid-scale roughness patterns compared to the Vistula Reach.

When comparing the two reaches, maps show clear differences in the spatial and temporal consistency of roughness fields (Figure 4-12). The Vistula Reach is characterized by relatively stable and continuous roughness patterns across dates, while the Po Reach shows more heterogeneous and temporally variable roughness distributions at the computational grid scale, reflecting a more complex vegetation structure.

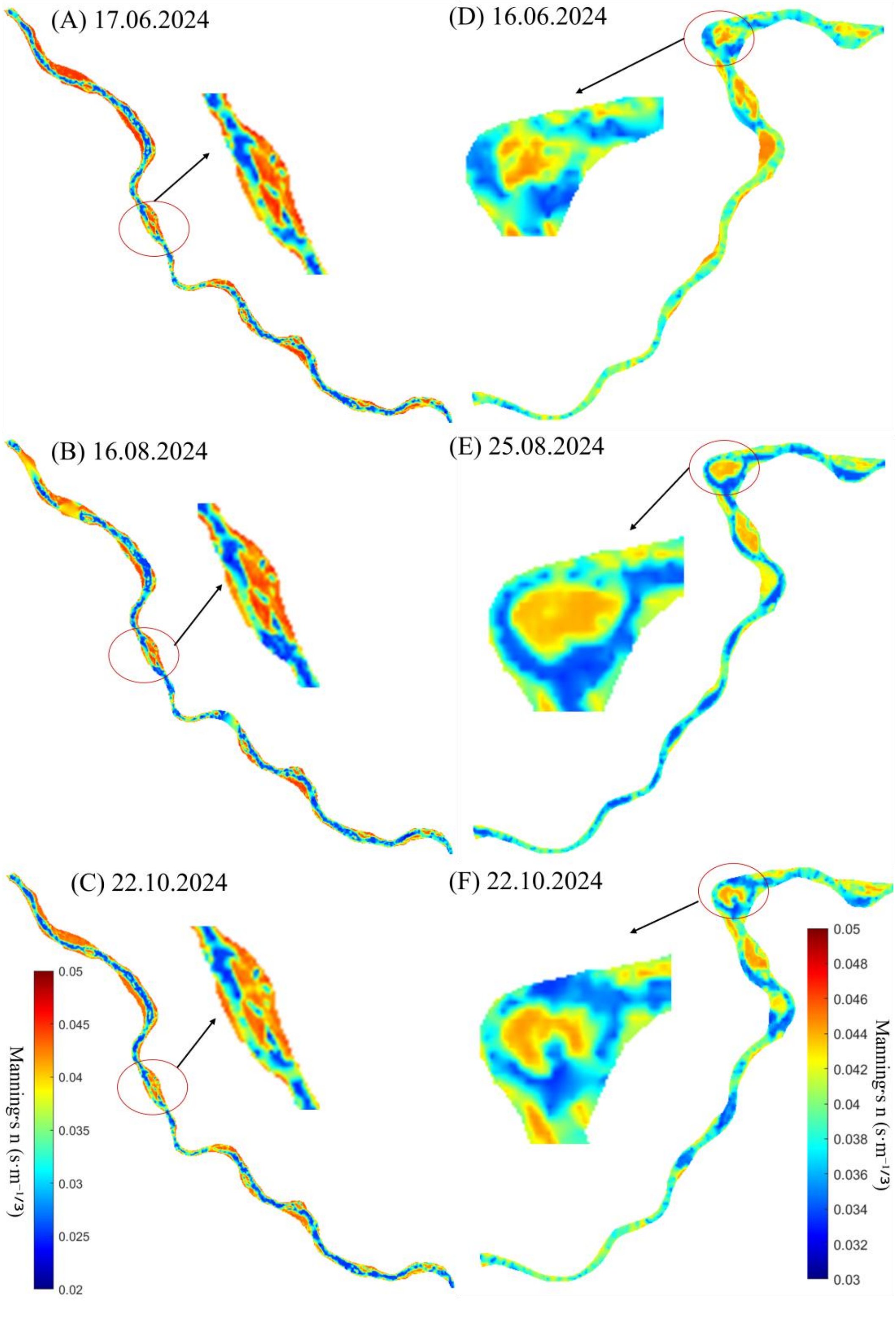

Figure 4-12. Roughness map used in modeling the Vistula Reach on (A) 06 June, (B) 23 August, and (C) 22 October, 2024; and the Po Reach on (D) 17 June, (E) 16 August, and (F) 22 October, 2024. The zoomed areas are shown as examples to illustrate variations in rougness.

4.4.4 Comparison between simulated and observed discharges in the Vistula Reach

The difference between observed discharge and discharge simulated using two different *n* values in the Vistula Reach is reported in Figure 4-13.

Simulations using the calibrated *n* (hereafter referred to as fixed *n*), which was 0.06, showed a generally strong agreement with the observed discharge, with an r_P^2 of 0.94 and an *NSE* of 0.90, indicating that the overall temporal distribution of discharge was well simulated. The *PBIAS* of −9.96% reflected an overall underestimation during the simulation period, mainly associated with higher discharge conditions.

When the estimated satellite-based roughness (hereafter referred to as dynamic *n*) was applied, the overall model performance improved. The r_P^2 increased to 0.97, while the *NSE* remained at 0.92, and the *PBIAS* was reduced to −7.82%. These results indicated that, although both approaches achieved comparable overall performance, the dynamic roughness scheme reduced underestimation, particularly by decreasing discharge bias under high-flow conditions.

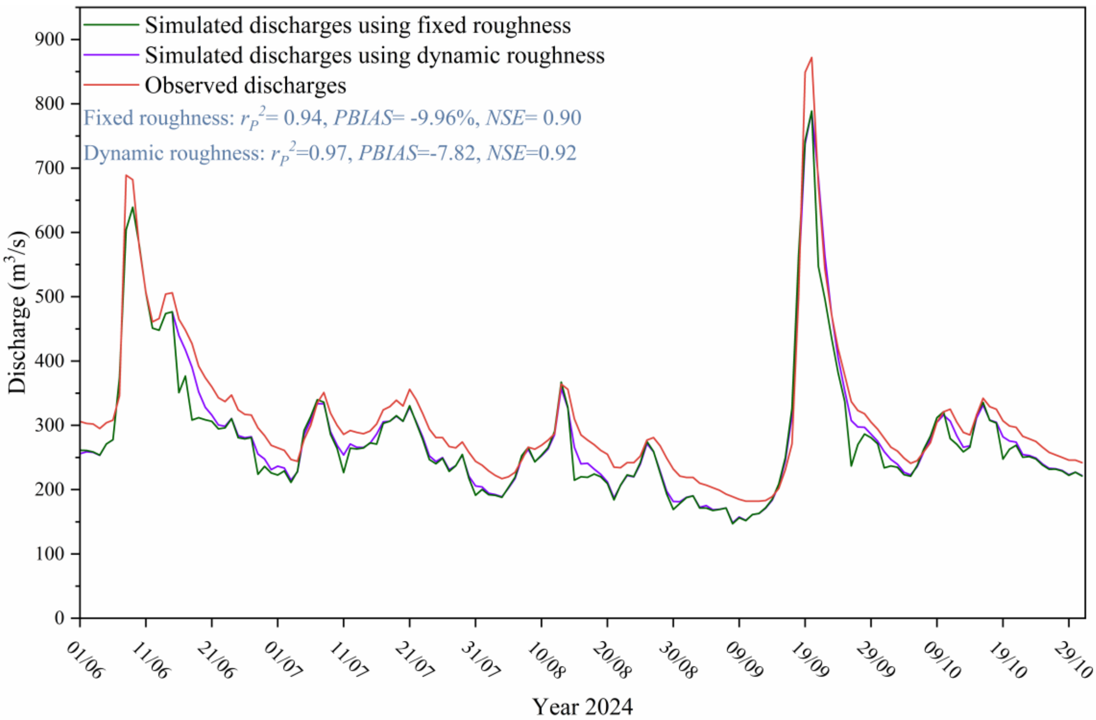

Figure 4-13. Observed and simulated discharges at the Gusin Station in the Vistula Reach at a daily scale using inputs from calibrated *n* (0.06) and satellite-based *n*. Note that this *x*-axis reports the time as day/month of 2024.

During June and early July, as well as mid to late July and throughout August, when discharge was predominantly low (approximately 180–260 m³/s) to moderate (approximately 690 m³/s), both fixed and dynamic *n* simulations closely match the observed discharge, and differences between the two approaches are relatively small, suggesting that model sensitivity to roughness variations is limited under low discharge conditions. It can be noted that, under low discharge conditions, both simulations with fixed and dynamic roughness exhibit slightly larger short-term fluctuations, although their overall discharge levels remain comparable and close to the observations.

More differences were found during mid-September to early October, when higher discharge events occurred. In this period, both fixed and dynamic *n* tend to underestimate the observed discharge around peak conditions. However, the dynamic *n* simulation produced peak and recession discharges closer to the observations than the fixed roughness case (Rucinska 2015), which explains the improved *PBIAS*. Importantly, the timing of peak discharge was well captured by both approaches, with no obvious delay or advance relative to observations, indicating that the main improvement from dynamic roughness lies in reducing discharge bias rather than altering peak timing (Rucinska 2015).

Overall, the dynamic roughness achieves a performance comparable to the fixed roughness. By reducing underestimation during high discharge conditions while maintaining accurate peak timing, the dynamic roughness provides more reliable discharge simulations.

4.4.5 Comparison between simulated and observed discharges in the Po Reach

The comparison between the discharge simulated using fixed and dynamic n and observed discharge is illustrated in Figure 4-13.

For the Po Reach, simulations using fixed n showed a strong agreement with the observed discharge, with an r_P^2 of 0.96 and an *NSE* of 0.90. Similar to the Vistula Reach, the *PBIAS* of −13.92% indicated an underestimation, which is mainly observed during medium to high flow conditions, while the overall temporal pattern of discharge is well reproduced.

When the dynamic n is applied, the overall statistical performance remains very similar. The r_P^2 and *NSE* remain unchanged at 0.96 and 0.90, respectively, while the *PBIAS* slightly improves to −13.8%. This small improvement indicates that dynamic roughness slightly reduces the extent of underestimation during some higher flow periods. In terms of overall agreement, the two roughness schemes produce nearly identical discharge simulations for the Po Reach, and, for most of the simulation period, the discharge curves obtained using fixed and dynamic roughness almost overlap and closely follow the observed discharge.

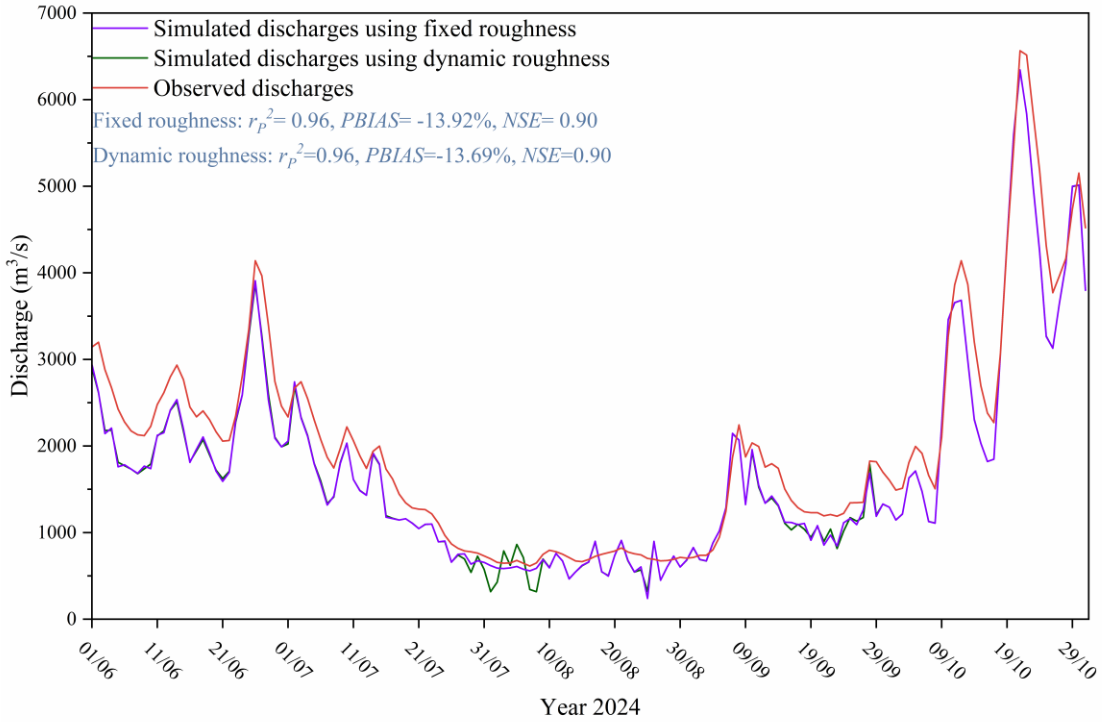

Figure 4-14. Observed and simulated discharges at Borgoforte Station in the Po Reach at a daily scale using inputs from calibrated *n* (0.06) and satellite-based *n*. Note that this figure is given as day/month of 2024.

From Figure 4-14, it can be noticed that fixed *n* and dynamic *n* produced nearly overlapping results in terms of discharge at the downstream end, except for the period from late August to mid-October.

During early summer, discharge showed strong temporal variability, and noticeable differences between fixed and dynamic *n* simulations were observed during periods of rapid discharge change. The two simulations differ more during periods of rapid flow change, when discharge varies by around 200 m^3/s to over 1000 m^3/s within a few days, even though their discharge values remain very similar, with differences typically limited to a few tens of m^3/s compared to peak discharges exceeding 3000 to 6000 m^3/s. Until late July, when discharge decreased to relatively low levels, the two simulations became very close to the observed discharge. Both simulations using fixed and dynamic roughness behave similarly under low-flow conditions, indicating that model sensitivity to roughness variations was limited.

During late summer to early autumn (September to October), higher discharge events occurred, and both fixed and dynamic *n* simulations tended to underestimate discharge around peak conditions, which largely explained the negative *PBIAS* values. Despite this underestimation, the timing of the peak discharge was well reproduced by both simulations, with no obvious delay or advance relative to observations. Compared to the fixed *n*, the dynamic roughness simulation showed slightly better agreement in discharge magnitude during some high discharge events, as reflected by the marginal improvement in *PBIAS*.

Overall, fixed and dynamic *n* simulations showed comparable performance for the Po Reach. Differences between the two approaches were generally small, and the discharge curves largely overlapped during low discharge periods, while the dynamic roughness provided a modest improvement during some higher discharge events. Further discussion of these results and the underlying mechanisms is provided in the following section.

Chapter 5 Discussion

5.1 Machine learning model to estimate vegetation height

The extraction of vegetation characteristics, particularly vegetation height, has long been recognized as a challenging task (Lang et al. 2023, Chen et al. 2024, Zhang et al. 2024, Zhou et al. 2024). In fact, traditional field-based measurements are typically designed to characterize vegetation under specific and static conditions (Xie *et al.* 2008, Schad *et al.* 2025). Once vegetation conditions change, for example, in terms of density, species, or growth stage, such measurements are generally unable to represent these vegetative dynamics (Luhar and Nepf 2013, Feng *et al.* 2024, Hou *et al.* 2025).

Satellite imagery provides long-term and continuous observations and, therefore, could be effectively used to describe temporal variations in vegetation conditions (Wallace *et al.* 2006, Darabi *et al.* 2025). However, most satellite products are limited by moderate spatial resolution (10 and 30 m, for Sentinel and Landsat missions, respectively), which is often insufficient to resolve detailed vegetation structure (Chen, Zhou, *et al.* 2023, Radeloff *et al.* 2024). Moreover, vegetation conditions are commonly characterized using multispectral vegetation indices derived from satellite imagery, which primarily reflect canopy spectral responses related to greenness and vigor rather than vegetation structure such as vegetation height and diameter (Asner 1998, Gitelson 2004, Farwell *et al.* 2021, Radeloff *et al.* 2024). As a result, important vegetation structural parameters like vegetation height are difficult to obtain directly from satellite imagery alone, and are therefore obtained using other non-contact techniques such as LiDAR, or data derived from UAV-based photogrammetry (Datt 1999, Lefsky *et al.* 2002, Dandois and Ellis 2013, Bendig *et al.* 2014, Liu *et al.* 2019, Potapov *et al.* 2021).

Establishing a reliable relationship between multispectral indices and vegetation height is the key challenge of this study. Simple linear or polynomial regression approaches often fail to capture the complex and nonlinear interactions between spectral responses and vegetation structure (Farwell *et al.* 2021, Lourenço *et al.* 2021, Guo *et al.* 2025). To address this limitation, innovative machine learning approaches were introduced in this study, as they have shown promising performance in vegetation monitoring (Pan *et al.* 2023, Guo *et al.* 2025, Hou *et al.* 2025, Nasiri *et al.* 2025). Specifically, Random Forest (RF) and Extra Trees (ET) models were employed to explore the relationship between multispectral indices and vegetation height (Belgiu and Drăgu 2016, Wang *et al.* 2021, Nasiri *et al.* 2025). Although machine learning approaches demonstrated relatively strong performance in this study, there are some key points worth discussing.

First of all, there is a difference in model performance between vegetation height in the range 0-3 m and 3-20 m. The reason why 3 m is used as the threshold is that it represents a clear structural transition in vegetation height across the study sites (Figure 5-1). Although vegetation height is continuous and does not show a sharp natural breakpoint at exactly 3 m, the empirical cumulative distribution function (ECDF) of vegetation height indicates that the proportion of samples below and above 3 m differs substantially among ROIs. In some ROIs, most vegetation remains below 3 m and is mainly composed of grass and shrubs, while in others a larger proportion exceeds 3 m, indicating the presence of taller woody vegetation. This distinction reflects a meaningful difference in vegetation structure. Therefore, 3 m is adopted as a practical threshold to separate low vegetation from taller canopy vegetation, and the ML models are trained separately for the two height ranges.

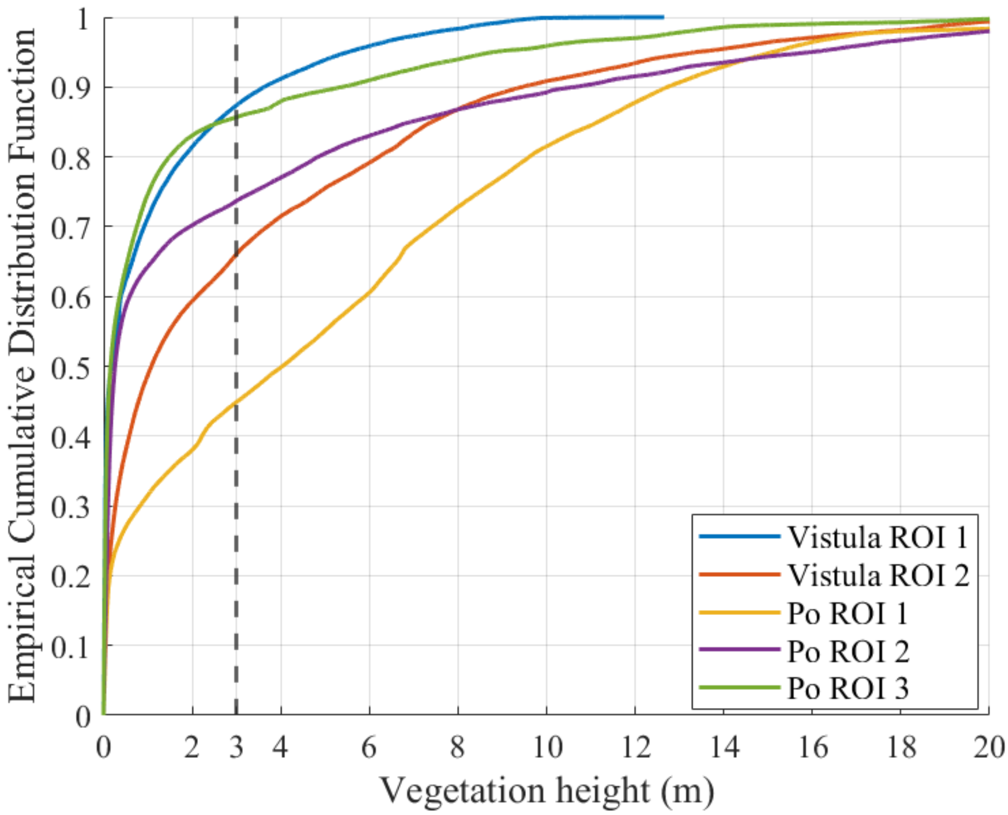

Figure 5-1. Empirical cumulative distribution function (ECDF) of vegetation height across ROIs.

The better performance of the machine learning model in the 0 - 3 m vegetation height range across the Vistula, Po, and Vistula+Po case studies is closely related to both vegetation structure and spectral sensitivity. Low vegetation is typically composed of grasses and low shrubs with relatively simple canopy structures, for which multispectral vegetation indices (e.g., NDVI, GNDVI, and NDRE) are highly sensitive to changes in leaf area and vegetation density (Huete *et al.* 2002, Glenn *et al.* 2008). In this height range, spectral indices remain sensitive to changes in low vegetation, allowing the model to learn a more stable relationship between spectral features and vegetation height (Glenn *et al.* 2008). In addition, UAV-based photogrammetric height estimates tend to have smaller relative errors at low heights, often within the centimeter-to-decimeter range (Dandois and Ellis 2010, Anderson and Gaston 2013), which further improves the consistency of the training data for vegetation lower than 3 m. However, model performance decreases in the 3 to 20 m vegetation height range across all regions, reflecting limitations in the input feature space rather than deficiencies in the learning algorithm itself. As vegetation height and canopy complexity increase, multispectral vegetation indices tend to have saturation effects, where spectral responses no longer change linearly with height (Huete *et al.* 2002, Mutanga and Skidmore 2004). Under such conditions, vegetation with different heights may correspond to similar spectral signatures, reducing the model's ability to classify medium and tall vegetation. In addition, taller vegetation is associated with more complex vertical structures and shadowing effects, which are difficult to capture using standard multispectral indices alone (Asner *et al.* 2012). As a result, predictions in the 3-20 m range tend to be more dispersed, with increased *RMSE* and reduced explanatory power.

Moreover, horizontal banding patterns are observed in the scatter plots in Figures 4-2(A), 4-2(B), 4-3(A), and 4-4(A), which are common characteristics of tree-based regression models, such as Random Forest and Extra Trees (Breiman 2001). Namely, as explained in Figure 5-2, tree-based regression models do not produce continuously varying outputs (Breiman 2001, Scornet 2013, Neufeld *et al.* 2022). Instead, the feature space is divided into a series of regions, and all samples falling within the same region are assigned the same predicted value (Belgiu and Drăgu 2016). Therefore, even when vegetation height varies smoothly in reality, the machine learning model may output a limited number of discrete height levels, causing more apparent clustering in parts of the feature space where multispectral variability is low or where training samples are sparse or unevenly distributed (Quinlan 1992, Biau and Scornet 2016, Mentch and Hooker 2016, Georganos *et al.* 2018). In this study, banding is evident in both the 0 to 3 m and 3 to 20 m ranges, but becomes more frequent at higher vegetation heights, where spectral saturation and uneven sample distributions are more prominent. Importantly, these bands are not random noise, but rather a systematic response of the model under limited feature information. Although such discretization may introduce some uncertainty in the estimated vegetation height, its impact on the hydrodynamic model predictions is expected to be limited. This is because hydraulic simulations are primarily controlled by large-scale spatial patterns of roughness rather than small local variations, particularly in large rivers where roughness values are spatially averaged at the grid scale (Horritt and Bates 2002; Pappenberger *et al.* 2005).

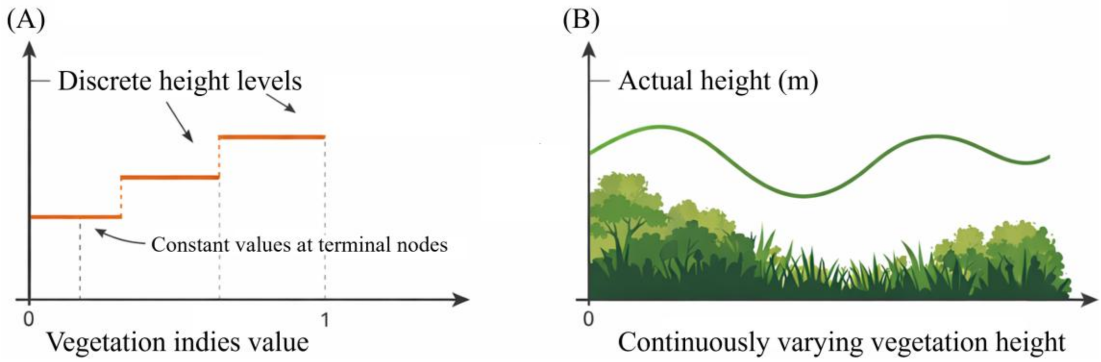

Figure 5-2. Comparison between tree-based step functions and continuous vegetation dynamics. (A) Discontinuous piecewise constant predictions derived from a tree-based regressor; (B) continuous spatial and temporal variation of actual vegetation.

In addition, clear banding patterns have not been found in Figure 4-3(B) and 4-4(B). Namely, in the Po and Vistula+Po Reach, clear banding patterns occur less frequently in the higher vegetation height range. This difference is mainly related to the underlying distribution of vegetation height and the increased heterogeneity of the input data. In the Po reach, tall vegetation exhibits a more continuous height distribution, spanning multiple height levels, which prevents model predictions from clustering around a small number of discrete values, a behavior consistent with the piecewise constant nature of tree-based regression models (Breiman 2001, Hengl *et al.* 2018). In addition, under tall vegetation conditions, similar multispectral signatures may correspond to different heights, further dispersing model outputs (Lefsky *et al.* 2002). In the combined dataset, the inclusion of samples from multiple regions increases this heterogeneity, eventually resulting in broader scatter distributions rather than distinct horizontal bands (Meyer *et al.* 2019).

Except for the horizontal banding patterns, rectangular empty regions in the lower-right part of the scatter plots, representing cases with low observed height but high simulated height, indicate that such combinations are rare across all regions and height ranges. From a machine learning perspective, this suggests that the model behaves conservatively under low vegetation height conditions, avoiding strong overestimation. This behavior is closely linked to the distribution of training samples, where low vegetation is generally associated with low spectral responses (Meyer *et al.* 2019). As a result, the model learns a stable mapping that prevents extreme predictions in this part of the feature space. Such conservative behavior is advantageous in practice, as it reduces the risk of producing unrealistic height estimates in low vegetation areas (James *et al.* 2021).

In addition, although the Vistula and the Po reaches are different in geographical setting, climate, and vegetation composition, the machine learning results show strong similarity in both evaluated metrics and distribution patterns. This suggests that the model primarily learns general relationships between multispectral features and vegetation height, rather than reach-specific characteristics. In particular, low vegetation height exhibits transferable spectral–structural relationships across regions, allowing the model to maintain consistent performance. A similar model behavior across regions has also been found in previous studies using multispectral-based machine learning approaches (Pelletier *et al.* 2016, Maxwell *et al.* 2018), indicating that the method proposed in this study can be applied to multiple regions, also beyond the study areas.

When the Vistula and Po datasets are trained separately, the models only learn region-specific relationships between multispectral information and vegetation height. In general, more training data is expected to improve model performance when the relationship between the input features and the target variable remains consistent (Linjordet and Balog 2019). However, this assumption is not true when datasets from multiple regions with distinct vegetation composition, background reflectance, and environmental conditions are combined (Weiss *et al.* 2016, Linjordet and Balog 2019, Reichstein *et al.* 2019). In this study, similar multispectral index values can represent very different vegetation heights in different regions. This is mainly because vegetation structure, species composition, and canopy density vary between the Vistula and Po reaches, which affects the spectral response. As a result, the relationship between MVIs and *h* becomes less consistent when data from multiple regions are combined. It can be noticed from Table 4-2 that for short vegetation (0–3 m), the single region models achieved an R^2 of 0.74 in both reaches, with *RMSE* values of 0.29 m (Vistula) and 0.30 m (Po). After combining the datasets from two reaches, R^2 slightly decreased to 0.72 and *RMSE* increased to 0.33 m. The difference becomes more evident for taller vegetation (3–20 m). In the single region models, R^2 ranged from 0.61 to 0.63, while in the combined model, it decreased to 0.57. At the same time, *RMSE* increased from 2.11–2.18 m to 2.30 m, and *PBIAS* also became slightly larger. These results suggest that including data from different regions improves the robustness of the model but also introduces higher uncertainty, particularly for taller and more structurally complex vegetation. Similar effects of data heterogeneity and domain mismatch on model stability and prediction uncertainty have been widely reported in multi-region and cross-domain remote sensing studies (Tuia *et al.* 2016, Weiss *et al.* 2016, Reichstein *et al.* 2019).

Five MVIs, which are most commonly used in vegetation monitoring, were used in this study to better characterize vegetation conditions. Each index captures different aspects of vegetation properties. NDVI reflects vegetation vigor but is subject to high biomass (Huete *et al.* 2002), OSAVI considers the soil background (Steven 1998), NDRE is more sensitive to dense canopy conditions (Boonupara *et al.* 2024), and GNDVI responds better to chlorophyll or nitrogen variations (Barati *et al.* 2011). By combining these indices, the model can use complementary spectral information instead of relying on a single index, which may suffer from saturation or limited sensitivity (Nițu *et al.* 2025, Yan *et al.* 2025, Chrysostomou *et al.* 2026).

However, adding more MVIs does not directly improve accuracy (Ibrahim *et al.*

2024, Chatterjee *et al.* 2025). If the indices are highly correlated, the additional information may be redundant (Yan *et al.* 2025). Therefore, the benefit of using multiple MVIs depends on whether the model can effectively extract useful information from them (Deng *et al.* 2024, Matyukira and Mhangara 2024, Chatterjee *et al.* 2025). In this study, the nonlinear learning framework helps capture these relationships and partly compensates for the increased heterogeneity across regions.

In conclusion, although the machine learning model uncertainty increases at medium to tall vegetation heights, the stable performance observed in the 0 to 3 m range is particularly relevant for subsequent applications. In fact, low vegetation typically dominates floodplains and vegetated bars, where small changes in height can have a pronounced effect on the hydraulic roughness (Naiman *et al.* 2005, Baptist *et al.* 2007, Nepf 2012b). Therefore, the reliable performance of the model in this relatively low range provides a solid basis for estimating dynamic roughness from vegetation height, in particular as far as grass and bushes are concerned.

5.2 Evaluation of satellite-driven vegetation height

A comparison between *h* estimated from Sentinel-2 multispectral imagery and UAV-derived *h* acquired on the same date was used to further evaluate the model performance and demonstrated that the trained ML model can reliably capture spatial variations in vegetation height across both rivers. The high similarity observed from Figures 4-6 and 4-7 for both the Vistula and Po reaches indicates that the relationship learned between multispectral indices and vegetation height is reliable, despite the indirect nature of optical observations of vegetation structure.

Trained machine learning (ML) model performance is particularly stable in low vegetation height ranges, where scatter is limited, and systematic bias remains small. This behavior can be explained by both remote sensing and ML considerations. Under low vegetation conditions, multispectral indices remain sensitive to changes in canopy cover and structure, allowing height variations to be more clearly distinguished (Glenn *et al.* 2008). At the same time, low vegetation heights dominate floodplains and vegetated bars, especially in the case of large lowland rivers such as the two case studies, resulting in a denser and more representative training sample distribution in this range, which constrains tree-based models to produce conservative and stable predictions rather than extreme extrapolations (James *et al.* 2021).

Increased scatter at higher vegetation heights reflects the inherent limitations of multispectral data in resolving complex vertical canopy structure. As vegetation height and structural complexity increase, similar spectral responses may correspond to different canopy configurations, leading to greater uncertainty in height estimation (Lefsky *et al.* 2002, Asner *et al.* 2012). Differences between the Vistula and Po Reaches further suggest that regional heterogeneity in vegetation composition and spatial structure influences the model behavior, a pattern commonly reported in cross-region machine learning applications using multispectral data (Pelletier *et al.* 2016, Tuia *et al.* 2016).

Additionally, the striping pattern can also be observed in Figures 4-6 and 4-7. This condition is mainly related to the discrete nature of the satellite-derived MVIs used as model inputs. Sentinel-2 imagery has a limited set of reflectance values at a spatial resolution of 10 m, which leads to repeated or very similar index values across many pixels. When these discrete inputs are used in tree-based machine learning models, the predictions tend to form clusters with similar output values. Therefore, the predicted vegetation heights appear as vertical bands when compared with the continuous UAV-measured vegetation heights. However, this pattern does not indicate a modelling error and has no significant impact on the model performance, while it reflects the combined effects of the discretized remote sensing predictors and the prediction behavior of tree-based models. Similar patterns have also been reported in previous studies using tree-based models with remote sensing predictors (Belgiu and Drăgu 2016, Maxwell *et al.* 2018).

Overall, these results indicate that the proposed multispectral-based machine learning approach provides reliable vegetation height estimates at the floodplain scale, particularly for low vegetation, where small variations in vegetation height can significantly affect hydraulic roughness under shallow flow conditions. (Baptist *et al.* 2007, Nepf 2012a). This supports the suitability of the estimated vegetation height as an input for subsequent roughness parameterization in hydrodynamic modeling.

5.3 Effects of dynamic satellite-based roughness on discharge

Hydrodynamic models represent flood processes to support flood risk assessment and management, although their outputs are highly sensitive to input parameters (Guo *et al.* 2025), among which hydraulic roughness is widely recognized as a major source of uncertainty (James *et al.* 2021). In most commonly used models, vegetation effects are somewhat ignored, and a fixed roughness parameter is used to explain flow resistance (Chow 1959). Such an assumption may be acceptable in channels with stable bed conditions or limited vegetation, but it becomes inadequate in rivers with extensive floodplains and vegetated bars, where spatial heterogeneity in vegetation strongly influences flow dynamics (Baptist *et al.* 2007, Nepf 2012b). In these cases, low vegetation typically dominates floodplains and bars, and even small changes in vegetation height can significantly affect hydraulic roughness under shallow flow conditions (Green 2005, Nikora *et al.* 2008, Vargas-Luna *et al.* 2015).

To reduce the uncertainty of hydrodynamic models caused by roughness parameters, this study introduces a dynamic roughness parameter derived from satellite observations and machine learning, which is applied as a time-varying input to the hydrodynamic model. Simulated discharges obtained using dynamic roughness n are compared with simulations based on a fixed n, as well as with observed values, for both the Vistula and Po reaches, to examine model sensitivity to roughness variation under contrasting vegetation conditions. Across both study regions, differences between fixed and dynamic roughness simulations are not uniform throughout the simulation period, but become more obvious under specific hydrological conditions, particularly during periods of rapid discharge change and higher flow conditions, while, under stable discharge conditions, the difference between the two simulations remains small. This is consistent with the satellite-derived roughness maps, which show clear differences in the spatial distribution of roughness across dates and between the two rivers, indicating that the impact of vegetation-derived roughness on simulated discharge depends on the discharge conditions, rather than remaining constant over time.

During low discharge periods, as shown in Figures 4-13 and 4-14, the mean simulated discharge obtained using fixed and dynamic roughness remains similar in both the Po and Vistula rivers, indicating that the mean flow discharges are relatively insensitive to roughness variations when flow depths are shallow, at least at the analyzed daily time scale. Similar results have been widely proven in previous hydrodynamic modelling studies, where discharge is mainly constrained by the channel geometry, cross-sectional control, and baseflow supply rather than by moderate variations in hydraulic resistance under medium flow conditions (Ferguson 2007, Neal *et al.* 2015). However, despite the similarity in mean discharge levels, both roughness formulations exhibit more pronounced short-term fluctuations under low-flow conditions, reflecting the inherent sensitivity of shallow flows to small perturbations in effective roughness.

When discharge and water levels are low, even very small changes in water depth can already trigger noticeable changes in wetted area, effective roughness, and flow resistance (Nikora *et al.* 2001, Nepf 2012b). This especially occurs in river reaches with exposed bars and partially inundated floodplains, where small water level fluctuations can hugely influence the bed roughness value, leading to the floating in discharges (Green 2005, D'ippolito *et al.* 2021, Nicosia and Ferro 2023). It is thus explained why both rivers exhibit stronger short-term discharge fluctuations during low-flow periods, even though their average discharge is still well reproduced by both fixed and dynamic roughness simulations. Importantly, these fluctuations arise from physical interactions between flow depth and roughness under shallow-water conditions, rather than from numerical instability of the hydrodynamic model, as reported in previous modelling studies (Lane *et al.* 2004, Bates *et al.* 2010).

This effect is more significant in the Po River. As shown by the 2D flow patterns (Figure 4-2) and the discharge time series (Figure 4-14), during August, when both discharge and water levels are low, sandbars lie only slightly above the water surface. Under these conditions, even small changes in water level can change the states of bars and vegetation that they are submerged or exposed and the submerged extent, which immediately alters flow pathways and leads to rapid changes in effective roughness (Nepf, 2012b). Because roughness directly controls flow resistance (Ferguson 2007, Sikora *et al.* 2024, Zhang *et al.* 2025), low discharge conditions increase the impact of small depth variations, leading to huge short-term variability in simulated discharge. The observed discharge fluctuations, therefore, reflect the natural sensitivity of shallow flows to roughness variations, rather than artefacts related to model instability.

At the reach scale, simulated discharge using fixed and dynamic roughness in the Po River is largely similar for most of the simulation period (Figure 4–12). Differences arise primarily during periods when the dynamic roughness fields exhibit strong spatial contrasts and rapid temporal changes, as shown in Table 4-2 and the roughness maps. Floodplains and bars in the Po River are characterized by mixed distributions of trees, shrubs, and grasses, resulting in highly heterogeneous canopy structures, which limit the ability of multispectral satellite data to fully understand vegetation characteristics, particularly in areas with dense or multi-layered canopies (Asner *et al.* 2012). Therefore, during dynamic roughness estimation, grid cells associated with highly uncertain vegetation information are excluded, leading to strong temporal variability in the number of roughness map grids actively participating in modeling, ranging from several hundred thousand on some dates to only a few thousand on others (Table 4-2). From a machine-learning perspective, this represents a conservative prediction strategy, in which model outputs are constrained by the reliable subset of training data rather than being driven by uncertain inputs (James *et al.* 2021). When the spatial coverage of valid roughness grids is limited, the reach-scale roughness field becomes less spatially representative, and the resulting discharge simulations tend to remain close to those obtained using fixed roughness. Conversely, when a larger number of grids contribute to the dynamic roughness field, clearer deviations between the two roughness configurations become detectable, although overall statistical performance remains comparable. In contrast, the Vistula River is mainly characterized by low vegetation with a relatively simple and homogeneous structure (Figure 4-1), which facilitates a more direct relationship between multispectral indices and vegetation conditions (Naiman *et al.* 2005, Glenn *et al.* 2008). The corresponding roughness maps (Figure 4-12) show spatially continuous and coherent roughness patterns across dates, with roughness values forming relatively stable bands along the channel. Low and sparsely distributed vegetation typically has reduced canopy complexity, limiting spectral saturation and shadowing effects, which are commonly observed in taller or denser canopies (Mutanga and Skidmore 2004). Therefore, variations in vegetation cover and height can be more effectively captured by multispectral indices in optical satellite imagery (Baret and Guyot 1991, Nagler *et al.* 2005). From a hydrodynamic perspective, such vegetation conditions lead to a clearer contribution of vegetation-related resistance to the total flow resistance, particularly under low-flow conditions when the relative influence of bed roughness is reduced. Under these circumstances, changes in vegetation-induced roughness are more consistently transferred into the effective roughness parameter used in the hydrodynamic model (Wilson *et al.* 2003). Therefore, differences between simulations employing dynamic and fixed roughness formulations become more apparent during specific periods, especially during low-flow stages when vegetation resistance constitutes a larger fraction of the overall hydraulic resistance.

It can also be observed that, in both the Vistula and Po reaches, simulations using dynamic roughness exhibit smoother discharge time series than those using fixed roughness under low-discharge conditions following high-discharge events. This is because vegetation conditions changed during high-discharge periods. When it turns to a low discharge period, during which vegetation roughness exerts a stronger control on flow resistance, the fixed roughness fails to represent the changed vegetation conditions, while a dynamic roughness is able to capture these changes.

Most hydrodynamic models, including Delft3D FM, provide built-in vegetation or land use/cover (LULC) based roughness parameters, in which hydraulic resistance is assigned according to predefined LULC classes or vegetation types. (Prior *et al.* 2021, Feldmann *et al.* 2023, Deltares 2024) However, such parameterizations are built on discrete vegetation classifications and empirical lookup tables, which inherently assume internal homogeneity within each class and limited temporal variability (Prior *et al.* 2021, Sharpe *et al.* 2023). In river reaches characterized by complex bar morphology and highly heterogeneous vegetation patterns, these assumptions are difficult to satisfy and can introduce additional, poorly constrained parameters into the numerical model (Yassine *et al.* 2023). Due to the uncertainties associated with class-based roughness parameters and their additional assumptions, a fixed Manning's n is instead used as the baseline roughness and calibrated against observed discharge. Moreover, modeling using a fixed roughness value remains the most commonly used method in hydrodynamic modeling (Al-Asadi and Duan 2017, Ferreira *et al.* 2021). By using a calibrated fixed roughness as the reference, the comparison with the satellite-based dynamic roughness focuses on the effect of introducing explicitly dynamic vegetation resistance, while maintaining methodological consistency and ensuring the broader applicability of the proposed approach.

It can also be noticed that the calibrated fixed roughness value n is 0.06 in both the Vistula and the Po Reaches, while the satellite-based dynamic roughness values range from 0.01 to 0.05 (Figure 4-12), more in line with past studies (Nones 2019, Hamidifar *et al.* 2026). This difference is because the fixed roughness is applied to represent the whole simulation reach over the entire study period, so it has to describe all sources of flow resistance at the same time. When modelling, the model compensates for differences between the main channel and vegetated bars, for seasonal vegetation changes, and for small-scale resistance, which is thus not explicitly resolved by the model (James *et al.* 2004, Yassine *et al.* 2023). Therefore, the calibrated fixed roughness tends to be relatively high to have the best model performance, while the dynamic roughness changes in space and time (Morvan *et al.* 2008), with low values assigned to open-channel areas, while higher values are used for vegetated bars and floodplains. The real-time vegetation conditions can also be reflected by dynamic roughness. Therefore, its value range is lower and narrower, and the difference between fixed and dynamic roughness simply reflects their different roles in the numerical model. In conclusion, introducing dynamic roughness into the Delft3D FM model does not lead to a significant shift in flood wave peak timing, but it improves the consistency of simulated discharge magnitudes and reduces systematic bias associated with roughness parameterization. The benefits of dynamic roughness are most obvious under shallow flow conditions and in river reaches where vegetation dynamics exert a strong control on hydraulic resistance. Such conditions are typically characterized by frequent exposure of bars and floodplains during low-flow periods, dominance of low to intermediate vegetation, and pronounced seasonal variability in vegetation cover, all of which can be reliably identified from optical satellite imagery (e.g., Landsat missions) through moderate vegetation index values and clear temporal dynamics (Baret and Guyot 1991, Glenn *et al.* 2008, Nones and Guo 2026).

Chapter 6 Conclusions

In rivers characterized by extensive floodplains and vegetated bars, hydrodynamic models commonly use fixed roughness values to account for flow resistance. However, this assumption is different from real conditions and becomes inadequate in systems where vegetation covering in-channel bars varies seasonally and interacts strongly with flow dynamics. To address this limitation, the current study developed an integrated framework combining remote sensing and machine learning to estimate vegetation height and derive dynamic roughness, which was subsequently incorporated into hydrodynamic discharge simulations for selected reaches of the Vistula and Po rivers. The resulting simulations are intended to better support flood modeling and flood management, particularly in vegetated river systems where vegetation strongly influences flood processes by modifying hydraulic resistance.

The results of this study can be summarized as follows:

1. Relationships between multispectral vegetation indices and vegetation height were established using UAV-derived measurements. The results indicate that the model performs best in the low vegetation height range (0–3 m), with R^2 values around 0.74, *RMSE* of approximately 0.29–0.30 m, and *PBIAS* close to 7%, demonstrating a reliable capability to capture spatial variations in low vegetation conditions. In the higher vegetation range (3–20 m), uncertainty increases, although the overall relationship remains reasonable with the R^2 values around 0.6, *PBIAS* values around 3.7%, and *RMSE* values around 2 m. These reflect the characteristics of multispectral remote sensing, which is more sensitive to low vegetation while having limited capability to resolve tall and structurally complex canopies. Comparisons among study areas further show that model performance is strongly influenced by vegetation structural complexity and sample distribution, with regions dominated by low vegetation being more favorable for stable training and generalization.

2. For vegetation height validation, the trained machine learning model was applied to Sentinel-2 imagery acquired on the same date as the UAV surveys. Comparisons with UAV measurements show good performances in both magnitude and temporal variability, with errors generally on the order of a few tens of centimeters and no pronounced systematic bias. This confirms that, despite known limitations under dense or tall vegetation, the combined multispectral and machine learning approach can provide stable reach-scale vegetation height estimates suitable for dynamic roughness calculation.

3. In the hydrodynamic simulations, discharge results obtained using dynamic roughness were compared with those based on a fixed roughness configuration. During the calibration period, under consideration of the balance between r_P^2, *PBIAS*, and *NSE*, an *n* value of 0.06 was selected as the best calibrated roughness value for both Vistula and Po Reaches modeling. In the Vistula River, both configurations achieved high performance, with calibrated r_P^2 values of approximately 0.94, *NSE* values of around 0.9, and a *PBIAS* of -9.97%. When dynamic roughness was applied, r_P^2 increased to about 0.97, *NSE* remained close to 0.92, and *PBIAS* improved to −7.82%, indicating a reduction in systematic underestimation without altering the overall hydrograph structure. In the Po River, the two roughness configurations yielded very similar r_P^2 and *NSE* values (around 0.96 and 0.90, respectively), and only minor differences in *PBIAS* (approximately −13.92% versus −13.69%), reflecting the limited contrast between dynamic and fixed roughness under highly complex vegetation conditions.

4. It can be noticed that model sensitivity to roughness variation is strongest under low-discharge and shallow flow conditions. In the Po Reach during August, when water levels are low and bar margins are close to the water surface, small water-level fluctuations can substantially alter the extent of flow interaction with bars and vegetation. This leads to rapid changes in effective roughness and amplified short-term discharge variability. Such fluctuations reflect the physical sensitivity of shallow flows

to roughness variation rather than model instability. In contrast, the Vistula River exhibits more stable channel geometry under low-flow conditions, resulting in smoother discharge behavior and more distinct differences between roughness parameterizations during certain periods.

In conclusion, this study demonstrates that dynamic roughness derived from multispectral remote sensing and machine learning can improve the statistical consistency of discharge simulations without modifying the fundamental structure of hydrodynamic models. While the magnitude of improvement depends on vegetation structure and data availability, the approach proposed in the present work is particularly effective in systems dominated by low vegetation and shallow flow conditions. These findings support the use of satellite-based dynamic roughness as a practical and scalable pathway for incorporating vegetation dynamics into hydrodynamic modeling and flood risk assessment.

Bibliography

Abedin, T., Xu, H., and Uddin, S., 2026. The impact of K selection in K fold cross-validation on bias and variance in supervised learning models. Scientific Reports, 16(1), 6084. https://doi.org/10.1038/s41598-026-37247-x

Acar, E., 2025. Evaluation of the Effect of Land Vegetation on Flood Cross Section in Open Channels. Düzce Üniversitesi Bilim ve Teknoloji Dergisi, 13(3), 1022–1039. https://doi.org/10.29130/dubited.1496571

Aishwarya, Rani, M., Kumari, P., Lavania, P., Gupta, G., Tiwari, P., Kumar Singh, R., Kumar, M., Dobriyal, M., Srivastav, M., and Kumar, P., 2026. An overview of remote sensing technology in forest management. In: Advanced Geospatial and Ground Based Techniques in Forest Monitoring, 37–59. https://doi.org/10.1016/B978-0-443-18949-4.00017-8

Akkala, A., Boubrahimi, S.F., Hamdi, S.M., Hosseinzadeh, P., and Nassar, A., 2025. Spatio-Temporal Graph Neural Networks for Streamflow Prediction in the Upper Colorado Basin. Hydrology, 12(3), 60. https://doi.org/10.3390/hydrology12030060

Aksoy, B., Öztürk, M., and Özölçer, İ.H., 2024. Effect of Bed Material on Roughness and Hydraulic Potential in Filyos River. Water, 16(20), 2934. https://doi.org/10.3390/w16202934

Akter, A., and Fahim, M.A.R., 2026. Modelling of Intense Rainfall-Induced Flash Flood Inundation Using Delft3D FM. Hydrology, 13(1), 7. https://doi.org/10.3390/hydrology13010007

Al-Asadi, K., and Duan, J.G., 2017. Assessing methods for estimating roughness coefficient in a vegetated marsh area using Delft3D. Journal of Hydroinformatics, 19(5), 766–783. https://doi.org/10.2166/hydro.2017.064

Anderson, B.G., Rutherfurd, I.D., and Western, A.W., 2006. An analysis of the influence of riparian vegetation on the propagation of flood waves. Environmental Modelling and Software, 21(9), 1290–1296. https://doi.org/10.1016/j.envsoft.2005.04.027

Anderson, K., and Gaston, K.J., 2013. Lightweight unmanned aerial vehicles will revolutionize spatial ecology. Frontiers in Ecology and the Environment, 11(3), 138–146. https://doi.org/10.1890/120150

Anzani, H.S., Kantoush, S.A., and Kobayashi, S., 2025. Impact of bed roughness configurations on flow dynamics and hydraulic resistance in open-channel flows. Scientific Reports, 16, 3614. https://doi.org/10.1038/s41598-025-33650-y

Arlot, S., and Celisse, A., 2010. A survey of cross-validation procedures for model selection. Statistics Surveys, 4, 40–79. https://doi.org/10.1214/09-SS054

Aronica, G., Bates, P.D., and Horritt, M.S., 2002. Assessing the uncertainty in distributed model predictions using observed binary pattern information within

GLUE. Hydrological Processes, 16(10), 2001–2016. https://doi.org/10.1002/hyp.398

Asner, G.P., 1998. Biophysical and biochemical sources of variability in canopy reflectance. Remote Sensing of Environment, 64(3), 234–253. https://doi.org/10.1016/S0034-4257(98)00014-5

Asner, G.P., Knapp, D.E., Boardman, J., Green, R.O., Kennedy-Bowdoin, T., Eastwood, M., Martin, R.E., Anderson, C., and Field, C.B., 2012. Carnegie Airborne Observatory-2: Increasing science data dimensionality via high-fidelity multi-sensor fusion. Remote Sensing of Environment, 124, 454–465. https://doi.org/10.1016/j.rse.2012.06.012

Augustijn, D.C.M., Huthoff, F., and Van Velzen, E.H., 2008. Comparison of vegetation roughness descriptions. In: Altinakar, M.S., Kokpinar, M.A., Darama, Y., Yegen, B., and Harmancioglu, N.B. (eds.), River Flow 2008: Proceedings of the 4th International Conference on Fluvial Hydraulics, Cesme, Izmir, Turkey, 3–5 September 2008. Ankara: Kubaba Congress Department and Travel Services, 343–350.

Babiński, Z., and Habel, M., 2013. Hydromorphological conditions of the lower Vistula in the development of navigation and hydropower. Acta Energetica, 2(15), 83–90. https://doi.org/10.12736/issn.2300-3022.2013206

Badora, D., Wawer, R., Król-Badziak, A., Nieróbca, A., Kozyra, J., and Jurga, B., 2023. Hydrological Balance in the Vistula Catchment under Future Climates. Water, 15(23), 4168. https://doi.org/10.3390/w15234168

Ballesteros, J.A., Bodoque, J.M., Díez-Herrero, A., Sanchez-Silva, M., and Stoffel, M., 2011. Calibration of floodplain roughness and estimation of flood discharge based on tree-ring evidence and hydraulic modelling. Journal of Hydrology, 403(1–2), 103–115. https://doi.org/10.1016/j.jhydrol.2011.03.045

Baptist, M.J., Babovic, V., Uthurburu, J.R., Keijzer, M., Uittenbogaard, R.E., Mynett, A., and Verwey, A., 2007. On inducing equations for vegetation resistance. Journal of Hydraulic Research, 45(4), 435–450. https://doi.org/10.1080/00221686.2007.9521778

Barati, S., Rayegani, B., Saati, M., Sharifi, A., and Nasri, M., 2011. Comparison the accuracies of different spectral indices for estimation of vegetation cover fraction in sparse vegetated areas. Egyptian Journal of Remote Sensing and Space Science, 14(1), 49–56. https://doi.org/10.1016/j.ejrs.2011.06.001

Baret, F., and Guyot, G., 1991. Potentials and limits of vegetation indices for LAI and APAR assessment. Remote Sensing of Environment, 35(2–3), 161–173. https://doi.org/10.1016/0034-4257(91)90009-U

Barinas, G., Good, S.P., and Tullos, D., 2024. Continental Scale Assessment of Variation in Floodplain Roughness With Vegetation and Flow Characteristics. Geophysical Research Letters, 51(1), e2023GL105588. https://doi.org/10.1029/2023GL105588

Barnes, E.M., Clarke, T.R., Richards, S.E., Colaizzi, P.D., Haberland, J., Kostrzewski, M., Waller, P., Choi, C., Riley, E., Thompson, T., Lascano, R.J., Li, H., and Moran, M.S., 2000. Coincident detection of crop water stress, nitrogen status and canopy density using ground-based multispectral data. USDA-ARS Technical Report 1356, U.S. Department of Agriculture, Agricultural Research Service.

Bates, P.D., Horritt, M.S., and Fewtrell, T.J., 2010. A simple inertial formulation of the shallow water equations for efficient two-dimensional flood inundation modelling. Journal of Hydrology, 387(1–2), 33–45. https://doi.org/10.1016/j.jhydrol.2010.03.027

Belgiu, M., and Drăgu, L., 2016. Random forest in remote sensing: A review of applications and future directions. ISPRS Journal of Photogrammetry and Remote Sensing, 114, 24–31. https://doi.org/10.1016/j.isprsjprs.2016.01.011

Bendig, J., Bolten, A., Bennertz, S., Broscheit, J., Eichfuss, S., and Bareth, G., 2014. Estimating Biomass of Barley Using Crop Surface Models (CSMs) Derived from UAV-Based RGB Imaging. Remote Sensing, 6(11), 10395–10412. https://doi.org/10.3390/rs61110395

Bertalan, L., Holb, I., Pataki, A., Négyesi, G., Szabó, G., Kupásné Szalóki, A., and Szabó, S., 2022. UAV-based multispectral and thermal cameras to predict soil water content – A machine learning approach. Computers and Electronics in Agriculture, 200, 107262. https://doi.org/10.1016/j.compag.2022.107262

Beven, K., 2012. Rainfall-Runoff Modelling: The Primer. 2nd ed. Chichester: John Wiley and Sons. https://doi.org/10.1002/9781119951001

Biau, G., and Scornet, E., 2016. A random forest guided tour. Test, 25(2), 197–227. https://doi.org/10.1007/s11749-016-0481-7

Blasi, C., Capotorti, G., Copiz, R., Guida, D., Mollo, B., Smiraglia, D., and Zavattero, L., 2014. Classification and mapping of the ecoregions of Italy. Plant Biosystems, 148(6), 1255–1345. https://doi.org/10.1080/11263504.2014.985756

Boardman, J., and Evans, R., 2020. The measurement, estimation and monitoring of soil erosion by runoff at the field scale: Challenges and possibilities with particular reference to Britain. Progress in Physical Geography, 44(1), 31–49. https://doi.org/10.1177/0309133319861833

Bogdanowicz, E., Karamuz, E., and Romanowicz, R.J., 2021. Temporal Changes in Flow Regime along the River Vistula. Water, 13(20), 2840. https://doi.org/10.3390/w13202840

Boonupara, T., Udomkun, P., Gibson-Poole, S., Hamilton, A., and Kaewlom, P., 2024. Assessing plant pigmentation impacts: A novel approach integrating UAV and multispectral data to analyze atrazine metabolite effects from soil contamination. Smart Agricultural Technology, 9, 100570. https://doi.org/10.1016/j.atech.2024.100570

Boothroyd, R.J., Williams, R.D., Hoey, T.B., Barrett, B., and Prasojo, O.A., 2021a. Applications of Google Earth Engine in fluvial geomorphology for detecting river channel change. Wiley Interdisciplinary Reviews: Water, 8(1), e1496. https://doi.org/10.1002/wat2.1496

Boothroyd, R.J., Nones, M., and Guerrero, M., 2021b. Deriving Planform Morphology and Vegetation Coverage From Remote Sensing to Support River Management Applications. Frontiers in Environmental Science, 9, 657354. https://doi.org/10.3389/fenvs.2021.657354

Box, W., Järvelä, J., and Västilä, K., 2021. Flow resistance of floodplain vegetation mixtures for modelling river flows. Journal of Hydrology, 601, 126593. https://doi.org/10.1016/j.jhydrol.2021.126593

Boyle, D.P., Gupta, H.V., and Sorooshian, S., 2000. Toward improved calibration of hydrologic models: Combining the strengths of manual and automatic methods. Water Resources Research, 36(12), 3663–3674. https://doi.org/10.1029/2000WR900207

Bozzi, S., Passoni, G., Bernardara, P., Goutal, N., and Arnaud, A., 2015. Roughness and Discharge Uncertainty in 1D Water Level Calculations. Environmental Modeling and Assessment, 20(4), 343–353. https://doi.org/10.1007/s10666-014-9430-6

Bozzola, M., and Swanson, T., 2014. Policy implications of climate variability on agriculture: Water management in the Po river basin, Italy. Environmental Science & Policy, 43, 26–38. https://doi.org/10.1016/j.envsci.2013.12.002

Breiman, L., 2001. Random forests. Machine Learning, 45(1), 5–32. https://doi.org/10.1023/A:1010933404324

Buszewski, B., Buszewska, T., Chmarzyński, A., Kowalkowski, T., Kowalska, J., Kosobucki, P., Zbytniewski, R., Namieśnik, J., Kot-Wasik, A., Pacyna, J., and Panasiuk, D., 2005. The present condition of the Vistula river catchment area and its impact on the Baltic Sea coastal zone. Regional Environmental Change, 5(2–3), 97–110. https://doi.org/10.1007/s10113-004-0077-8

Carp, A., 2023. Measuring Accuracy of the DJI Mavic 3 Enterprise RTK using DroneDeploy Photogrammetry. White paper. DroneDeploy.

Casulli, V., and Walters, R.A., 2000. An unstructured grid, three-dimensional model based on the shallow water equations. International Journal for Numerical Methods in Fluids, 32(3), 331–348. https://doi.org/10.1002/(SICI)1097-0363(20000215)32:3<331::AID-FLD941>3.0.CO;2-C

Cavallini, E., Viaroli, P., Naldi, M., Saccò, M., Scibona, A., Barbieri, E., Franceschini, S., and Nizzoli, D., 2024. Seasonal Variability and Hydrological Patterns Influence the Long-Term Trends of Nutrient Loads in the River Po. Water, 16(18), 2628. https://doi.org/10.3390/w16182628

Cerkowniak, G.R., Ostrowski, R., Schönhofer, J., Stella-Bogusz, M., Szmytkiewicz, M., and Szmytkiewicz, P., 2024. Optimized regulation of the Vistula River at its connection to the sea. Continental Shelf Research, 276, 105244. https://doi.org/10.1016/j.csr.2024.105244

Chatterjee, S., Baath, G.S., Sapkota, B.R., Flynn, K.C., and Smith, D.R., 2025. Enhancing LAI estimation using multispectral imagery and machine learning: A comparison between reflectance-based and vegetation indices-based approaches.

Computers and Electronics in Agriculture, 230, 109790. https://doi.org/10.1016/j.compag.2024.109790

Chaulagain, S., Stone, M.C., Dombroski, D., Gillihan, T., Chen, L., and Zhang, S., 2022. An investigation into remote sensing techniques and field observations to model hydraulic roughness from riparian vegetation. River Research and Applications, 38(10), 1730–1745. https://doi.org/10.1002/rra.4053

Chen, J., Liang, X., Liu, Z., Gong, W., Chen, Y., Hyyppä, J., Kukko, A., and Wang, Y., 2024. Tree species recognition from close-range sensing: A review. Remote Sensing of Environment, 313, 114337. https://doi.org/10.1016/j.rse.2024.114337

Chen, J., Wang, L., Jucker, T., Da, H., Zhang, Z., Hu, J., Yang, Q., Wang, X., Qin, Y., Shen, G., Shu, L., and Zhang, J., 2023. Detecting forest canopy gaps using unoccupied aerial vehicle RGB imagery in a species-rich subtropical forest. Remote Sensing in Ecology and Conservation, 9(5), 671–686. https://doi.org/10.1002/rse2.336

Chen, Q., Zheng, B., Chenu, K., Hu, P., and Chapman, S.C., 2022. Unsupervised Plot-Scale LAI Phenotyping via UAV-Based Imaging, Modelling, and Machine Learning. Plant Phenomics, 2022, 9768253. https://doi.org/10.34133/2022/9768253

Chen, Y., Cao, F., Cheng, W., Liu, B., and Yu, P., 2023. Real-time correction of channel-bed roughness and water level in river network hydrodynamic modeling for accurate forecasting. Scientific Reports, 13, 20660. https://doi.org/10.1038/s41598-023-42791-x

Cheng, N.S., 2011. Representative roughness height of submerged vegetation. Water Resources Research, 47(8), W08517. https://doi.org/10.1029/2011WR010590

Cho, H.J., Mishra, D., and Wood, J., 2012. Remote sensing of submerged aquatic vegetation. In: Escalante, B. (ed.), Remote Sensing – Applications. Rijeka: IntechOpen, 99–116. https://doi.org/10.5772/35156

Chou, J., and Chung, W.-C., 2024. Cloud Computing and High Performance Computing (HPC) Advances for Next Generation Internet. Future Internet, 16(12), 465. https://doi.org/10.3390/fi16120465

Chow, V.T., 1959. Open-channel hydraulics. New York: McGraw-Hill.

Chrysostomou, C., Neophytides, S.P., Mavrovouniotis, M., and Hadjimitsis, G., 2026. Optimized spectral indices for global vegetation and water mapping using Sentinel-2. Scientific Reports, 16, 4491. https://doi.org/10.1038/s41598-025-34720-x

Claverie, M., Ju, J., Masek, J.G., Dungan, J.L., Vermote, E.F., Roger, J.C., Skakun, S.V., and Justice, C., 2018. The Harmonized Landsat and Sentinel-2 surface reflectance data set. Remote Sensing of Environment, 219, 145–161. https://doi.org/10.1016/j.rse.2018.09.002

Clevers, J.G.P.W., and Gitelson, A.A., 2013. Remote estimation of crop and grass chlorophyll and nitrogen content using red-edge bands on Sentinel-2 and -3. International Journal of Applied Earth Observation and Geoinformation, 23(1), 344–351. https://doi.org/10.1016/j.jag.2012.10.008

Copernicus Land Monitoring Service, 2020. CORINE Land Cover 2018 (vector), Europe, 6-yearly (version 2020_20u1). European Environment Agency. https://doi.org/10.2909/71c95a07-e296-44fc-b22b-415f42acfdf0

Cowan, W.L., 1956. Estimating hydraulic roughness coefficients. Agricultural Engineering, 37(7), 473–475.

Crompton, O., Katul, G., and Thompson, S.E., 2025. Uniting Surface Properties With Hydrodynamic Roughness in Shallow Overland Flow Models. Water Resources Research, 61(1), e2024WR037176. https://doi.org/10.1029/2024WR037176

D'Ippolito, A., Calomino, F., Alfonsi, G., and Lauria, A., 2021. Flow resistance in open channel due to vegetation at reach scale: A review. Water, 13(2), 116. https://doi.org/10.3390/w13020116

Dandois, J.P., and Ellis, E.C., 2010. Remote sensing of vegetation structure using computer vision. Remote Sensing, 2(4), 1157–1176. https://doi.org/10.3390/rs2041157

Dandois, J.P., and Ellis, E.C., 2013. High spatial resolution three-dimensional mapping of vegetation spectral dynamics using computer vision. Remote Sensing of Environment, 136, 259–276. https://doi.org/10.1016/j.rse.2013.04.005

Darabi, H., Haghighi, A.T., Klöve, B., and Luoto, M., 2025. Remote sensing of vegetation trends: A review of methodological choices and sources of uncertainty. Remote Sensing Applications: Society and Environment, 37, 101500. https://doi.org/10.1016/j.rsase.2025.101500

Dash, J.P., Watt, M.S., Pearse, G.D., Heaphy, M., and Dungey, H.S., 2017. Assessing very high resolution UAV imagery for monitoring forest health during a simulated disease outbreak. ISPRS Journal of Photogrammetry and Remote Sensing, 131, 1–14. https://doi.org/10.1016/j.isprsjprs.2017.07.007

Dashpurev, B., Wesche, K., Jäschke, Y., Oyundelger, K., Phan, T.N., Bendix, J., and Lehnert, L.W., 2021. A cost-effective method to monitor vegetation changes in steppes ecosystems: A case study on remote sensing of fire and infrastructure effects in eastern Mongolia. Ecological Indicators, 132, 108331. https://doi.org/10.1016/j.ecolind.2021.108331

Datt, B., 1999. A New Reflectance Index for Remote Sensing of Chlorophyll Content in Higher Plants: Tests using Eucalyptus Leaves. Journal of Plant Physiology, 154(1), 30–36. https://doi.org/10.1016/S0176-1617(99)80314-9

Delegido, J., Verrelst, J., Alonso, L., and Moreno, J., 2011. Evaluation of Sentinel-2 Red-Edge Bands for Empirical Estimation of Green LAI and Chlorophyll Content. Sensors, 11(7), 7063–7081. https://doi.org/10.3390/s110707063

Deltares, 2020. D-Flow Flexible Mesh User Manual. Delft: Deltares.

Deltares, 2024. Delft3D FM Suite 1D2D: User Manual D-Flow Flexible Mesh. Delft: Deltares.

Deltares, 2025. Delft3D FM Suite: Simulation software for safe, sustainable and future deltas – User Manual D-Flow Flexible Mesh. Delft: Deltares.

Deng, X., Hu, X., Shi, L., Su, C., Li, J., Du, S., and Li, S., 2024. Deep learning-enabled exploration of global spectral features for photosynthetic capacity estimation. Frontiers in Plant Science, 15, 1499875. https://doi.org/10.3389/fpls.2024.1499875

DJI, 2022. DJI Mavic 3 Multispectral User Manual, Version 1.0. Shenzhen: DJI.

DJI, 2024. DJI Terra User Manual, Version 4.3. Shenzhen: DJI.

Dottori, F., Szewczyk, W., Ciscar, J.C., Zhao, F., Alfieri, L., Hirabayashi, Y., Bianchi, A., Mongelli, I., Frieler, K., Betts, R.A., and Feyen, L., 2018. Increased human and economic losses from river flooding with anthropogenic warming. Nature Climate Change, 8(9), 781–786. https://doi.org/10.1038/s41558-018-0257-z

Drusch, M., Del Bello, U., Carlier, S., Colin, O., Fernandez, V., Gascon, F., Hoersch, B., Isola, C., Laberinti, P., Martimort, P., Meygret, A., Spoto, F., Sy, O., Marchese, F., and Bargellini, P., 2012. Sentinel-2: ESA's Optical High-Resolution Mission for GMES Operational Services. Remote Sensing of Environment, 120, 25–36. https://doi.org/10.1016/j.rse.2011.11.026

Duc, L., and Sawada, Y., 2023. A signal-processing-based interpretation of the Nash–Sutcliffe efficiency. Hydrology and Earth System Sciences, 27(9), 1827–1839. https://doi.org/10.5194/hess-27-1827-2023

Eltner, A., Kaiser, A., Castillo, C., Rock, G., Neugirg, F. and Abellán, A., 2016. Image-based surface reconstruction in geomorphometry – merits, limits and developments. Earth Surface Dynamics, 4, pp.359–389. https://doi.org/10.5194/esurf-4-359-2016

Farwell, L.S., Gudex-Cross, D., Anise, I.E., Bosch, M.J., Olah, A.M., Radeloff, V.C., Razenkova, E., Rogova, N., Silveira, E.M.O., Smith, M.M., and Pidgeon, A.M., 2021. Satellite image texture captures vegetation heterogeneity and explains patterns of bird richness. Remote Sensing of Environment, 253, 112175. https://doi.org/10.1016/j.rse.2020.112175

Feldmann, D., Laux, P., Heckl, A., Schindler, M., and Kunstmann, H., 2023. Near surface roughness estimation: A parameterization derived from artificial rainfall experiments and two-dimensional hydrodynamic modelling for multiple vegetation coverages. Journal of Hydrology, 617, 128786. https://doi.org/10.1016/j.jhydrol.2022.128786

Feng, D.Q., Fan, J.J., Wang, W.J., Xia, C.X., and Li, A., 2024. New formula of vegetation roughness height and Darcy–Weisbach friction factor in channel flow. Journal of Hydrology, 636, 131278. https://doi.org/10.1016/j.jhydrol.2024.131278

Ferguson, R., 2007. Flow resistance equations for gravel- and boulder-bed streams. Water Resources Research, 43(5), W05427. https://doi.org/10.1029/2006WR005422

Ferraz, M.A.J., Barboza, T.O.C., Arantes, P.S., Pinho, R.G., and Santos, A.F., 2024. Integrating Satellite and UAV Technologies for Maize Plant Height Estimation Using Advanced Machine Learning. AgriEngineering, 6(1), 20–33.

https://doi.org/10.3390/agriengineering6010002
Ferreira, D.M., Fernandes, C.V.S., Kaviski, E., and Bleninger, T., 2021. Calibration of river hydrodynamic models: Analysis from the dynamic component in roughness coefficients. Journal of Hydrology, 598, 126136. https://doi.org/10.1016/j.jhydrol.2021.126136
Ferziger, J.H., and Perić, M., 2002. Computational Methods for Fluid Dynamics. 3rd ed. Berlin, Heidelberg: Springer. https://doi.org/10.1007/978-3-642-56026-2
Fleischmann, A.S., Paiva, R.C.D., Collischonn, W., Siqueira, V.A., Paris, A., Moreira, D.M., Papa, F., Bitar, A.A., Parrens, M., Aires, F., and Garambois, P.A., 2020. Trade-Offs Between 1-D and 2-D Regional River Hydrodynamic Models. Water Resources Research, 56(8), e2019WR026812. https://doi.org/10.1029/2019WR026812
Fortes, A.A., Hashimoto, M., Udo, K., and Ichikawa, K., 2024. Satellite and UAV derived seasonal vegetative roughness estimation for flood analysis. Proceedings of the International Association of Hydrological Sciences, 392, 203–208. https://doi.org/10.5194/piahs-392-203-2024
Forzieri, G., Degetto, M., Righetti, M., Castelli, F., and Preti, F., 2011. Satellite multispectral data for improved floodplain roughness modelling. Journal of Hydrology, 407(1–4), 41–57. https://doi.org/10.1016/j.jhydrol.2011.07.009
Francis, R.J., Kingsford, R.T., Moseby, K., Read, J., Pedler, R., Fisher, A., McCann, J., and West, R., 2024. Tracking landscape scale vegetation change in the arid zone by integrating ground, drone and satellite data. Remote Sensing in Ecology and Conservation, 10(3), 374–387. https://doi.org/10.1002/rse2.375
Fu, D., Xiao, H., Su, F., Zhou, C., Dong, J., Zeng, Y., Yan, K., Li, S., Wu, J., Wu, W., and Yan, F., 2021. Remote sensing cloud computing platform development and Earth science application. National Remote Sensing Bulletin, 25(1), 220–230. https://doi.org/10.11834/jrs.20210447
Gascon, F., Bouzinac, C., Thépaut, O., Jung, M., Francesconi, B., Louis, J., Lonjou, V., Lafrance, B., Massera, S., Gaudel-Vacaresse, A., Languille, F., Alhammoud, B., Viallefont, F., Pflug, B., Bieniarz, J., Clerc, S., Pessiot, L., Trémas, T., Cadau, E., and Fernandez, V., 2017. Copernicus Sentinel-2A Calibration and Products Validation Status. Remote Sensing, 9(6), 584. https://doi.org/10.3390/rs9060584
Georganos, S., Grippa, T., Vanhuysse, S., Lennert, M., Shimoni, M., and Wolff, E., 2018. Very High Resolution Object-Based Land Use-Land Cover Urban Classification Using Extreme Gradient Boosting. IEEE Geoscience and Remote Sensing Letters, 15(4), 607–611. https://doi.org/10.1109/LGRS.2018.2803259
Geurts, P., Ernst, D., and Wehenkel, L., 2006. Extremely randomized trees. Machine Learning, 63(1), 3–42. https://doi.org/10.1007/s10994-006-6226-1
Gitelson, A.A., 2004. Wide Dynamic Range Vegetation Index for Remote Quantification of Biophysical Characteristics of Vegetation. Journal of Plant Physiology, 161(2), 165–173. https://doi.org/10.1078/0176-1617-01176
Gitelson, A.A., Kaufman, Y.J., and Merzlyak, M.N., 1996. Use of a green channel in

remote sensing of global vegetation from EOS-MODIS. Remote Sensing of Environment, 58(3), 289–298. https://doi.org/10.1016/S0034-4257(96)00072-7

Gitelson, A.A., Viña, A., Ciganda, V., Rundquist, D.C., and Arkebauer, T.J., 2005. Remote estimation of canopy chlorophyll content in crops. Geophysical Research Letters, 32(8), L08403. https://doi.org/10.1029/2005GL022688

Glenn, E.P., Huete, A.R., Nagler, P.L., and Nelson, S.G., 2008. Relationship Between Remotely-sensed Vegetation Indices, Canopy Attributes and Plant Physiological Processes: What Vegetation Indices Can and Cannot Tell Us About the Landscape. Sensors, 8(4), 2136–2160. https://doi.org/10.3390/s8042136

Glock, K., Tritthart, M., Habersack, H., and Hauer, C., 2019. Comparison of hydrodynamics simulated by 1D, 2D and 3D models focusing on bed shear stresses. Water, 11(2), 226. https://doi.org/10.3390/w11020226

Goldsmith, W., Bernardi, D., and Schippa, L., 2015. River, delta and coastal morphological response accounting for biological dynamics. Proceedings of the International Association of Hydrological Sciences, 367, 413–420. https://doi.org/10.5194/piahs-367-413-2015

Gómez, V.H., Franco, L.R., Ravazzani, G., Passoni, G., and Mancini, M., 2024. Modeling arboreal vegetation-induced friction and its influence on river flooding using a two-dimensional model. Environmental Fluid Mechanics, 24(3), 387–411. https://doi.org/10.1007/s10652-024-09991-z

Gorelick, N., Hancher, M., Dixon, M., Ilyushchenko, S., Thau, D., and Moore, R., 2017. Google Earth Engine: Planetary-scale geospatial analysis for everyone. Remote Sensing of Environment, 202, 18–27. https://doi.org/10.1016/j.rse.2017.06.031

Górnik, M., 2020. Changing trends of river flows in the Upper Vistula Basin (East-Central Europe). Acta Geophysica, 68(2), 495–504. https://doi.org/10.1007/s11600-020-00400-9

Green, J.C., 2005. Modelling flow resistance in vegetated streams: Review and development of new theory. Hydrological Processes, 19(6), 1245–1259. https://doi.org/10.1002/hyp.5564

Guo, Y., Ding, W., Xu, W., Zhu, X., Wang, X., and Tang, W., 2022. Assessment of an Alternative Climate Product for Hydrological Modeling: A Case Study of the Danjiang River Basin, China. Water, 14(7), 1105. https://doi.org/10.3390/w14071105

Guo, Y., Nones, M., Zhou, Y., Zhu, R., and Ding, W., 2025. Combination of UAV Imagery and Deep Learning to Estimate Vegetation Height over Fluvial Sandbars. Water, 17(21), 3160. https://doi.org/10.3390/w17213160

Gupta, H.V., Sorooshian, S., and Yapo, P.O., 1999. Status of Automatic Calibration for Hydrologic Models: Comparison with Multilevel Expert Calibration. Journal of Hydrologic Engineering, 4(2), 135–143. https://doi.org/10.1061/(ASCE)1084-0699(1999)4:2(135)

Halecki, W., and Młyński, D., 2025. Urban flood dilemmas: How European cities growth shapes flood risk and resilience strategies? Journal of Environmental

Management, 374, 124161. https://doi.org/10.1016/j.jenvman.2025.124161

Hamidifar, H., Nones, M., and Rowiński, P.M., 2026. Morphodynamic Feedback on Flood Hydraulics in Alluvial River Systems: The Polish Middle Vistula River Case. River Research and Applications, 42(1), 212–223. https://doi.org/10.1002/rra.70059

Hanif, C.M., and Barber, M.E., 2016. Open channel flow. In: Johnson, R.W. (ed.), Handbook of Fluid Dynamics. 2nd ed. Boca Raton: CRC Press, 16.1–16.25. https://doi.org/10.4324/9781003170181-29

Hengl, T., Nussbaum, M., Wright, M.N., Heuvelink, G.B.M., and Gräler, B., 2018. Random forest as a generic framework for predictive modeling of spatial and spatio-temporal variables. PeerJ, 6, e5518. https://doi.org/10.7717/peerj.5518

Hiederer, R., 2013. Mapping Soil Properties for Europe – Spatial Representation of Soil Database Attributes. Luxembourg: Publications Office of the European Union, EUR26082EN. https://doi.org/10.2788/94128

Hoch, J.M., van Beek, R., Winsemius, H.C., and Bierkens, M.F.P., 2018. Benchmarking flexible meshes and regular grids for large-scale fluvial inundation modelling. Advances in Water Resources, 121, 350–360. https://doi.org/10.1016/j.advwatres.2018.09.003

Hodges, B.R., 2019. Conservative finite-volume forms of the Saint-Venant equations for hydrology and urban drainage. Hydrology and Earth System Sciences, 23(3), 1281–1304. https://doi.org/10.5194/hess-23-1281-2019

Horritt, M.S., and Bates, P.D., 2001. Predicting floodplain inundation: Raster-based modelling versus the finite-element approach. Hydrological Processes, 15(5), 825–842. https://doi.org/10.1002/hyp.188

Horritt, M.S., and Bates, P.D., 2002. Evaluation of 1D and 2D numerical models for predicting river flood inundation. Journal of Hydrology, 268(1–4), 87–99. https://doi.org/10.1016/S0022-1694(02)00121-X

Hosseini, S.M., and Coonrod, J., 2011. Coupling Numerical and Physical Modeling for Analysis of Flow in a Diversion Structure with Coanda-effect Screens. Water, 3(3), 764–786. https://doi.org/10.3390/w3030764

Hou, L.F., Li, L., Chen, R., Wu, Y.P., Feng, G.L., and Sun, G.Q., 2025. Vegetation dynamics: Modeling, mechanisms, and emergent properties. Physics Reports, 1145, 1–87. https://doi.org/10.1016/j.physrep.2025.09.003

Hsu, Y.L., Dykes, J.D., Allard, R.A., and Kaihatu, J.M., 2006. Evaluation of Delft3D performance in nearshore flows. Technical Report, Texas A&M University, College Station, TX, USA.

Huete, A., Didan, K., Miura, T., Rodriguez, E.P., Gao, X., and Ferreira, L.G., 2002. Overview of the radiometric and biophysical performance of the MODIS vegetation indices. Remote Sensing of Environment, 83(1–2), 195–213. https://doi.org/10.1016/S0034-4257(02)00096-2

Huthoff, F., Augustijn, D.C.M., and Hulscher, S.J.M.H., 2007. Analytical solution of the depth-averaged flow velocity in case of submerged rigid cylindrical vegetation. Water Resources Research, 43(6), W06513. https://doi.org/10.1029/2006WR005625

Ibrahim, S., Balzter, H., and Tansey, K., 2024. Machine learning feature importance selection for predicting aboveground biomass in African savannah with landsat 8 and ALOS PALSAR data. Machine Learning with Applications, 16, 100561. https://doi.org/10.1016/j.mlwa.2024.100561

Immitzer, M., Vuolo, F., and Atzberger, C., 2016. First Experience with Sentinel-2 Data for Crop and Tree Species Classifications in Central Europe. Remote Sensing, 8(3), 166. https://doi.org/10.3390/rs8030166

James, C.S., Birkhead, A.L., Jordanova, A.A., and O'Sullivan, J.J., 2004. Flow resistance of emergent vegetation. Journal of Hydraulic Research, 42(4), 390–398. https://doi.org/10.1080/00221686.2004.9728404

James, G., Witten, D., Hastie, T., and Tibshirani, R., 2021. An Introduction to Statistical Learning with Applications in R. 2nd ed. New York: Springer. https://doi.org/10.1007/978-1-0716-1418-1

James, M.R. and Robson, S., 2012. Straightforward reconstruction of 3D surfaces and topography with a camera: Accuracy and geoscience application. Journal of Geophysical Research: Earth Surface, 117(F3), F03017. https://doi.org/10.1029/2011JF002289

Järvelä, J., 2002. Flow resistance of flexible and stiff vegetation: A flume study with natural plants. Journal of Hydrology, 269(1–2), 44–54. https://doi.org/10.1016/S0022-1694(02)00193-2

Järvelä, J., 2004. Determination of flow resistance caused by non-submerged woody vegetation. International Journal of River Basin Management, 2(1), 61-70. https://doi.org/10.1080/15715124.2004.9635222

Järvelä, J., 2005. Effect of submerged flexible vegetation on flow structure and resistance. Journal of Hydrology, 307(1–4), 233–241. https://doi.org/10.1016/j.jhydrol.2004.10.013

Jiang, L., Westphal Christensen, S., and Bauer-Gottwein, P., 2021. Calibrating 1D hydrodynamic river models in the absence of cross-section geometry using satellite observations of water surface elevation and river width. Hydrology and Earth System Sciences, 25(12), 6359–6379. https://doi.org/10.5194/hess-25-6359-2021

Kernkamp, H.W.J., Van Dam, A., Stelling, G.S., and De Goede, E.D., 2011. Efficient scheme for the shallow water equations on unstructured grids with application to the Continental Shelf. Ocean Dynamics, 61(8), 1175–1188. https://doi.org/10.1007/s10236-011-0423-6

Keupers, I., Nguyen Thanh, T., and Willems, P., 2015. Modelling the time variance of the river bed roughness coefficient for improved simulation of water levels. International Journal of River Basin Management, 13(2), 167–178. https://doi.org/10.1080/15715124.2014.999782

Kiczko, A., Romanowicz, R.J., Osuch, M., and Karamuz, E., 2013. Maximising the usefulness of flood risk assessment for the river Vistula in Warsaw. Natural Hazards and Earth System Sciences, 13(12), 3443–3455. https://doi.org/10.5194/nhess-13-3443-2013

Klemeš, V., 1986. Operational testing of hydrological simulation models. Hydrological Sciences Journal, 31(1), 13–24. https://doi.org/10.1080/02626668609491024

Kohavi, R., 1995. A Study of Cross-Validation and Bootstrap for Accuracy Estimation and Model Selection. In: Proceedings of the 14th International Joint Conference on Artificial Intelligence (IJCAI), 1137–1143.

Kordowski, J., 2009. On the lower Vistula valley development in the light of geomorphological and sedimentological investigations. Polish Geological Institute Special Papers, 25, 21–36.

Kouwen, N., and Unny, T.E., 1973. Flexible roughness in open channels. Journal of the Hydraulics Division, 99(5), 713–728.

Krasiewicz, D.W., and Wierzbicki, G., 2023. Flood Perception from Local Perspective of Rural Community vs. Geomorphological Control of Fluvial Processes in Large Alluvial Valley (the Middle Vistula River, Poland). Hydrology, 10(10), 191. https://doi.org/10.3390/hydrology10100191

Kryniecka, K., Magnuszewski, A., and Radecki-Pawlik, A., 2022. Sentinel-1 Satellite Radar Images: A New Source of Information for Study of River Channel Dynamics on the Lower Vistula River, Poland. Remote Sensing, 14(5), 1056. https://doi.org/10.3390/rs14051056

Kubiak-Wójcicka, K., 2020. Variability of Air Temperature, Precipitation and Outflows in the Vistula Basin (Poland). Resources, 9(9), 103. https://doi.org/10.3390/resources9090103

Kubiak-Wójcicka, K., Pilarska, A., and Kamiński, D., 2024. Meteorological drought in the upper Noteć catchment area (Central Poland) in the light of NDVI and SPI indicators. Applied Water Science, 14(8), 180. https://doi.org/10.1007/s13201-024-02215-1

Kuhn, M., and Johnson, K., 2013. Applied Predictive Modeling. New York: Springer. https://doi.org/10.1007/978-1-4614-6849-3

Kuurasuo, J., 2025. Towards the Development of a Reflectance Estimation Pipeline for Multispectral and RGB Drone Imagery. Master's thesis, University of Helsinki.

Kvålseth, T.O., 1985. Cautionary note about R^2. The American Statistician, 39(4), 279–285. https://doi.org/10.1080/00031305.1985.10479448

Łajczak, A., Babiński, Z., Falkowski, T., Gierszewski, P., Habel, M., Plit, J., Soja, R., and Szmańda, J., 2021. Współczesne przemiany rzeźby koryta i równiny zalewowej Wisły. In: Współczesne przemiany rzeźby Polski. Kraków: Instytut Geografii i Gospodarki Przestrzennej UJ, 145–178.

Lane, S.N., Hardy, R.J., Elliot, L., and Ingham, D.B., 2004. Numerical modeling of flow processes over gravelly surfaces using structured grids and a numerical porosity treatment. Water Resources Research, 40(1), W01302.

https://doi.org/10.1029/2002WR001934
Lang, N., Jetz, W., Schindler, K., and Wegner, J.D., 2023. A high-resolution canopy height model of the Earth. Nature Ecology & Evolution, 7(11), 1778–1789. https://doi.org/10.1038/s41559-023-02206-6
Le Piane, F., Vozza, M., Baldoni, M., and Mercuri, F., 2024. Integrating high-performance computing, machine learning, data management workflows, and infrastructures for multiscale simulations and nanomaterials technologies. Beilstein Journal of Nanotechnology, 15, 1498–1515. https://doi.org/10.3762/bjnano.15.119
Lee, W., Sun, A.Y., Scanlon, B.R., and Dawson, C., 2024. Hindcasting compound pluvial, fluvial and coastal flooding during Hurricane Harvey (2017) using Delft3D-FM. Natural Hazards, 120(1), 851–880. https://doi.org/10.1007/s11069-023-06247-9
Lefsky, M.A., Cohen, W.B., Parker, G.G., and Harding, D.J., 2002. Lidar remote sensing for ecosystem studies. BioScience, 52(1), 19–30. https://doi.org/10.1641/0006-3568(2002)052[0019:LRSFES]2.0.CO;2
Legates, D.R., and McCabe, G.J., 1999. Evaluating the use of "goodness-of-fit" measures in hydrologic and hydroclimatic model validation. Water Resources Research, 35(1), 233–241. https://doi.org/10.1029/1998WR900018
Lesser, G.R., Roelvink, J.A., van Kester, J.A.T.M., and Stelling, G.S., 2004. Development and validation of a three-dimensional morphological model. Coastal Engineering, 51(8–9), 883–915. https://doi.org/10.1016/j.coastaleng.2004.07.014
Li, H., Yin, J., and Jiao, L., 2024. An Improved 3D Reconstruction Method for Satellite Images Based on Generative Adversarial Network Image Enhancement. Applied Sciences, 14(16), 7177. https://doi.org/10.3390/app14167177
Linjordet, T., and Balog, K., 2019. Impact of Training Dataset Size on Neural Answer Selection Models. In: Lecture Notes in Computer Science, vol. 11437, 828–835. https://doi.org/10.1007/978-3-030-15712-8_59
Liu, C., Liu, Y., Lu, Y., Liao, Y., Nie, J., Yuan, X., and Chen, F., 2019. Use of a leaf chlorophyll content index to improve the prediction of above-ground biomass and productivity. PeerJ, 7, e6240. https://doi.org/10.7717/peerj.6240
Łoboda, A.M., Przyborowski, Karpiński, M., Bialik, R.J., and Nikora, V.I., 2018. Biomechanical properties of aquatic plants: The effect of test conditions. Limnology and Oceanography: Methods, 16(4), 222–236. https://doi.org/10.1002/lom3.10239
López-Ramade, E., Mulligan, R.P., Medellín, G., and Torres-Freyermuth, A., 2023. Modelling beach morphological responses near coastal structures under oblique waves driven by sea-breezes. Coastal Engineering, 182, 104290. https://doi.org/10.1016/j.coastaleng.2023.104290
Lourenço, P., Godinho, S., Sousa, A., and Gonçalves, A.C., 2021. Estimating tree aboveground biomass using multispectral satellite-based data in Mediterranean

agroforestry system using random forest algorithm. Remote Sensing Applications: Society and Environment, 23, 100560. https://doi.org/10.1016/j.rsase.2021.100560

Lu, B., and He, Y., 2017. Species classification using Unmanned Aerial Vehicle (UAV)-acquired high spatial resolution imagery in a heterogeneous grassland. ISPRS Journal of Photogrammetry and Remote Sensing, 128, 73–85. https://doi.org/10.1016/j.isprsjprs.2017.03.011

Luhar, M., and Nepf, H.M., 2013. From the blade scale to the reach scale: A characterization of aquatic vegetative drag. Advances in Water Resources, 51, 305–316. https://doi.org/10.1016/j.advwatres.2012.02.002

Main, R., Cho, M.A., Mathieu, R., O'Kennedy, M.M., Ramoelo, A., and Koch, S., 2011. An investigation into robust spectral indices for leaf chlorophyll estimation. ISPRS Journal of Photogrammetry and Remote Sensing, 66(6), 751–761. https://doi.org/10.1016/j.isprsjprs.2011.08.001

Matyukira, C., and Mhangara, P., 2024. Advances in vegetation mapping through remote sensing and machine learning techniques: a scientometric review. European Journal of Remote Sensing, 57(1), 2422330. https://doi.org/10.1080/22797254.2024.2422330

Maxwell, A.E., Warner, T.A., and Fang, F., 2018. Implementation of machine-learning classification in remote sensing: An applied review. International Journal of Remote Sensing, 39(9), 2784–2817. https://doi.org/10.1080/01431161.2018.1433343

McCuen, R.H., Knight, Z., and Cutter, A.G., 2006. Evaluation of the Nash–Sutcliffe Efficiency Index. Journal of Hydrologic Engineering, 11(6), 597–602. https://doi.org/10.1061/(ASCE)1084-0699(2006)11:6(597)

Mentch, L., and Hooker, G., 2016. Quantifying uncertainty in random forests via confidence intervals and hypothesis tests. Journal of Machine Learning Research, 17, 1–41.

Mewis, P., 2021. Estimation of Vegetation-Induced Flow Resistance for Hydraulic Computations Using Airborne Laser Scanning Data. Water, 13(13), 1864. https://doi.org/10.3390/w13131864

Meyer, H., Reudenbach, C., Wöllauer, S., and Nauss, T., 2019. Importance of spatial predictor variable selection in machine learning applications – Moving from data reproduction to spatial prediction. Ecological Modelling, 411, 108815. https://doi.org/10.1016/j.ecolmodel.2019.108815

Montanari, A., 2012. Hydrology of the Po River: Looking for changing patterns in river discharge. Hydrology and Earth System Sciences, 16(10), 3739–3747. https://doi.org/10.5194/hess-16-3739-2012

Moriasi, D.N., Arnold, J.G., Van Liew, M.W., Bingner, R.L., Harmel, R.D., and Veith, T.L., 2007. Model evaluation guidelines for systematic quantification of accuracy in watershed simulations. Transactions of the ASABE, 50(3), 885–900.

Morvan, H., Knight, D., Wright, N., Tang, X., and Crossley, A., 2008. The concept of roughness in fluvial hydraulics and its formulation in 1D, 2D and 3D numerical simulation models. Journal of Hydraulic Research, 46(2), 191–208. https://doi.org/10.1080/00221686.2008.9521855

Mutanga, O., and Skidmore, A.K., 2004. Narrow band vegetation indices overcome the saturation problem in biomass estimation. International Journal of Remote Sensing, 25(19), 3999–4014. https://doi.org/10.1080/01431160310001654923

Nagler, P., Glenn, E.P., Hursh, K., Curtis, C., and Huete, A., 2005. Vegetation Mapping for Change Detection on an Arid-Zone River. Environmental Monitoring and Assessment, 109(1), 255–274. https://doi.org/10.1007/s10661-005-6285-y

Naiman, R.J., Décamps, H., McClain, M.E., and Likens, G.E., 2005. Riparia: Ecology, conservation, and management of streamside communities. Burlington: Academic Press. https://doi.org/10.1016/B978-0-12-663315-3.X5000-X

Nasiri, V., Hawryło, P., Tompalski, P., Wertz, B., and Socha, J., 2025. Linking remotely sensed growth-related canopy attributes to interannual tree-ring width variations: A species-specific study using Sentinel optical and SAR time series. ISPRS Journal of Photogrammetry and Remote Sensing, 221, 347–362. https://doi.org/10.1016/j.isprsjprs.2025.02.002

Neal, J.C., Odoni, N.A., Trigg, M.A., Freer, J.E., Garcia-Pintado, J., Mason, D.C., Wood, M., and Bates, P.D., 2015. Efficient incorporation of channel cross-section geometry uncertainty into regional and global scale flood inundation models. Journal of Hydrology, 529, 169–183. https://doi.org/10.1016/j.jhydrol.2015.07.026

Neal, J., Schumann, G., and Bates, P., 2012. A subgrid channel model for simulating river hydraulics and floodplain inundation over large and data sparse areas. Water Resources Research, 48(11), W11506. https://doi.org/10.1029/2012WR012514

Nepf, H.M., 1999. Drag, turbulence, and diffusion in flow through emergent vegetation. Water Resources Research, 35(2), 479–489. https://doi.org/10.1029/1998WR900069

Nepf, H.M., 2012a. Flow and transport in regions with aquatic vegetation. Annual Review of Fluid Mechanics, 44, 123–142. https://doi.org/10.1146/annurev-fluid-120710-101048

Nepf, H.M., 2012b. Hydrodynamics of vegetated channels. Journal of Hydraulic Research, 50(3), 262–279. https://doi.org/10.1080/00221686.2012.696559

Neufeld, A.C., Gao, L.L., and Witten, D.M., 2022. Tree-Values: Selective Inference for Regression Trees. Journal of Machine Learning Research, 23, 1–43.

Nicosia, A., and Ferro, V., 2023. Flow resistance due to shrubs and woody vegetation. Flow Measurement and Instrumentation, 89, 102308. https://doi.org/10.1016/j.flowmeasinst.2023.102308

Nikora, V., Goring, D., McEwan, I., and Griffiths, G., 2001. Spatially Averaged Open-Channel Flow over Rough Bed. Journal of Hydraulic Engineering, 127(2), 123–133. https://doi.org/10.1061/(ASCE)0733-9429(2001)127:2(123)

Nikora, V., Larned, S., Nikora, N., Debnath, K., Cooper, G., and Reid, M., 2008.

Hydraulic Resistance due to Aquatic Vegetation in Small Streams: Field Study. Journal of Hydraulic Engineering, 134(9), 1326–1332. https://doi.org/10.1061/(ASCE)0733-9429(2008)134:9(1326)

Nițu, A., Florea, C., Ivanovici, M., and Racoviteanu, A., 2025. NDVI and Beyond: Vegetation Indices as Features for Crop Recognition and Segmentation in Hyperspectral Data. Sensors, 25(12), 3817. https://doi.org/10.3390/s25123817

Niu, C., Hu, C., Li, M., Zhao, L., Xie, T., Li, W., Wen, K., and Dou, S., 2025. The influence of roughness in the floodplain of the lower yellow river on water depth and flow velocity of overbank floods. Journal of Hydrology: Regional Studies, 59, 102422. https://doi.org/10.1016/j.ejrh.2025.102422

Nones, M., 2019. Numerical modelling as a support tool for river habitat studies: An Italian case study. Water, 11(3), 482. https://doi.org/10.3390/w11030482

Nones, M., and Guo, Y., 2026. Prolonged Dry Periods Associated with Riparian Vegetation Growth and Channel Simplification. Hydrology, 13(1), 21. https://doi.org/10.3390/hydrology13010021

Nones, M., Maselli, V., and Varrani, A., 2020. Numerical modeling of the hydro-morphodynamics of a distributary channel of the Po River delta (Italy) during the spring 2009 flood event. Geosciences, 10(6), 209. https://doi.org/10.3390/geosciences10060209

Noviana, R., and Sela, E.I., 2024. Performance Comparison Random Forest and Logistic Regression in Predicting Time Deposit Customers with Feature Selection. International Journal of Computer Applications, 186(16), 15–22. https://doi.org/10.5120/ijca2024923654

Onyutha, C., 2020. From R-squared to coefficient of model accuracy for assessing “goodness-of-fits”. Geoscientific Model Development Discussions, 1–25. https://doi.org/10.5194/gmd-2020-51

Pace, G., Gutiérrez-Cánovas, T., Henriques, R., Boeing, F., Cássio, F., and Pascoal, C., 2022. Remote sensing indicators to assess riparian vegetation and river ecosystem health. Ecological Indicators, 144, 109519. https://doi.org/10.1016/j.ecolind.2022.109519

Pan, W., Wang, X., Sun, Y., Wang, J., Li, Y., and Li, S., 2023. Karst vegetation coverage detection using UAV multispectral vegetation indices and machine learning algorithm. Plant Methods, 19(1), 7. https://doi.org/10.1186/s13007-023-00982-7

Pandit, A., Hogan, S., Mahoney, D.T., Ford, W.I., Fox, J.F., Wellen, C., and Husic, A., 2025. Establishing performance criteria for evaluating watershed-scale sediment and nutrient models at fine temporal scales. Water Research, 274, 123156. https://doi.org/10.1016/j.watres.2025.123156

Pappenberger, F., Beven, K., Horritt, M., and Blazkova, S., 2005. Uncertainty in the calibration of effective roughness parameters in HEC-RAS using inundation and downstream level observations. Journal of Hydrology, 302(1–4), 46–69. https://doi.org/10.1016/j.jhydrol.2004.06.036

Paprotny, D., Terefenko, P., and Śledziowski, J., 2024. HANZE database of historical flood impacts in Europe, 1870-2020. Scientific Data, 11, 493. https://doi.org/10.1038/s41597-024-03352-3

Pasma, G.R., Suharyanto, H.H.R., Khoirunnisa, H., Wijayanti, R., Gumbira, G., and Rachman, R.A., 2024. Assessment of Sensitivity and Validity Hydrodynamic Model in Cisadane Using Delft3D Flow Model. ILMU KELAUTAN: Indonesian Journal of Marine Sciences, 29(1), 133–146. https://doi.org/10.14710/ik.ijms.29.1.133-146

Pelletier, C., Valero, S., Inglada, J., Champion, N., and Dedieu, G., 2016. Assessing the robustness of Random Forests to map land cover with high resolution satellite image time series over large areas. Remote Sensing of Environment, 187, 156–168. https://doi.org/10.1016/j.rse.2016.10.010

Penna, N., Coscarella, F., D'Ippolito, A., and Gaudio, R., 2020. Bed Roughness Effects on the Turbulence Characteristics of Flows through Emergent Rigid Vegetation. Water, 12(9), 2401. https://doi.org/10.3390/w12092401

Petryk, S., and Bosmajian, G., 1975. Analysis of flow through vegetation. Journal of the Hydraulics Division, 101(7), 871–884. https://doi.org/10.1061/JYCEAJ.0004397

Pietras, B., and Pyrc, R., 2025. Extreme Short-Duration Rainfall and Urban Flood Hazard: Case Studies of Convective Events in Warsaw and Zamość, Poland. Water, 17(18), 2671. https://doi.org/10.3390/w17182671

Piniewski, M., Szcześniak, M., Kardel, I., Berezowski, T., Okruszko, T., Srinivasan, R., Vikhamar Schuler, D., and Kundzewicz, Z.W., 2017. Hydrological modelling of the Vistula and Odra river basins using SWAT. Hydrological Sciences Journal, 62(8), 1266–1289. https://doi.org/10.1080/02626667.2017.1321842

Poggi, D., Porporato, A., Ridolfi, L., Albertson, J.D., and Katul, G.G., 2004. The effect of vegetation density on canopy sub-layer turbulence. Boundary-Layer Meteorology, 111(3), 565–587. https://doi.org/10.1023/B:BOUN.0000016576.05621.73

Potapov, P., Li, X., Hernandez-Serna, A., Tyukavina, A., Hansen, M.C., Kommareddy, A., Pickens, A., Turubanova, S., Tang, H., Silva, C.E., Armston, J., Dubayah, R., Blair, J.B., and Hofton, M., 2021. Mapping global forest canopy height through integration of GEDI and Landsat data. Remote Sensing of Environment, 253, 112165. https://doi.org/10.1016/j.rse.2020.112165

Prior, E.M., Aquilina, C.A., Czuba, J.A., Pingel, T.J., and Hession, W.C., 2021. Estimating floodplain vegetative roughness using drone-based laser scanning and structure from motion photogrammetry. Remote Sensing, 13(13), 2616. https://doi.org/10.3390/rs13132616

Przyborowski, Ł., Łoboda, A.M., Karpiński, M., and Bialik, R.J., 2018. Characteristics of flow around aquatic plants in natural conditions: Experimental setup, challenges and difficulties. GeoPlanet: Earth and Planetary Sciences, 347–361. https://doi.org/10.1007/978-3-319-70914-7_23

Quinlan, J.R., 1992. Learning with continuous classes. In: Proceedings of the 5th

Australian Joint Conference on Artificial Intelligence, 343–348.
Radeloff, V.C., Roy, D.P., Wulder, M.A., Anderson, M., Cook, B., Crawford, C.J., Friedl, M., Gao, F., Gorelick, N., Hansen, M., Healey, S., Hostert, P., Hulley, G., Huntington, J.L., Johnson, D.M., Neigh, C., Lyapustin, A., Lymburner, L., Pahlevan, N., Pekel, J.F., Scambos, T.A., Schaaf, C., Strobl, P., Woodcock, C.E., Zhang, H.K., and Zhu, Z., 2024. Need and vision for global medium-resolution Landsat and Sentinel-2 data products. Remote Sensing of Environment, 300, 113918. https://doi.org/10.1016/j.rse.2023.113918
Radke, D., and Radke, J., 2020. Beyond Measurement: Extracting Vegetation Height from High Resolution Imagery with Deep Learning. Remote Sensing, 12(22), 3797. https://doi.org/10.3390/rs12223797
Rahmani, F., and Fattahi, M.H., 2023. Investigation of alterations in droughts and floods patterns induced by climate change. Acta Geophysica, 72(1), 405–418. https://doi.org/10.1007/s11600-023-01043-2
Räike, A., Svendsen, L.M., Haapaniemi, J., Larsen, S.E., Oblomkova, N., Frank-Kamenetsky, D., Bojanowski, D., Brynska, W., Ennet, P., Gustafsson, B., Koch, D., Kokorite, I., Mönnich, J., Plunge, S., Pohl, M., and Sonesten, L., 2018. Input of nutrients by the seven biggest rivers in the Baltic Sea region. Baltic Sea Environment Proceedings, 163, 1–25.
Rajendiran, S., Balaji, R., and Rishi, D.S., 2025. Performance evaluation and comparison of Delft3DFM and TUFLOW FV for urban flood simulation along Tapi River, India. Modeling Earth Systems and Environment, 11(4), 278. https://doi.org/10.1007/s40808-025-02453-5
Refsgaard, J.C., and Henriksen, H.J., 2004. Modelling guidelines—terminology and guiding principles. Advances in Water Resources, 27(1), 71–82. https://doi.org/10.1016/j.advwatres.2003.08.006
Reichstein, M., Camps-Valls, G., Stevens, B., Jung, M., Denzler, J., Carvalhais, N., and Prabhat, 2019. Deep learning and process understanding for data-driven Earth system science. Nature, 566(7743), 195–204. https://doi.org/10.1038/s41586-019-0912-1
Reinke, K., and Jones, S., 2006. Integrating vegetation field surveys with remotely sensed data. Ecological Management and Restoration, 7(S1), S18–S23. https://doi.org/10.1111/j.1442-8903.2006.00287.x
Roelvink, D., Reniers, A., van Dongeren, A., van Thiel de Vries, J., McCall, R., and Lescinski, J., 2009. Modelling storm impacts on beaches, dunes and barrier islands. Coastal Engineering, 56(11–12), 1133–1152. https://doi.org/10.1016/j.coastaleng.2009.08.006
Rogers, C.W., Smartt, A.D., Brye, K.R., and Norman, R.J., 2017. Nitrogen source effects on methane emissions from drill-seeded, delayed-flood rice production. Soil Science, 182(1), 9–17. https://doi.org/10.1097/SS.0000000000000188
Rondeaux, G., Steven, M., and Baret, F., 1996. Optimization of soil-adjusted vegetation indices. Remote Sensing of Environment, 55(2), 95–107.

https://doi.org/10.1016/0034-4257(95)00186-7
Rouse, J.W., Haas, R.H., Schell, J.A., and Deering, D.W., 1974. Monitoring vegetation systems in the Great Plains with ERTS. In: Proceedings of the Third ERTS-1 Symposium. NASA SP-351, 309–317.
Ruan, L., Yan, M., Zhang, L., Fan, X.S., and Yang, H., 2022. Spatial-temporal NDVI pattern of global mangroves: A growing trend during 2000–2018. Science of the Total Environment, 844, 157075. https://doi.org/10.1016/j.scitotenv.2022.157075
Osuch, M., 2015. Sensitivity and uncertainty analysis of precipitation–runoff models for the Middle Vistula basin. In: Romanowicz, R.J. and Osuch, M. (eds.), Stochastic Flood Forecasting System: The Middle River Vistula Case Study. Cham: Springer International Publishing, 61–82. https://doi.org/10.1007/978-3-319-18854-6_5
Schad, A.N., Reif, M.K., Harwood, J.H., Macon, C.L., Dodd, L.L., Vasquez, K.L., Philley, K.D., Dobson, G.E., and Steinmetz, K.M., 2025. Comparison of Field and Virtual Vegetation Surveys Conducted Using Uncrewed Aircraft System (UAS) Imagery at Two Coastal Marsh Restoration Projects. Remote Sensing, 17(2), 223. https://doi.org/10.3390/rs17020223
Schaefli, B., and Gupta, H.V., 2007. Do Nash values have value? Hydrological Processes, 21(15), 2075–2080. https://doi.org/10.1002/hyp.6825
Schneider, G.J.A., and Barnes, H.H., 1989. Guide for selecting Manning's roughness coefficients for natural channels and flood plains. U.S. Geological Survey Water-Supply Paper 2339.
Scornet, E., 2013. Tuning parameters in random forests. ESAIM: Proceedings and Surveys, 60, 133–162. https://doi.org/10.1051/proc/201760133
Sharpe, R.G., Brooks, A., Olley, J., and Kemp, J., 2023. Quantifying hydraulic roughness in a riparian forest using a drag force-based method. Journal of Flood Risk Management, 16(2), e12892. https://doi.org/10.1111/jfr3.12892
Shi, J., Yang, K., Yuan, N., Li, Y., Ma, L., Liu, Y., Fang, S., Peng, Y., Zhu, R., Wu, X., and Gong, Y., 2025. UAV-based rice aboveground biomass estimation using a random forest model with multi-organ feature selection. European Journal of Agronomy, 164, 127529. https://doi.org/10.1016/j.eja.2025.127529
Shu, M., Li, Q., Ghafoor, A., Zhu, J., Li, B., and Ma, Y., 2023. Using the plant height and canopy coverage to estimation maize aboveground biomass with UAV digital images. European Journal of Agronomy, 151, 126957. https://doi.org/10.1016/j.eja.2023.126957
Sikora, M., Bohdal, T., Tandecka, K., Kacalak, W., and Mathia, T.G., 2024. The Effect of Channel Surface Roughness on Two–Phase Flow Patterns: A Review. Energies, 17(21), 5483. https://doi.org/10.3390/en17215483
Soana, E., Bartoli, M., Milardi, M., Fano, E.A., and Castaldelli, G., 2019. An ounce of prevention is worth a pound of cure: Managing macrophytes for nitrate mitigation in irrigated agricultural watersheds. Science of the Total Environment, 647, 301–312. https://doi.org/10.1016/j.scitotenv.2018.07.385

Soana, E., Gervasio, M.P., Granata, T., Colombo, D., and Castaldelli, G., 2023. Climate change impacts on eutrophication in the Po River (Italy): Temperature-mediated reduction in nitrogen export but no effect on phosphorus. Journal of Environmental Sciences, 143, 148–163. https://doi.org/10.1016/j.jes.2023.07.008

Sosnowska, A., 2025. Assessment of long-term channel morphological changes by river bars' size estimation based on remote sensing techniques, Vistula River, Poland. Earth Science Informatics, 18(1), 115. https://doi.org/10.1007/s12145-024-01629-4

Speer, P.R., and Gamble, C.R., 1965. Magnitude and frequency of floods in the United States. U.S. Geological Survey Water-Supply Paper.

Speiser, J.L., 2021. A random forest method with feature selection for developing medical prediction models with clustered and longitudinal data. Journal of Biomedical Informatics, 117, 103763. https://doi.org/10.1016/j.jbi.2021.103763

Stamou, A.I., Papadonikolaki, G., Gkesouli, A., and Nikoletopoulos, A., 2012. Modeling the effect of vegetation on river floodplain hydraulics. Global Nest Journal, 14(3), 371–377. https://doi.org/10.30955/gnj.000883

Steven, M.D., 1998. The Sensitivity of the OSAVI Vegetation Index to Observational Parameters. Remote Sensing of Environment, 63(1), 49–60. https://doi.org/10.1016/S0034-4257(97)00114-4

Stone, B.M., and Shen, H.T., 2002. Hydraulic Resistance of Flow in Channels with Cylindrical Roughness. Journal of Hydraulic Engineering, 128(5), 500–506. https://doi.org/10.1061/(ASCE)0733-9429(2002)128:5(500)

Straatsma, M.W., and Baptist, M.J., 2008. Floodplain roughness parameterization using airborne laser scanning and spectral remote sensing. Remote Sensing of Environment, 112(3), 1062–1080. https://doi.org/10.1016/j.rse.2007.07.012

Swastika, P.V., Pudjaprasetya, S.R., Wiryanto, L.H., and Hadiarti, R.N., 2021. A momentum-conserving scheme for flow simulation in 1D channel with obstacle and contraction. Fluids, 6(1), 26. https://doi.org/10.3390/fluids6010026

Szyga-Pluta, K., Tomczyk, A.M., Piniewski, M., and Eini, M.R., 2023. Past and future changes in the start, end, and duration of the growing season in Poland. Acta Geophysica, 71(6), 3041–3055. https://doi.org/10.1007/s11600-023-01117-1

Tamiminia, H., Salehi, B., Mahdianpari, M., Quackenbush, L., Adeli, S., and Brisco, B., 2020. Google Earth Engine for geo-big data applications: A meta-analysis and systematic review. ISPRS Journal of Photogrammetry and Remote Sensing, 164, 152–170. https://doi.org/10.1016/j.isprsjprs.2020.04.001

Tan, C., Chen, Z., Liao, A., and Zeng, X., 2024. Accuracy assessment of Mavic 3 industrial UAV based on DJI Terra and Pix4Dmapper. In: Proceedings of SPIE, 13223, 498–504. https://doi.org/10.1117/12.3035344

Tang, X., Li, S., Li, T., Gao, Y., Zhang, S., Chen, Q., and Zhang, X., 2021. Review on global digital elevation products. National Remote Sensing Bulletin, 25(1), 167–181. https://doi.org/10.11834/jrs.20210210

Tang, Z., Chu, J., Zhou, Z., Zhou, T., and Yuan, K., 2025. The sensitivity analysis of parameters in the 1D–2D coupled model for urban flooding. Applied Sciences, 15(4), 2157. https://doi.org/10.3390/app15042157

Thapa, R., Thoms, M.C., Parsons, M., and Reid, M., 2016. Adaptive cycles of floodplain vegetation response to flooding and drying. Earth Surface Dynamics, 4(1), 175–191. https://doi.org/10.5194/esurf-4-175-2016

Tuia, D., Persello, C., and Bruzzone, L., 2016. Domain adaptation for the classification of remote sensing data: An overview of recent advances. IEEE Geoscience and Remote Sensing Magazine, 4(2), 41–57. https://doi.org/10.1109/MGRS.2016.2548504

Van Der Laan, M.J., Polley, E.C., and Hubbard, A.E., 2007. Super learner. Statistical Applications in Genetics and Molecular Biology, 6(1), Article 25. https://doi.org/10.2202/1544-6115.1309

Vargas-Luna, A., Crosato, A., and Uijttewaal, W.S.J., 2015. Effects of vegetation on flow and sediment transport: Comparative analyses and validation of predicting models. Earth Surface Processes and Landforms, 40(2), 157–176. https://doi.org/10.1002/esp.3633

Vermuyten, E., Meert, P., Wolfs, V., and Willems, P., 2020. Impact of seasonal changes in vegetation on the river model prediction accuracy and real-time flood control performance. Journal of Flood Risk Management, 13(4), e12651. https://doi.org/10.1111/jfr3.12651

Vezzoli, R., Mercogliano, P., Pecora, S., Zollo, A.L., and Cacciamani, C., 2015. Hydrological simulation of Po River (North Italy) discharge under climate change scenarios using the RCM COSMO-CLM. Science of the Total Environment, 521–522, 346–358. https://doi.org/10.1016/j.scitotenv.2015.03.096

Vreugdenhil, C.B., 1994. Numerical Methods for Shallow-Water Flow. Dordrecht: Kluwer Academic Publishers. https://doi.org/10.1007/978-94-015-8354-1

Vrugt, J.A., Gupta, H.V., Bastidas, L.A., Bouten, W., and Sorooshian, S., 2003. Effective and efficient algorithm for multiobjective optimization of hydrologic models. Water Resources Research, 39(8), 1214. https://doi.org/10.1029/2002WR001746

Vyawahare, R., and Tatewar, S., 2025. A Comprehensive Review on the Role of Vegetation in Open Channels and its Impact on Sediment Transport and Flow Dynamics. EPJ Web of Conferences, 328, 01018. https://doi.org/10.1051/epjconf/202532801018

Wallace, J., Behn, G., and Furby, S., 2006. Vegetation condition assessment and monitoring from sequences of satellite imagery. Ecological Management and Restoration, 7(S1), S31–S36. https://doi.org/10.1111/j.1442-8903.2006.00289.x

Wang, H., Seaborn, T., Wang, Z., Caudill, C.C., and Link, T.E., 2021. Modeling tree canopy height using machine learning over mixed vegetation landscapes. International Journal of Applied Earth Observation and Geoinformation, 101, 102353. https://doi.org/10.1016/j.jag.2021.102353

Wang, J., Yang, J., Li, Z., Ke, L., Li, Q., Fan, J., and Wang, X., 2024. Research on Soil

Erosion Based on Remote Sensing Technology: A Review. Agriculture, 15(1), 18. https://doi.org/10.3390/agriculture15010018

Weiss, K., Khoshgoftaar, T.M., and Wang, D.D., 2016. A survey of transfer learning. Journal of Big Data, 3(1), 9. https://doi.org/10.1186/s40537-016-0043-6

Werner, M.G.F., 2004. A comparison of flood extent modelling approaches through constraining uncertainties on gauge data. Hydrology and Earth System Sciences, 8(6), 1141–1152. https://doi.org/10.5194/hess-8-1141-2004

Westoby, M.J., Brasington, J., Glasser, N.F., Hambrey, M.J. and Reynolds, J.M., 2012. 'Structure-from-Motion' photogrammetry: A low-cost, effective tool for geoscience applications. Geomorphology, 179, pp.300–314. https://doi.org/10.1016/j.geomorph.2012.08.021

Wilimitis, D., and Walsh, C.G., 2023. Practical Considerations and Applied Examples of Cross-Validation for Model Development and Evaluation in Health Care: Tutorial. JMIR AI, 2(1), e49023. https://doi.org/10.2196/49023

Wilson, C.A.M.E., Stoesser, T., Bates, P.D., and Pinzen, A.B., 2003. Open Channel Flow through Different Forms of Submerged Flexible Vegetation. Journal of Hydraulic Engineering, 129(11), 847–853. https://doi.org/10.1061/(ASCE)0733-9429(2003)129:11(847)

Wojkowski, J., Wałęga, A., Radecki-Pawlik, A., Młyński, D., and Lepeška, T., 2022. The influence of land cover changes on landscape hydric potential and river flows: Upper Vistula, Western Carpathians. CATENA, 210, 105878. https://doi.org/10.1016/j.catena.2021.105878

Wolpert, D.H., 1992. Stacked generalization. Neural Networks, 5(2), 241–259. https://doi.org/10.1016/S0893-6080(05)80023-1

Woodcock, C.E., and Strahler, A.H., 1987. The factor of scale in remote sensing. Remote Sensing of Environment, 21(3), 311–332. https://doi.org/10.1016/0034-4257(87)90015-0

Woźnica, A., Absalon, D., Matysik, M., Bąk, M., Cieplok, A., Halabowski, D., Koczorowska, A., Krodkiewska, M., Libera, M., Sierka, E., Spyra, A., Czerniawski, R., Sługocki, Ł., and Łozowski, B., 2023. Analysis of the Salinity of the Vistula River Based on Patrol Monitoring and State Environmental Monitoring. Water, 15(5), 838. https://doi.org/10.3390/w15050838

Wulder, M.A., Loveland, T.R., Roy, D.P., Crawford, C.J., Masek, J.G., Woodcock, C.E., Allen, R.G., Anderson, M.C., Belward, A.S., Cohen, W.B., Dwyer, J., Erb, A., Gao, F., Griffiths, P., Helder, D., Hermosilla, T., Hipple, J.D., Hostert, P., Hughes, M.J., and Zhu, Z., 2019. Current status of Landsat program, science, and applications. Remote Sensing of Environment, 225, 127–147. https://doi.org/10.1016/j.rse.2019.02.015

Wyżga, B., Kundzewicz, Z.W., Konieczny, R., Piniewski, M., Zawiejska, J., and Radecki-Pawlik, A., 2018. Comprehensive approach to the reduction of river flood risk: Case study of the Upper Vistula Basin. Science of the Total Environment, 631–632, 1251–1267.

https://doi.org/10.1016/j.scitotenv.2018.03.015
Xie, Y., Sha, Z., and Yu, M., 2008. Remote sensing imagery in vegetation mapping: a review. Journal of Plant Ecology, 1(1), 9–23. https://doi.org/10.1093/jpe/rtm005
Yan, K., Gao, S., Yan, G., Ma, X., Chen, X., Zhu, P., Li, J., Gastellu-Etchegorry, J.P., Myneni, R.B., and Wang, Q., 2025. A global systematic review of the remote sensing vegetation indices. International Journal of Applied Earth Observation and Geoinformation, 139, 104560. https://doi.org/10.1016/j.jag.2025.104560
Yassine, R., Cassan, L., Roux, H., Frysou, O., and Pérès, F., 2023. Numerical modelling of the evolution of a river reach with a complex morphology to help define future sustainable restoration decisions. Earth Surface Dynamics, 11(6), 1199–1221. https://doi.org/10.5194/esurf-11-1199-2023
Yu, P., Ji, T., Wu, X., Chen, Y., and Liu, G., 2025. An Adaptive Local Time-Stepping Method Applied to Storm Surge Inundation Simulation. Journal of Marine Science and Engineering, 13(3), 467. https://doi.org/10.3390/jmse13030467
Zahidi, I., Yusuf, B., and Cope, M., 2014. Vegetative roughness estimation for hydraulic modelling: a review. Research in Civil and Environmental Engineering, 2(1), 1–10.
Zanchettin, D., Traverso, P., and Tomasino, M., 2008. Po River discharges: A preliminary analysis of a 200-year time series. Climatic Change, 89(3–4), 411–433. https://doi.org/10.1007/s10584-008-9395-z
Zhang, Q., Wang, M., Ma, Q., Xie, W., Qian, R., Guo, Y., and Zhang, S., 2025. Friction factor for rough fractures: Roughness and flow inertia effects. Physics of Fluids, 37(2), 026612. https://doi.org/10.1063/5.0252669
Zhang, X., 2018. Simulating eroded soil organic carbon with the SWAT-C model. Environmental Modelling and Software, 102, 39–48. https://doi.org/10.1016/j.envsoft.2018.01.005
Zhang, Y., Zhang, W., Ji, Y., and Zhao, H., 2024. Forest Height Estimation and Inversion of Satellite-Based X-band InSAR Data. Geomatics and Information Science of Wuhan University, 49(12), 2279–2289. https://doi.org/10.13203/j.whugis20220373
Zhao, L., Liu, Y., and Luo, Y., 2021. The Efficiency of Parameters Derived from the Digital Surface Model (DSM) in Indicating the Forest Gap Features. Remote Sensing Technology and Application, 36(2), 420–430.
Zhou, X., Hu, K., Xiao, H., Yang, Y., Chen, J., and Cheng, Y., 2024. Effects of vegetation on the spatiotemporal distribution of soil water content in re-vegetated slopes using temporal stability analysis. CATENA, 234, 107570. https://doi.org/10.1016/j.catena.2023.107570
Zhu, X.X., Tuia, D., Mou, L., Xia, G.S., Zhang, L., Xu, F., and Fraundorfer, F., 2017. Deep Learning in Remote Sensing: A Comprehensive Review and List of Resources. IEEE Geoscience and Remote Sensing Magazine, 5(4), 8–36. https://doi.org/10.1109/MGRS.2017.2762307
Zhu, Y., 2022. The utilization of Delft3D model to relate the coastal hydrodynamics

and water quality with the illustration of Yong River Estuary in the southeast of China. Doctoral dissertation.

Ziegel, E.R., Hastie, T., Tibshirani, R., and Friedman, J., 2009. The Elements of Statistical Learning. New York: Springer. https://doi.org/10.1007/978-0-387-84858-7

Acknowledgements

This research was funded by the National Science Centre Poland–call PRELUDIUM BIS-3, Grant Number 2021/43/O/ST10/00539. The work is partially supported by a subsidy from the Polish Ministry of Education and Science for the Institute of Geophysics Polish Academy of Sciences.

First of all, I would like to thank my supervisor, dr. hab. Michael Nones, for providing me the opportunity to work at IGF PAS and for his fully support at these years. I am really appreciate to have such a nice supervisor that who always gives me positive responses when I have some new ideas, helps me to extend some networks, treats every guest I want to invite seriously, and helps me a lot in mu daily life, especially when I first arrived in Poland.

Secondly, I would like to thank my colleagues in the department. In particular, Dr. Varrani Arianna and Dr. Kaveh Ghahraman helped me a lot. Additionally, I would like to thank the PhD students from our institute, who were always kind enough to support me.

Finally, I would like to thank my family and myself. My parents have always supported every decision I made unconditionally, which allowed me to come this far. I am also grateful to myself for never giving up along the way.

Appendix A. DJI Mavic 3 Multispectral Specifications

The UAV used in this study was a DJI Mavic 3 Multispectral (M3M). The system integrates one RGB camera and four multispectral sensors mounted on a stabilized gimbal.

The RGB camera features a 4/3 CMOS sensor with a resolution of 20 MP and is equipped with a mechanical shutter. The multispectral module consists of four independent 5 MP sensors corresponding to the Green (560 nm), Red (650 nm), Red Edge (730 nm), and Near-Infrared (860 nm) spectral bands.

The UAV includes an integrated spectral sunlight sensor for irradiance measurement during flight. For positioning, the system is equipped with GNSS and supports RTK integration via the PSDK port. The UAV also includes omnidirectional vision systems and dual infrared sensing modules for stabilization and obstacle detection. The main technical specifications of the system are summarized in Table A1.

Table A1-1. Technical Specifications of the DJI M3M

Category	**Specification**
RGB sensor	4/3 CMOS, 20 MP
RGB shutter	Mechanical shutter
Multispectral sensors	4 × 5 MP
Spectral bands	560 nm (Green), 650 nm (Red), 730 nm (Red Edge), 860 nm (NIR)
Irradiance measurement	Integrated spectral sunlight sensor
Positioning	GNSS, RTK-supported
Vision system	Forward, backward, lateral, upward, downward
Infrared sensing	Dual 3D infrared modules
Operating temperature	−10°C to 40°C
Maximum flight time	43 min

Overall, the DJI Mavic 3 Multispectral provides integrated RGB and multispectral imaging capabilities together with GNSS-based positioning and onboard irradiance sensing. These parameters define the technical conditions under which the UAV imagery used in this study was acquired.

Appendix B. Vegetation height for UAV data

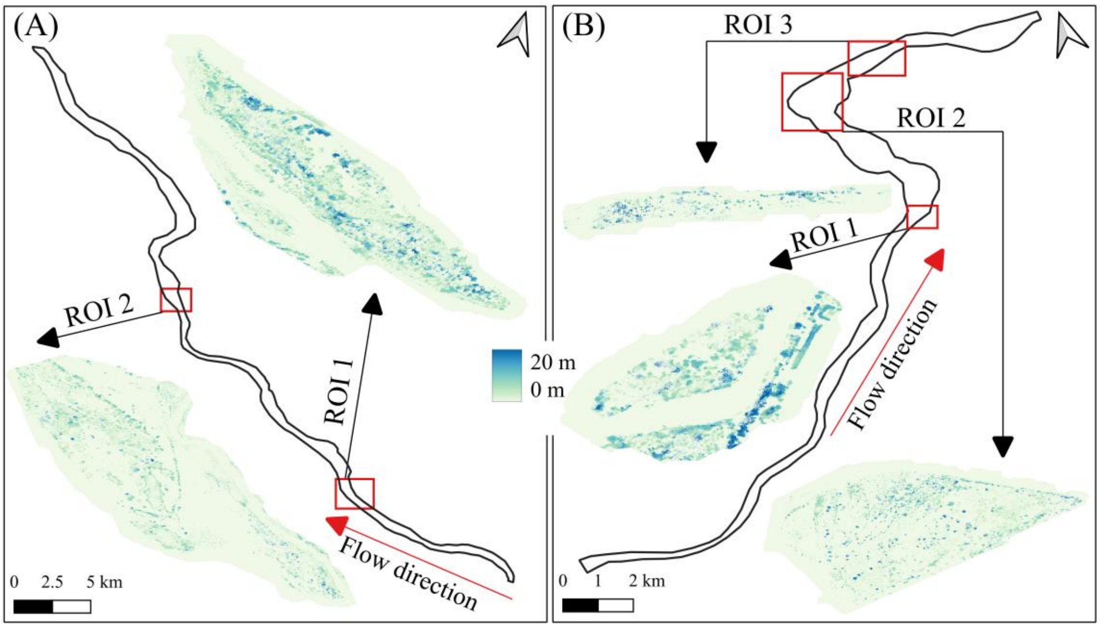

Figure B-1. Spatial distribution of vegetation height on sandbars in the Vistula and Po Reaches. (A) Vistula Reach and (B) Po Reach.

Appendix C. Different feature combinations used for ML model

Due to the relatively limited performance of machine learning models trained using only MVIs, additional features were introduced to explore whether the model accuracy could be improved. All candidate features derived from the vegetation indices are listed in Table C1-1.

To identify the best feature combinations, one third of the available samples were randomly selected, and machine-learning models were trained using all possible feature combinations. In this test, the samples were not separated into low vegetation and tall vegetation classes, as the purpose was only to identify feature combinations with better predictive performance.

The five best-performing feature combinations for the Vistula, Po, and Vistula+Po datasets are presented in Tables C1-2 to C1-4, respectively. Based on the overall comparison, the feature set x_1-x_{12} (Table 3-1), which was adopted in the main analysis, was considered to provide the most stable and reliable performance.

Table C1-1. All candidate features can be used for model training

Feature	Definition
F_1	NDVI
F_2	GNDVI
F_3	LCI
F_4	NDRE
F_5	OSAVI
F_6	$NDVI^2$
F_7	$GNDVI^2$
F_8	LCI^2
F_9	$NDRE^2$
F_{10}	$OSAVI^2$
F_{11}	NDVI * GNDVI
F_{12}	NDVI * LCI

F_{13}	NDVI * NDRE
F_{14}	NDVI * OSAVI
F_{15}	GNDVI * LCI
F_{16}	GNDVI * NDRE
F_{17}	GNDVI * OSAVI
F_{18}	LCI * NDRE
F_{19}	LCI * OSAVI
F_{20}	NDRE * OSAVI

Table C1-2. Top five feature combinations ranked by R² for Vistula+Po Reaches

Feature combinations	R^2	***RMSE* (m)**	***PBIAS* (%)**
$F_1+F_2+F_3+F_4+F_5+F_6+F_7+F_8+F_{11}+F_{13}+F_{14}+F_{16}$	0.55	3.79	2.82
$F_1+F_2+F_3+F_4+F_5+F_6+F_7+F_9+F_{11}$	0.52	3.79	2.84
$F_1+F_2+F_3+F_4+F_5+F_6+F_7+F_9+F_{10}+F_{11}$	0.52	3.79	2.99
$F_1+F_2+F_3+F_4+F_5+F_6+F_7+F_9+F_{11}+F_{12}$	0.51	3.80	3.00
$F_1+F_2+F_3+F_4+F_5+F_6+F_7+F_9+F_{10}+F_{11}+F_{12}$	0.50	3.80	3.12

Table C1-3. Top five feature combinations ranked by R² for Vistula Reach

Feature combinations	R^2	***RMSE* (m)**	***PBIAS* (%)**
$F_1+F_2+F_3+F_4+F_5+F_6+F_7+F_9+F_{10}+F_{11}$	0.65	2.87	2.45
$F_1+F_2+F_3+F_4+F_5+F_6+F_7+F_8+F_{11}+F_{13}+F_{14}+F_{16}$	0.65	2.87	2.62
$F_1+F_2+F_3+F_4+F_5+F_6+F_7+F_9+F_{11}+F_{12}$	0.63	2.87	2.63
$F_1+F_2+F_3+F_4+F_5+F_6+F_7+F_9+F_{10}+F_{11}+F_{12}$	0.62	2.88	2.62
$F_1+F_2+F_3+F_4+F_5+F_6+F_7+F_8+F_9+F_{11}$	0.60	2.88	2.76

Table C1-4. Top five feature combinations ranked by R^2 for Po Reach

Feature combinations	$\boldsymbol{R^2}$	***RMSE* (m)**	***PBIAS* (%)**
$F_1+F_2+F_3+F_4+F_5+F_6+F_7+F_8+F_{11}+F_{13}+F_{14}+F_{16}$	0.58	2.87	2.51
$F_1+F_2+F_3+F_4+F_5+F_6+F_7+F_9+F_{11}$	0.57	2.87	2.64
$F_1+F_2+F_3+F_4+F_5+F_6+F_7+F_9+F_{10}+F_{11}$	0.57	2.87	2.66
$F_1+F_2+F_3+F_4+F_5+F_6+F_7+F_9+F_{11}+F_{12}$	0.57	2.88	2.76
$F_1+F_2+F_3+F_4+F_5+F_6+F_7+F_8+F_9+F_{11}$	0.55	2.88	2.70

Appendix D. Delft 3D FM model

D1. Model configuration summary

To make the modelling component clearer, Table D1-1 summarizes the key Delft3D-FM model settings used in this thesis. It reports (i) the computational mesh characteristics derived from the provided mesh NetCDF files, and (ii) the main time-control and output settings extracted from the model configuration/log excerpts. This table is intended as a quick reference for readers before showing supplementary maps/time series of simulated hydrodynamic variables.

Table D1-1. Key model settings and mesh statistics for the two reaches.

	Vistula Reach	**Po Reach**
Number of 2D cells (faces)	5,990	15,341
Number of mesh nodes	6,703	16,443
Number of mesh edges	12,692	31,783
Median cell area (m^2)	8,674	638
Cell area (5–95% range, m^2)	3,190 – 18,696	222 – 3,627
Median equivalent cell size (area, m)	93.1	25.3
Equivalent cell size (5–95% range, m)	56.5 – 136.7	14.9 – 60.2
Simulation period	28.05 – 31.10, 2024	28.05 – 31.10, 2024
Initial time step (dtInit)	1 s	1 s
Maximum time step (dtMax)	30 s	30 s
External forcing update interval	300 s	300 s
Roughness update interval	Daily	Daily
Automatic time stepping	Enabled	Enabled
History output interval	86,400 s	86,400 s
Map output interval	86,400 s	86,400 s

D2. Average MVIs values and maps between the same period of 2024 and 2025

Because the UAV survey was conducted in 2025, while the hydrological data available for the hydrodynamic simulations only extend to 2024, it was necessary to verify whether vegetation conditions were similar between the two years.

To verify whether vegetation conditions are similar during the same period in both years, multispectral satellite imagery from 1 June to 31 October in both 2024 and 2025 was analysed. Five vegetation indices (NDVI, GNDVI, LCI, NDRE, and OSAVI) derived from Sentinel-2 imagery were calculated. Both the spatial distributions and the mean values of these indices were compared.

The statistical summaries (Table D2-1) and maps (Figure D2-1 to D2-5) are presented in the following tables and figures, demonstrating that vegetation conditions during the study period are generally consistent between the two years.

Table D2-1. Comparison of five MVIs between the same period of two years

	Year	**NDVI**	**GNDVI**	**LCI**	**NDRE**	**OSAVI**
Vistula	2024	0.26	0.19	-0.03	0.07	0.22
Reach	2025	0.30	0.23	-0.02	0.09	0.24
Po	2024	0.11	0.04	-0.06	0.02	0.14
Reach	2025	0.18	0.08	-0.04	0.06	0.19

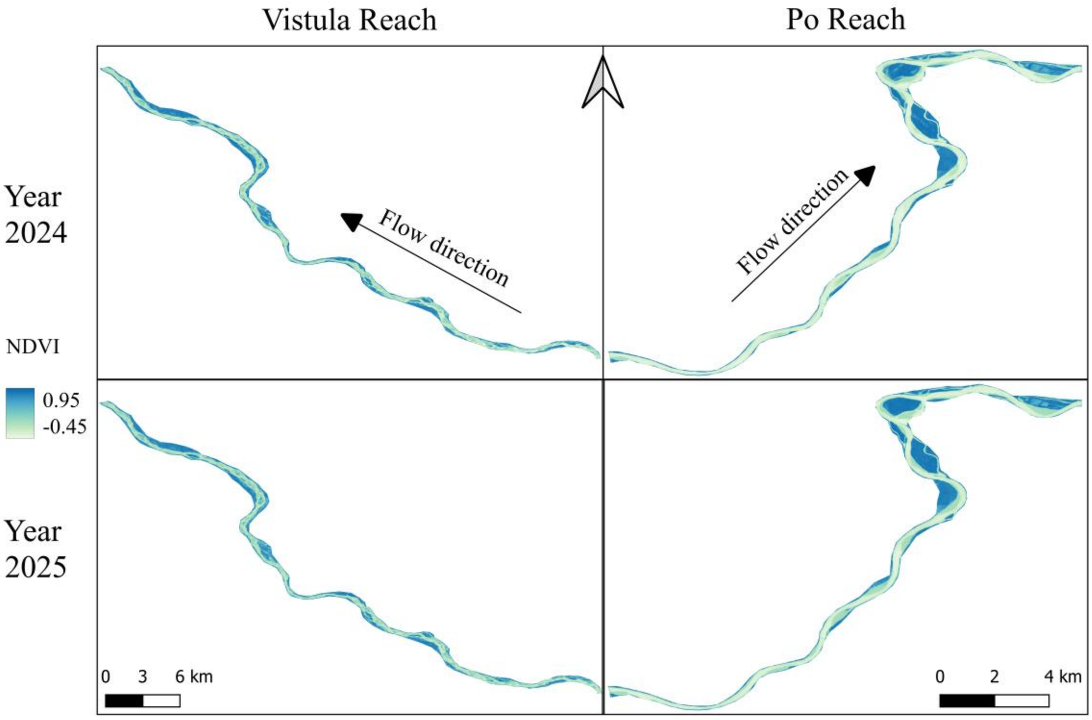

Figure D2-1. NDVI maps for the same periods of two years.

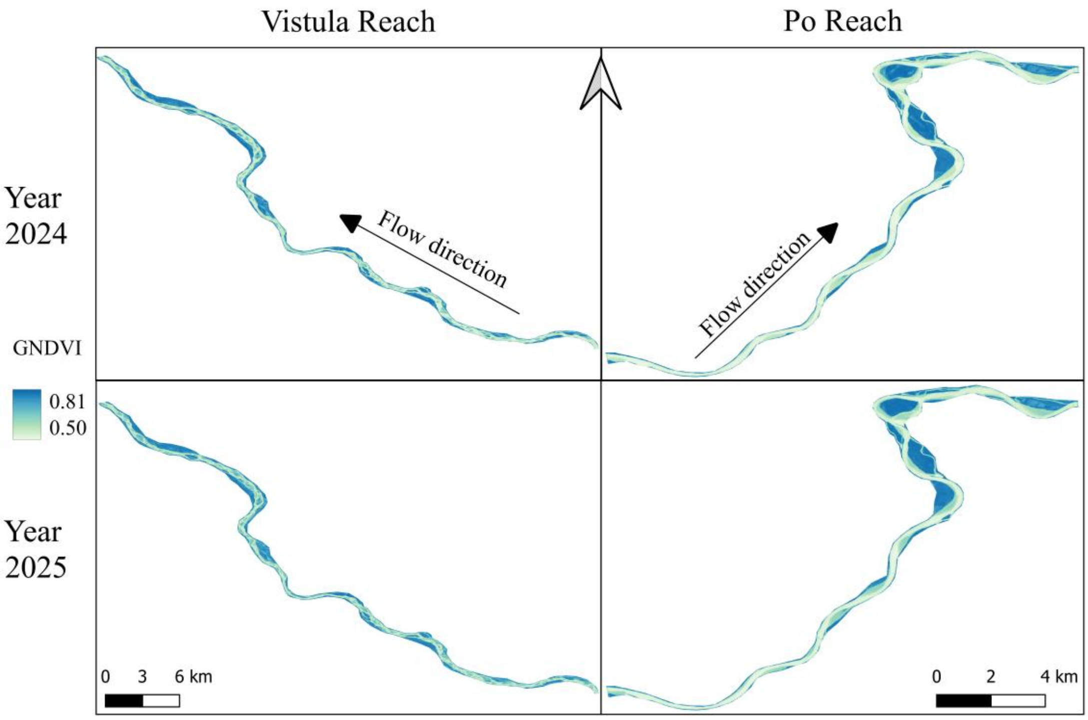

Figure D2-2. GNDVI maps for the same periods of two years.

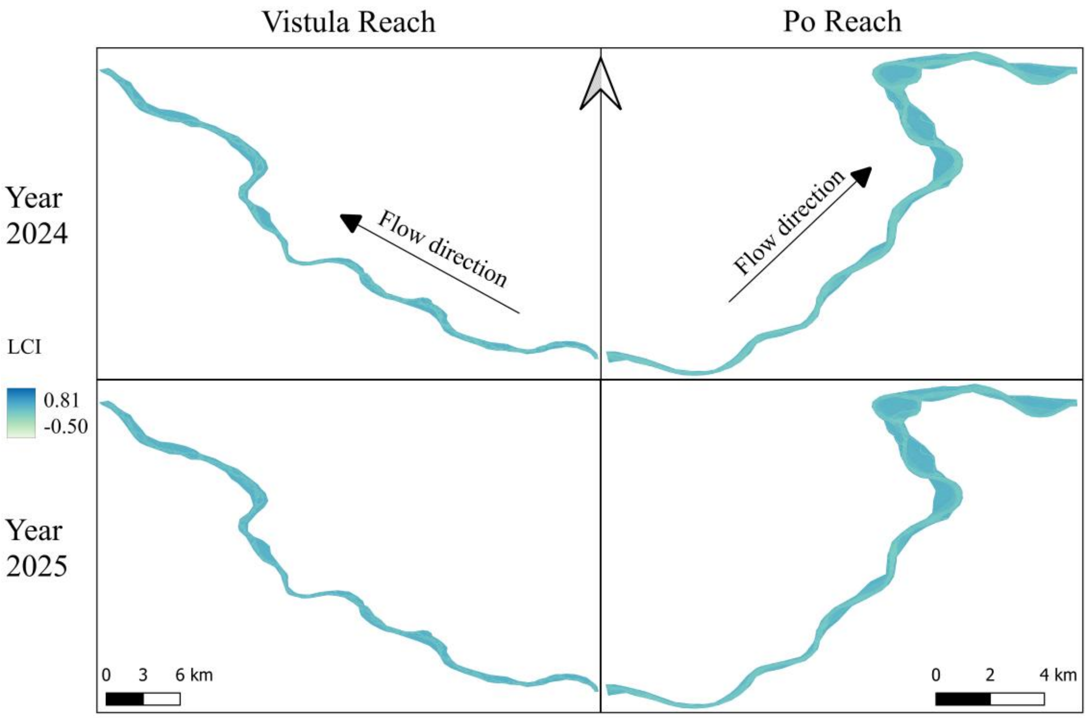

Figure D2-3. LCI maps for the same periods of two years.

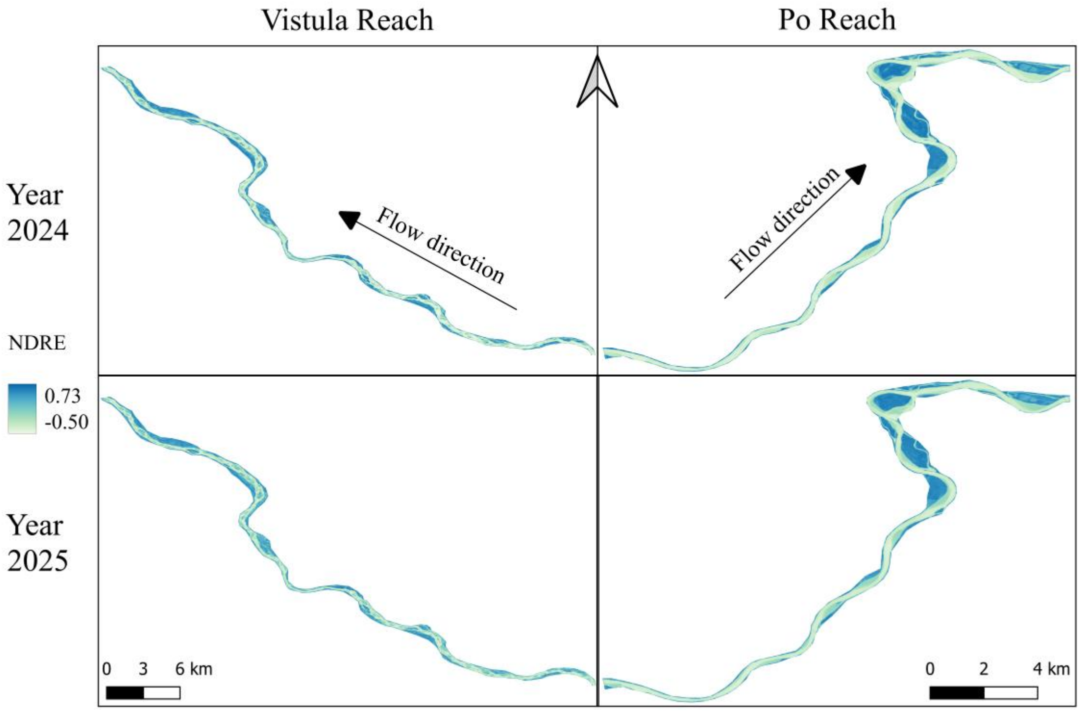

Figure D2-4. NDRE maps for the same periods of two years

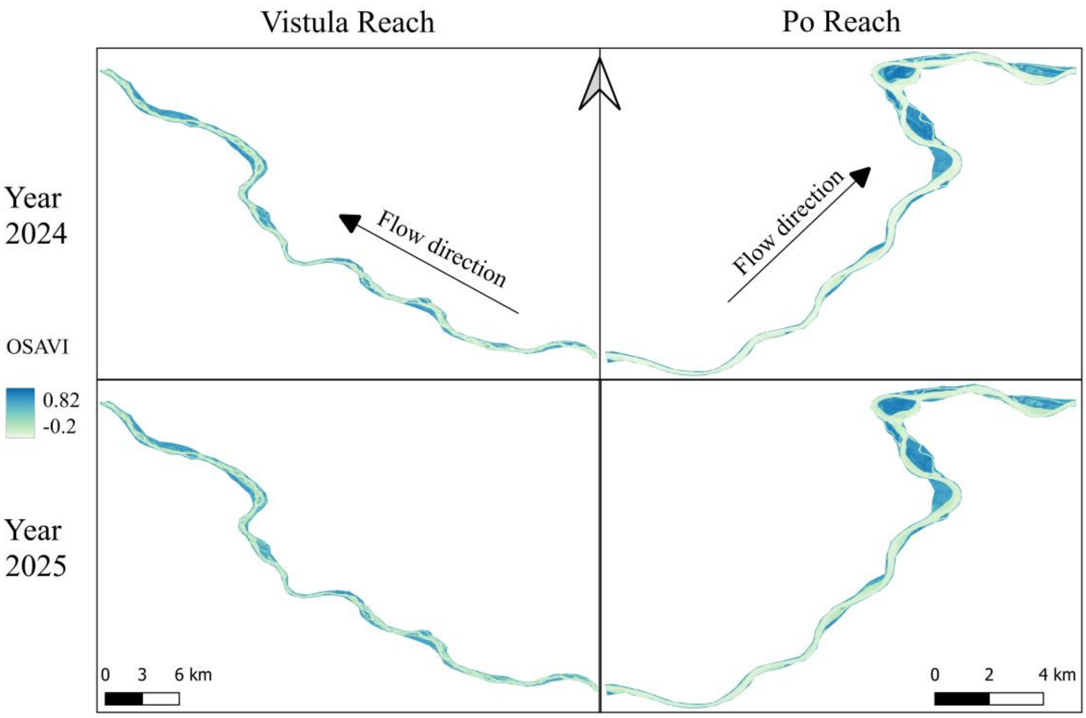

Figure D2-5. OSAVI maps for the same periods of two years.

D3. Flow element center velocity and total bed shear stress

Spatial distributions of total bed shear stress magnitude (N/m^2, also refer as pa) derived from the Delft3D-FM simulations for both study rivers are shown in Figure D2-1(Vistula Reach) and D2-2 (Po Reach).

For the Vistula River, four representative hydraulic conditions were selected based on observed discharge: a secondary flood peak (8 June 2024), a moderate flood stage (14 June 2024), an extreme low-flow condition (10 September 2024), and the maximum flood peak (20 September 2024). For each selected date, simulations using a calibrated fixed Manning coefficient were compared with simulations using satellite-derived dynamic Manning coefficients under identical boundary conditions.

For the Po River, four representative conditions were similarly analysed: a moderate flood event (26 June 2024), an extreme low-flow stage (7 August 2024), the maximum flood peak (21 October 2024), and a secondary flood peak (29 October 2024). The same modelling framework and boundary conditions were applied to ensure consistency between fixed and dynamic roughness simulations.

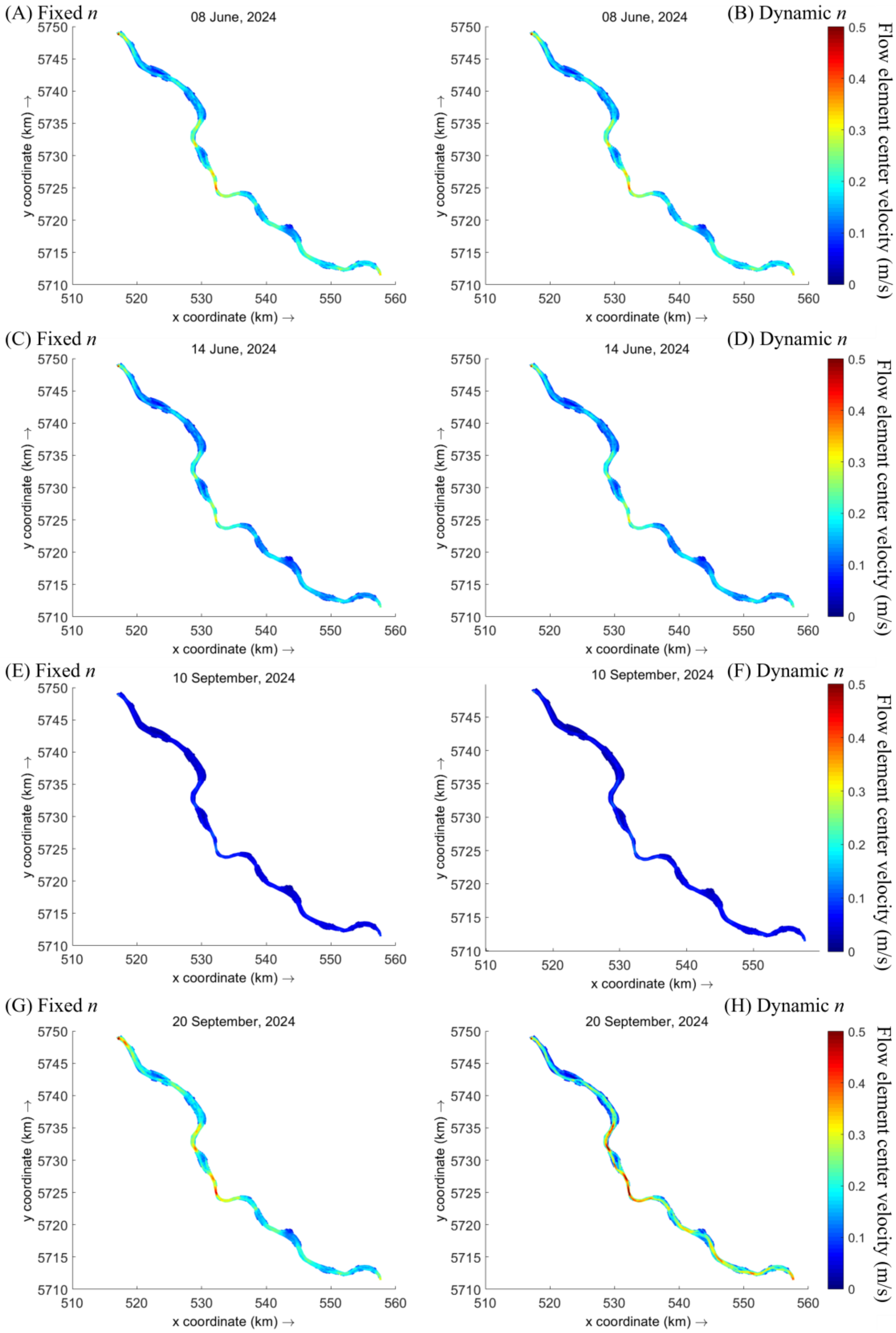

Figure D3-1. Spatial distribution of flow element center velocity (m/s) in the Vistula River under fixed and dynamic Manning roughness schemes for four representative hydraulic conditions: (A) and (B) secondary flood peak (8 June 2024), (C) and (D) moderate flood stage (14 June 2024), (E) and (F) extreme low-flow condition (10 September 2024), and (G) and (H) maximum flood peak (20 September 2024). For each condition, simulations using a calibrated fixed *n* (left panels) are compared with simulations using spatially distributed satellite-derived dynamic *n* (right panels).

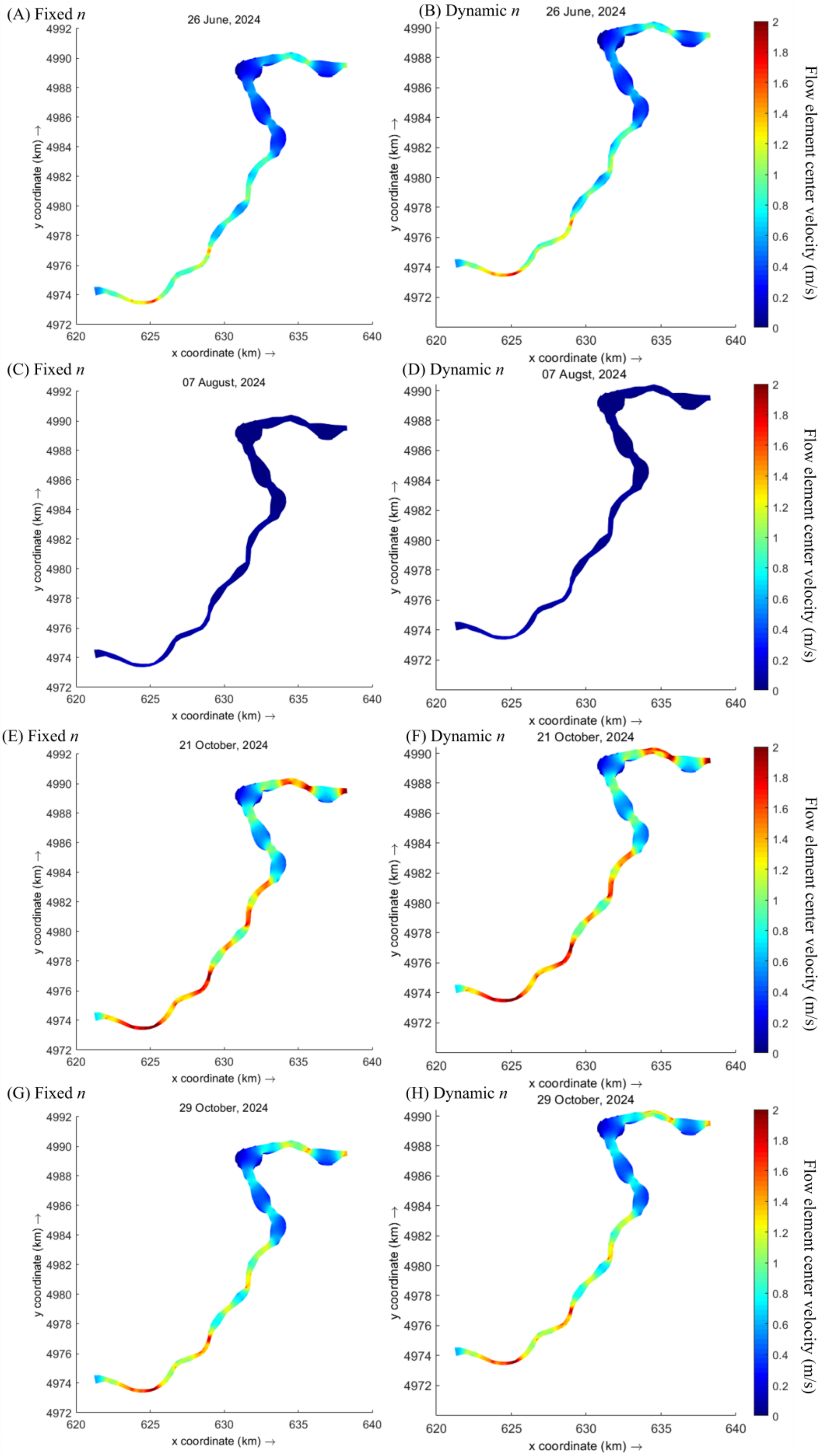
(A) Fixed n
26 June, 2024
(B) Dynamic n
26 June, 2024
(C) Fixed n
07 August, 2024
(D) Dynamic n
07 Augst, 2024
(E) Fixed n
21 October, 2024
(F) Dynamic n
21 October, 2024
(G) Fixed n
29 October, 2024
(H) Dynamic n
29 October, 2024
x coordinate (km) →
y coordinate (km) →
Flow element center velocity (m/s)

Figure D3-2. Spatial distribution of flow element center velocity (m/s) in the Po River under fixed and dynamic Manning roughness schemes for four representative hydraulic conditions: (A) and (B) moderate flood event (26 June 2024), (C) and (D) extreme low-flow stage (7 August 2024), (E) and (F) maximum flood peak (21 October 2024), and (G) and (H) secondary flood peak (29 October 2024). For each condition, simulations using a calibrated fixed *n* (left panels) are compared with simulations using spatially distributed satellite-derived dynamic *n* (right panels).

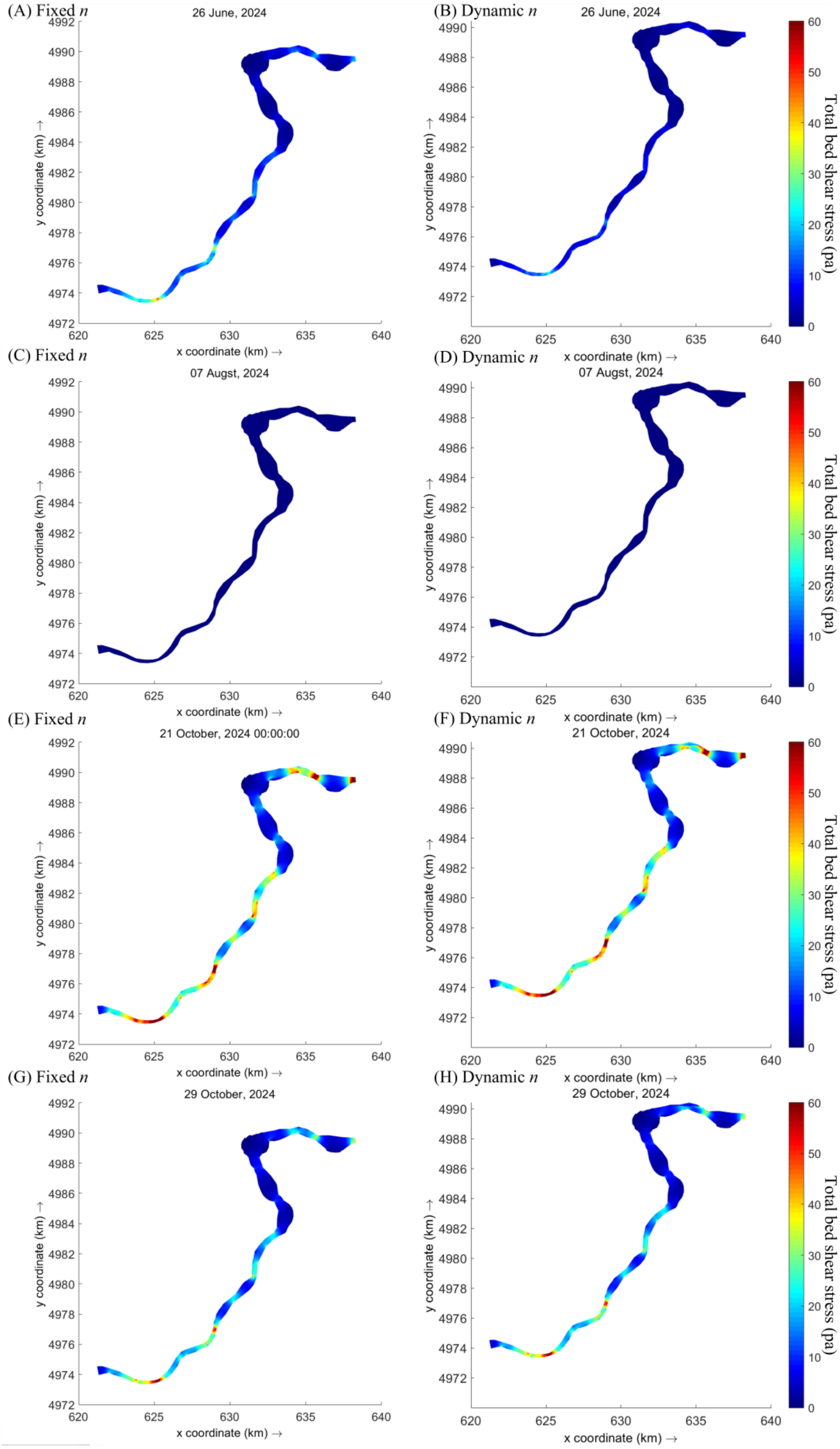

(A) Fixed *n*
26 June, 2024
(B) Dynamic *n*
26 June, 2024
(C) Fixed *n*
07 Augst, 2024
(D) Dynamic *n*
07 Augst, 2024
(E) Fixed *n*
21 October, 2024 00:00:00
(F) Dynamic *n*
21 October, 2024
(G) Fixed *n*
29 October, 2024
(H) Dynamic *n*
29 October, 2024
y coordinate (km) →
x coordinate (km) →
Total bed shear stress (pa)

Figure D3-3. Spatial distribution of total bed shear stress magnitude (pa) in the Vistula River under fixed and dynamic Manning roughness schemes for four representative hydraulic conditions: (A) and (B) secondary flood peak (8 June 2024), (C) and (D) moderate flood stage (14 June 2024), (E) and (F) extreme low-flow condition (10 September 2024), and (G) and (H) maximum flood peak (20 September 2024). For each condition, simulations using a calibrated fixed *n* (left panels) are compared with simulations using spatially distributed satellite-derived dynamic *n* (right panels).

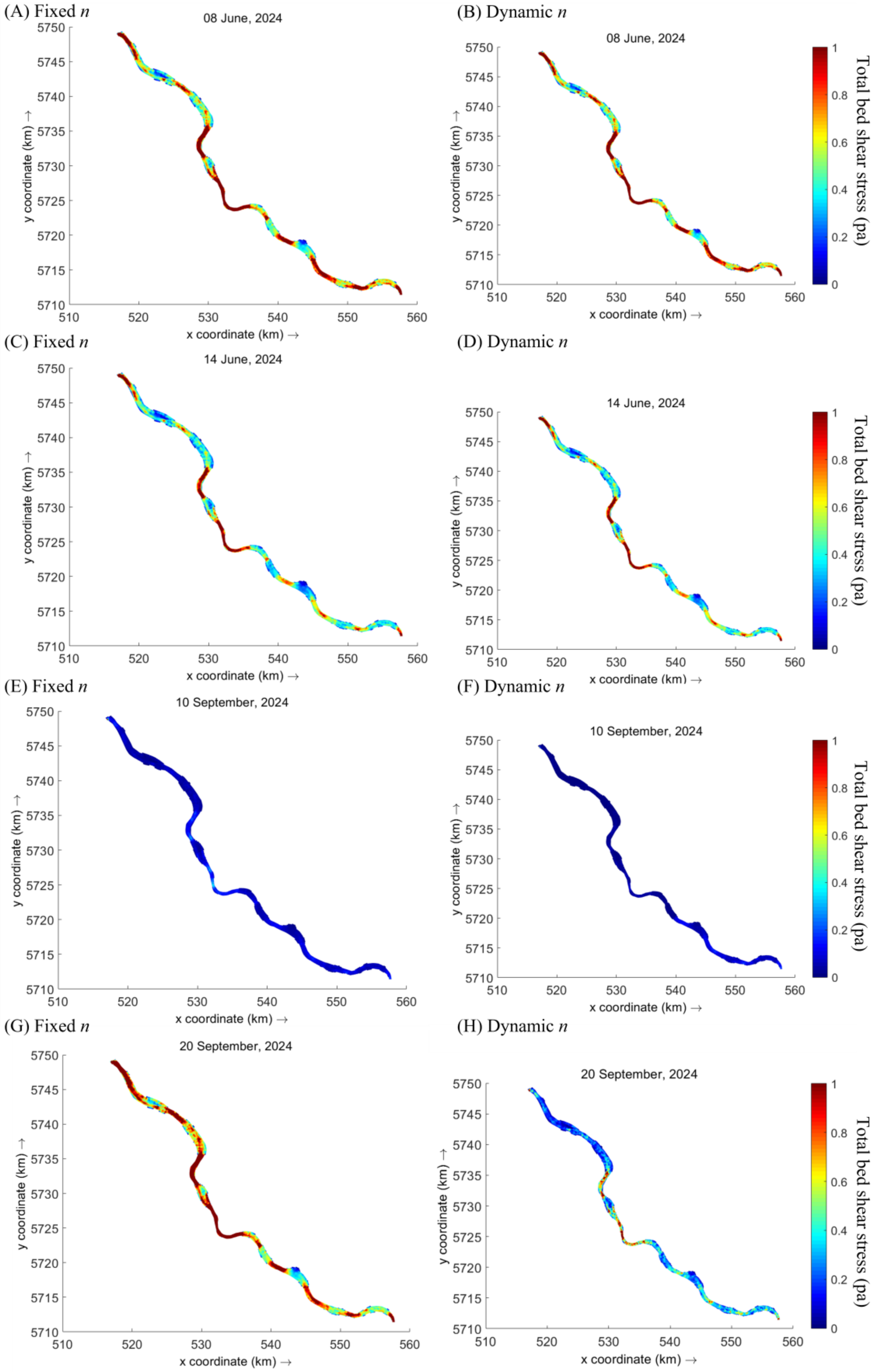

(A) Fixed *n*
08 June, 2024
(B) Dynamic *n*
08 June, 2024
(C) Fixed *n*
14 June, 2024
(D) Dynamic *n*
14 June, 2024
(E) Fixed *n*
10 September, 2024
(F) Dynamic *n*
10 September, 2024
(G) Fixed *n*
20 September, 2024
(H) Dynamic *n*
20 September, 2024
y coordinate (km) →
x coordinate (km) →
5750
5745
5740
5735
5730
5725
5720
5715
5710
510
520
530
540
550
560
Total bed shear stress (pa)
0
0.2
0.4
0.6
0.8
1

Figure D3-4. Spatial distribution of total bed shear stress magnitude (pa) for the Po River under fixed (left column) and dynamic (right column) Manning roughness schemes during four representative hydraulic conditions: (A) and (B) moderate flood event (26 June 2024), (C) and (D) extreme low-flow stage (7 August 2024), (E) and (F) maximum flood peak (21 October 2024), and (G) and (H) secondary flood peak (29 October 2024).

All figures display flow element center velocity and total bed shear stress magnitude over the computational domain. Within each river system, a consistent colour scale is used to allow direct visual comparison between roughness schemes. Flow element center velocity and bed shear stress are presented because it directly reflects the friction term in the depth-averaged momentum equations.